

2019-09-20

# Cytotoxic, Cellular Uptake, and Photophysical Properties of Various Re(I) Tricarbonyl Complexes

Capper, Miles S.

---

Capper, M. S. (2019). Cytotoxic, Cellular Uptake, and Photophysical Properties of Various Re(I) Tricarbonyl Complexes (Master's thesis, University of Calgary, Calgary, Canada). Retrieved from <https://prism.ucalgary.ca>.

<http://hdl.handle.net/1880/111074>

*Downloaded from PRISM Repository, University of Calgary*

UNIVERSITY OF CALGARY

Cytotoxic, Cellular Uptake, and Photophysical Properties of Various Re(I) Tricarbonyl  
Complexes

by

Miles S. Capper

A THESIS

SUBMITTED TO THE FACULTY OF GRADUATE STUDIES  
IN PARTIAL FULFILMENT OF THE REQUIREMENTS FOR THE  
DEGREE OF MASTER OF SCIENCE

GRADUATE PROGRAM IN CHEMISTRY

CALGARY, ALBERTA

SEPTEMBER, 2019

© Miles S. Capper 2019

## Abstract

A series of Re(I) tricarbonyl complexes with the general formula, *fac*-[Re(CO)<sub>3</sub>(2,2'-bipyridine)(X)]<sup>+0/-</sup> (X= *L*-cysteine; N-acetyl-*L*-cysteine; thiosulfate) were characterized using spectroscopic techniques and single-crystal X-ray diffraction. Photophysical, as well as singlet oxygen (<sup>1</sup>O<sub>2</sub>) generation and CO releasing properties were assessed. Cell viability of the complexes against the MDA-MB-231 breast cancer cell line were determined. Cellular localization and accumulation were investigated using synchrotron-based X-ray fluorescence microscopy (XFM).

The results of this study show the cytotoxicity, cellular uptake and photophysical properties of *fac*-[Re(CO)<sub>3</sub>(bpy)X]<sup>+0/-</sup> complexes (X= H<sub>2</sub>O, HCys<sup>-</sup>, NAC<sup>2-</sup>, S<sub>2</sub>O<sub>3</sub><sup>2-</sup>; bpy=2,2'-bipyridine). The cytotoxicity of *fac*-[Re(CO)<sub>3</sub>(bpy)(H<sub>2</sub>O)]<sup>+</sup> is diminished when the aqua ligand is replaced by cysteine or thiosulfate.

## Acknowledgements

I would like to thank my supervisor, Dr Farideh Jalilehvand for providing funding throughout this project and letting me explore my interests so freely. I would also like to give a special thanks to Dr Alejandra Enriquez Garcia who was a source of immense support and advice as well as making the workspace a fun and happy place. I would also like to thank Valerie J. Brunskill for her efforts as well as keeping me fed throughout my research. I look forward to seeing what both will achieve in the future. I would also like to thank all other group members both past and present.

I would like to thank both Dr. Belinda Heyne and Dr Carrie Shemanko. Dr. Heyne provided me with invaluable knowledge about the photochemistry as well as allowing me to use her lab. I will also give a special mention to Nicolas Macia for his efforts on detecting  $^1\text{O}_2$  and fluorescence and always being free to answer my questions. Dr Shemanko provided me with invaluable advice regarding my biological experiments and the gratitude for allowing me to use her lab. I would also like to thank Barry Lai from the Argonne National Laboratory for his work on X-ray fluorescence imaging. I would also like to thank Dr. Benjamin S. Gelfand and Dr Jian-Bin Lin for their assistance with single-crystal X-ray diffraction. Additionally, I would like to thank Dr. Sathish Ponnurangam and Amir Alihosseinzadeh for their help with measuring CO. I would like to thank teaching staff and especially Dr. Vivian Mozol who made my teaching experience particularly enjoyable and always provided me with sound advice. I would like to also thank Dr. Heikki M. Tuononen

who helped teach me computational chemistry. Finally, I would like to thank my supervisory committee, Dr. Roland Roesler whose door was always open to answer my questions and Dr. Jurgen Gailer who showed such an interest in my research as well as Dr. Darren Derksen and Dr. Belinda Heyne.

I am also grateful to Mr. Wade White, Dr. Michelle Forgeron and Mr. Johnson Li at the Instrumentation Facility in the Department of Chemistry (U of C) for their invaluable assistance. I would also like to thank Mark Toonen and Edward Cairns for their help with the design and building of glassware and light devices. I also would like to thank the Chemistry department administration and support staff.

To my family and friends who always support me no matter what. When times have been dark you have always helped me through and I am eternally grateful to you.

*I dedicate this to Deborah Waroquiers, we have been on quite the adventure together and  
I can never put into words how much you have helped me. Thank you.*

## Table of Contents

Abstract	II
Acknowledgements	III
Table of Contents	VI
List of Figures	IX
List of Tables	<b>Error! Bookmark not defined.</b>
List of Schemes	XVI
List of abbreviations and symbols	XVII
Chapter 1: Introduction	1
1.1 Cancer and Chemotherapy	1
1.1.1 History	1
1.1.2 Platinum and Chemotherapy	1
1.1.3 Resistance and Toxicity	3
1.2 Overcoming Resistance and Toxicity	5
1.2.1 Photodynamic Therapy (PDT)	5
1.2.2 Photoactivated Chemotherapy (PACT)	8
1.2.3 Sodium Thiosulfate (STS)	10
1.3 Rhenium	12
1.3.1 History	12
1.3.2 Chemotherapy	13
1.3.3 PDT and PACT	14
1.4 Scope of thesis	16
1.4.1 Single-Crystal X-ray diffraction	16
1.4.2 Photophysics	18
1.4.3 Cytotoxicity and cellular localization	24

Chapter 2: Cytotoxic and photophysical properties of Re(I) tricarbonyl complex coordinated <i>L</i> -cysteine and its derivative	28
2.1 Abstract	28
2.2 Introduction	29
2.3 Experimental Section	32
2.3.1 Materials	32
2.3.2 Cell Culture	32
2.3.3 Syntheses	33
2.3.3 Physical Measurements and Methods	35
2.4 Results and Discussion	41
2.4.1 Characterization of Re(I)-thiolate complexes <b>2</b> and <b>3</b>	41
2.4.2 Single Crystal X-ray Diffraction	43
2.4.3 Photophysical Properties	44
2.4.4 Singlet Oxygen Measurements	47
2.4.5 CO Release Measurements	49
2.4.6 Lipophilicity and partition coefficient (log P)	50
2.4.7 Cell Viability	51
2.4.8 Synchrotron-based X-ray Fluorescence Microscopy (XFM)	54
2.5 Conclusion	58
Chapter 3: The effect of sodium thiosulfate on cytotoxicity of a Re(I) tricarbonyl aqua complex	60
3.1 Abstract	60
3.2 Introduction	60
3.3 Experimental Section	64
3.3.1 Materials	64
3.3.2 Syntheses	64
3.3.3 Physical Measurements and Methods	65
3.4 Results and Discussion	69
3.4.1 Syntheses and characterization of the Re(I) thiosulfate complex	69
3.4.2 Single Crystal X-ray Diffraction	71
3.4.3 Lipophilicity and partition coefficient (log P)	73
3.4.3 Cell Viability	74



3.4.5 Synchrotron-based X-ray Fluorescence Microscopy (XFM)	76
3.6 Conclusion	81
Chapter 4 Future Work and Conclusions	82
4.1 Design of an ideal photosensitizer and PACT agent	82
Appendix	84
Chapter 2: Supporting Information	84
Syntheses	84
Physical Measurements and Methods	84
NMR Spectroscopy	86
FT-IR Spectroscopy	89
Thermogravimetric Analysis	90
Electrospray Ionization Mass-Spectrometry (ESI-MS)	91
Crystal Data	93
UV-Visible Absorbance Spectroscopy	95
Singlet Oxygen	98
UV Irradiation and CO Release	99
Lipophilicity and partition coefficient (log P)	101
Synchrotron-Based X-ray Fluorescence Microscopy (XFM)	104
Chapter 3: Supporting Information	108
Physical Measurements and Methods	108
NMR Spectroscopy	110
FT-IR Spectroscopy	111
Thermogravimetric Analysis (TGA)	112
Electrospray Ionization Mass-Spectrometry (ESI-MS)	113
Crystal Data	114
Lipophilicity and partition coefficient (log P)	123
Synchrotron Based X-ray Fluorescence Microscopy (XFM)	125
References	129

## List of Figures

<b>Figure 1.1</b> Chemical structure of cisplatin	2
<b>Figure 1.2</b> Chemical structures of carboplatin, nedaplatin and oxaliplatin	3
<b>Figure 1.3</b> Mechanism showing the energy states for a prototypical photosensitiser and its interaction with molecular oxygen ( $^3\text{O}_2$ ). Singlet states are denoted as S; triplet state is denoted by T. Transition states displayed are all spin allowed.	6
<b>Figure 1.4</b> Molecular orbital diagram displaying the generation of $^1\text{O}_2$	7
<b>Figure 1.5</b> Structure of the <i>tetrakis</i> -thiosulfato platinum(II) complex.	11
<b>Figure 1.6</b> Structure of <i>fac</i> -[Re(CO) <sub>3</sub> (N,N)(H <sub>2</sub> O)](OTf) and associated diimine ligands.	14
<b>Figure 1.7</b> Re(I) compounds with the general structure, <i>fac</i> -[Re(CO) <sub>3</sub> (N,N)(PR <sub>3</sub> )(CF <sub>3</sub> SO <sub>3</sub> )].	15
<b>Figure 1.8</b> Schematic displaying the experimental set up used for single-crystal X-ray diffraction.	17
<b>Figure 1.9</b> Simplified orbital/excited-state diagram of an octahedral d <sup>6</sup> metal complex where strong crystal field is assumed. $\uparrow\downarrow$ = electron with associated spin. $\uparrow$ = electron involved in electronic transition.	19
<b>Figure 1.10</b> General schematic of fluorescence spectroscopy apparatus.	20
<b>Figure 1.11</b> General schematic of singlet oxygen direct detection apparatus.	21
<b>Figure 1.12</b> a) Schlenk cuvette b) Irradiation apparatus equipped with 365 nm UV-A light (7.105 mW/ cm <sup>2</sup> ) placed at 7.2 cm from the sample position. c) General schematic of gas chromatography with a thermal conductivity detector (GC-TCD).	23
<b>Figure 1.14</b> Reduction of Resazurin in the presence of living cells to form Resorufin.	25
<b>Figure 1.15</b> Schematic of a synchrotron-based X-ray fluorescence microscopy experiment.	26

**Figure 2.1** Crystal Structure of  $\{fac-[Re(CO)_3(bpy)(HCys)]\}_4 \cdot 9H_2O$  (**2** + 1.75  $H_2O$ ). Ellipsoids are drawn at the 50% probability level.  $H_2O$  solvent molecules and H atoms have been omitted for clarity. 43

**Figure 2.2** UV-vis absorbance spectra of 50  $\mu M$  MeOH solutions of **1**, **2** and **3**. 45

**Figure 2.3** Excitation and emission spectra of **1**, **2** and **3** in MeOH at 298 K. 46

**Figure 2.4** Dose-response curve of **1**, **2** and cisplatin at 24 hrs and 48 hrs. Data are represented as means  $\pm$  standard deviations from three independent experiments with 9 biological replicates per concentration level. Data were analyzed with a one-way ANOVA followed by Dunnet post-tests from comparisons between treated and control cells. 52

**Figure 2.5** Optical micrographs, and XRF elemental distribution map of MDA-MB-231 cells treated for 6 h with **1**, **2** and DMEM as a control. The maximum elemental area densities (quantified from standards and expressed in  $\mu g\ cm^{-2}$ ) are given in the bottom of each map. 55

**Figure 2.6** Intracellular content of P, S, Cl, K, Ca, Fe, Cu, Zn, and Re obtained by quantification using XFM as compared with the nuclear content of MDA-MB-231 cells treated for 6 h with control (n=5) as well as 20  $\mu M$  solutions of **1** in DMEM (n=4) and **2** in 1.5% EtOH in DMEM (n=5). Error bars represent standard deviations. Data were analyzed with a one-way ANOVA followed by Tukey post-tests: \*p < 0.05; \*\* p < 0.01; \*\*\* p < 0.001 from comparisons between treated and control cell/nucleus regions. 56

**Figure 3.1** Crystal Structure of  $Na(fac-[Re(CO)_3(bpy)(S_2O_3)]) \cdot 1.75H_2O \cdot C_2H_5OH$  (**4** + 0.75  $H_2O$  +  $C_2H_5OH$ ) Ellipsoids are drawn at the 50% probability level.  $H_2O$  and EtOH solvent molecules and H atoms attached to C atoms have been omitted for clarity. 71

**Figure 3.2** Crystal Structure of  $fac-[Re(CO)_3(bpy)(H_2O)](fac-[Re(CO)_3(bpy)(S_2O_3)]) \cdot 4H_2O$  (**5**) Ellipsoids are drawn at the 50% probability level.  $H_2O$  solvent molecules and H atoms attached to C atoms have been omitted for clarity. 72

**Figure 3.3** Cell viability data in MDA-MB-231 breast cancer cells when treated with **1**, **4** and cisplatin for 24 h and 48 h. Data are represented as means  $\pm$  standard deviations from three independent experiments with 9 biological replicates per concentration level. Data

were analyzed with a one-way ANOVA followed by Dunnet post-tests: \* $p < 0.05$ ; \*\*  $p < 0.01$ ; \*\*\*  $p < 0.001$  from comparisons between treated and control cells. 75

**Figure 3.4** Optical micrographs (top left), and XRF elemental distribution map of MDA-MB-231 cells treated for 6 h with **1** (top), **4** and DMEM. The maximum elemental area densities (quantified from standards and expressed in  $\mu\text{g cm}^{-2}$ ) are given in the bottom of each map. 78

**Figure 3.5.** Intracellular content of P, S, Cl, K, Ca, Fe, Cu, Zn, and Re obtained by quantification using XFM as compared with the nuclear content of MDA-MB-231 cells treated for 6 h with control (n=5) as well as 20  $\mu\text{M}$  solutions of **1** (n=4) and **4** (n=4) in DMEM. Error bars represent standard deviations. Data were analyzed with a one-way ANOVA followed by Tukey post-tests: \* $p < 0.05$ ; \*\*  $p < 0.01$ ; \*\*\*  $p < 0.001$  from comparisons between treated and control cell/nucleus regions. 80

**Figure A2.1**  $^1\text{H}$  and  $^{13}\text{C}$  NMR of *fac*-[Re(CO)<sub>3</sub>(bpy)(H<sub>2</sub>O)](CF<sub>3</sub>SO<sub>3</sub>) (**1**) in D<sub>2</sub>O. 86

**Figure A2.2**  $^1\text{H}$  and  $^{13}\text{C}$  NMR of *fac*-[Re(CO)<sub>3</sub>(bpy)(HCys)].0.5H<sub>2</sub>O (**2**) in CD<sub>3</sub>OD. 87

**Figure A2.3**  $^1\text{H}$  NMR spectrum of Na(*fac*-[Re(CO)<sub>3</sub>(bpy)(NAC)]) (**3**) in D<sub>2</sub>O and CD<sub>3</sub>OD. 88

**Figure A2.4** FT-IR spectra of **1**, **2** and **3** and corresponding  $\nu(\text{CO})$  vibrations. 89

**Figure A2.5** Thermogravimetric analysis of **2** and **3**. 90

**Figure A2.6** ESI-mass spectra of **2** in MeOH + ion mode, – ion mode. Peak assignments can be found in Table A2.1. 91

**Figure A2.7** ESI-mass spectra of **3** in MeOH + ion mode, – ion mode. Peak assignments can be found in Table A2.2. 92

**Figure A2.8** UV-visible absorbance spectrum of **1** in MeOH. Assignment of bands and epsilon ( $\epsilon$ ) values shown in Table A2.5. 95

**Figure A2.9** UV-visible absorbance spectrum of **2** in MeOH. Assignment of bands and epsilon ( $\epsilon$ ) values shown in Table A2.6. 96

**Figure A2.10** UV-visible absorbance spectroscopy of **3** in MeOH. Assignment of bands and epsilon ( $\epsilon$ ) values shown in Table A2.7. 97

**Figure A2.11** Time-resolved decay curves probed at maximum wavelength after 355 nm laser excitation in an MeOH solution at 298 K of **1**, **2** and **3**. 98

**Figure A2.12** UV-visible absorbance spectra of **1**, **2** and **3** at the respective concentration of 25, 12.5 and 20  $\mu\text{M}$  in MeOH when irradiated in a Schlenk cuvette using a UV-A hand lamp (365 nm, 7.105 mW/cm<sup>-2</sup>) under Ar over the course of 2hr. 99

**Figure A2.13** UV-visible absorbance spectra of **1** in H<sub>2</sub>O and **2** in aqueous EtOH to obtain a calibration curve. Assignment of epsilon ( $\epsilon$ ) values at 243 nm shown in Table A2.9. 101

**Figure A2.14** UV-visible absorbance spectra of **1** in aqueous phase of the above solutions A - D (water/ n-octanol mixtures) obtained after shaking for 24 hr at 25 C. 102

**Figure A2.15** UV-visible absorbance spectra of **2** in aqueous phase of the above solutions E - I (water + 1.5% EtOH/ n-octanol mixtures) obtained after shaking for 24 hr at 25 C. 103

**Figure A2.16** Optical micrographs and scattered X-ray (XS) and XRF elemental distribution map of MDA-MB-231 cells treated with **1** for 6 h. The maximum elemental area densities (quantified from standards and expressed in  $\mu\text{g cm}^{-2}$ ) are given in the bottom of each map. The scale bar represents 10  $\mu\text{m}$  unless otherwise indicated. 104

**Figure A2.17** Optical micrographs and scattered X-ray (XS) and XRF elemental distribution map of MDA-MB-231 cells treated with **2** for 6 h. The maximum elemental area densities (quantified from standards and expressed in  $\mu\text{g cm}^{-2}$ ) are given in the bottom of each map. The scale bar represents 10  $\mu\text{m}$  unless otherwise indicated. 105

**Figure A2.18** Optical micrographs and scattered X-ray (XS) and XRF elemental distribution map of MDA-MB-231 cells treated with DMEM for 6 h. The maximum elemental area densities (quantified from standards and expressed in  $\mu\text{g cm}^{-2}$ ) are given in the bottom of each map. The scale bar represents 10  $\mu\text{m}$  unless otherwise indicated. 106

**Figure A2.19** XFM spectra of MDA-MB-231 sample cells treated for 6 hr with 20  $\mu\text{M}$  solutions of **1** and **2** or in DMEM. Each figure shows the fit to the spectrum and the contribution of the K $\alpha$  peaks used in the fitting with their corresponding labelling. 107

**Figure A3.1** <sup>1</sup>H NMR and <sup>13</sup>C NMR spectra of Na(*fac*-[Re(CO)<sub>3</sub>(bpy)(S<sub>2</sub>O<sub>3</sub>)])·H<sub>2</sub>O (**4**) in D<sub>2</sub>O. 110

<b>Figure A3.2</b> FT-IR spectrum of <b>4</b> and corresponding $\nu(\text{CO})$ vibrations.	111
<b>Figure A3.3</b> Thermogravimetric analysis (TGA) of <b>4</b> .	112
<b>Figure A3.4</b> ESI-mass spectra of <b>4</b> in $\text{H}_2\text{O}$ + ion mode, – ion mode. Peak assignments can be found in Table A3.1.	113
<b>Figure A3.5</b> UV-visible absorbance spectrum of <b>4</b> in $\text{H}_2\text{O}$ to obtain a calibration curve. Assignment of epsilon ( $\epsilon$ ) values at 243 nm shown in Table A3.9. Epsilon ( $\epsilon$ ) values at 243 nm shown in Table A3.9.	123
<b>Figure A3.6</b> UV-visible absorbance spectra of <b>4</b> in aqueous phase of the above solutions J - N (water/ n-octanol mixtures) obtained after shaking for 24 hr at 25 C.	124
<b>Figure A3.7</b> Optical micrographs and scattered X-ray (XS) and XRF elemental distribution map of MDA-MB-231 cells treated with <b>1</b> for 6 h. The maximum elemental area densities (quantified from standards and expressed in $\mu\text{g cm}^{-2}$ ) are given in the bottom of each map. The scale bar represents 10 $\mu\text{M}$ unless otherwise indicated.	125
<b>Figure A3.8</b> Optical micrographs and scattered X-ray (XS) and XRF elemental distribution map of MDA-MB-231 cells treated with <b>4</b> for 6 h. The maximum elemental area densities (quantified from standards and expressed in $\mu\text{g cm}^{-2}$ ) are given in the bottom of each map. The scale bar represents 10 $\mu\text{M}$ unless otherwise indicated.	126
<b>Figure A3.9</b> Optical micrographs and scattered X-ray (XS) and XRF elemental distribution map of MDA-MB-231 cells treated with DMEM for 6 h. The maximum elemental area densities (quantified from standards and expressed in $\mu\text{g cm}^{-2}$ ) are given in the bottom of each map. The scale bar represents 10 $\mu\text{M}$ unless otherwise indicated.	127
<b>Figure A3.10</b> XFM spectra of MDA-MB-231 sample cells treated for 6 hr with 20 $\mu\text{M}$ solutions of <b>1</b> and <b>4</b> or in DMEM (bottom). Each figure shows the fit to the spectrum and the contribution of the $\text{K}\alpha$ peaks used in the fitting with their corresponding labelling.	128

## List of Tables

<b>Table 2.1</b> Photophysical properties of complexes <b>1-3</b> in MeOH*	44
<b>Table 2.2</b> Singlet oxygen quantum yields ( $\Phi\Delta$ ) of <b>1</b> , <b>2</b> and <b>3</b> in air-equilibrated MeOH at 298 K	48
<b>Table 2.3</b> Partition coefficient and log P values of complexes <b>1</b> and <b>2</b>	50
<b>Table 2.4</b> IC <sub>50</sub> values of <b>1</b> , <b>2</b> and cisplatin in MDA-MB-231 breast cancer cells (see Fig 2.4).	53
<b>Table 3.1</b> Partition coefficient and log P values of complexes <b>1</b> and <b>4</b> .	74
<b>Table 3.2</b> IC <sub>50</sub> values of <b>1</b> , <b>4</b> and cisplatin against MDA-MB-231 breast cancer cells. Data are represented as means $\pm$ standard deviations from three independent experiments with 9 biological replicates per concentration level.	76
<b>Table A2.1</b> Assignments of mass ions in the ESI-MS as shown in Figure A2.6.	91
<b>Table A2.2</b> Assignment of mass ions of ESI-MS as shown in Figure A2.7.	92
<b>Table A2.3</b> Crystal Data and Structure Refinement for Complex <b>2</b> + 1.75 H <sub>2</sub> O.	93
<b>Table A2.4.</b> Selected Bond Lengths (Å) and Angles (deg) for Complex <b>2</b> + 1.75 H <sub>2</sub> O	94
<b>Table A2.5</b> Assignment of bands and epsilon ( $\epsilon$ ) values of UV-visible absorbance spectra as shown in Figure A2.8.	95
<b>Table A2.6</b> Assignment of bands and epsilon ( $\epsilon$ ) values of UV-visible absorbance spectra as shown in Figure A2.9.	96
<b>Table A2.7</b> Assignment of bands and epsilon ( $\epsilon$ ) values of UV-visible absorbance spectra as shown in Figure A2.10.	97
<b>Table A2.8</b> CO release measured using gas chromatography with thermal conductivity detector (GC-TCD) of <b>1</b> , <b>2</b> and <b>3</b> . 50 $\mu$ M concentrations of each complex in MeOH were irradiated in a Schlenk cuvette using a UVA hand lamp (365 nm, 7.105 mW/cm <sup>-2</sup> ) under Ar.	100
<b>Table A2.9</b> Assignment of bands and epsilon ( $\epsilon$ ) values of UV-visible absorbance spectra as shown in Figure A2.13.	101

	104
<b>Table A3.1</b> Assignments of mass ions in the ESI-MS spectra as shown in Figure A3.4.	113
<b>Table A3.2</b> Crystal Data and Structure Refinement for Complex <b>4</b> + 0.75H <sub>2</sub> O · C <sub>2</sub> H <sub>5</sub> OH.	114
<b>Table A3.3</b> Selected Bond Lengths (Å) for Complex <b>4</b> + 0.75H <sub>2</sub> O · C <sub>2</sub> H <sub>5</sub> OH.	115
<b>Table A3.4</b> Selected Bond Angles (deg) for Complex <b>4</b> + 0.75H <sub>2</sub> O · C <sub>2</sub> H <sub>5</sub> OH.	116
<b>Table A3.5</b> Crystal Data and Structure Refinement for Complex <b>5</b> + 4H <sub>2</sub> O.	117
<b>Table A3.6</b> Selected Bond Lengths (Å) for Complex <b>5</b> + 4 H <sub>2</sub> O.	118
<b>Table A3.7</b> Selected Bond Angles (deg) for Complex <b>5</b> + 4H <sub>2</sub> O.	120
<b>Table A3.8</b> Survey of Re(I) tricarbonyl complexes with S coordinating ligand in CSD version 5.38 ( 2017).	122
<b>Table A3.9</b> Assignment of bands and epsilon (ε) values of UV-visible absorbance spectra as shown in Figure A3.5.	123



## List of Schemes

**Scheme 1.1** General concept of PhotoCORMs: Photo-excitation of metal-carbonyl complex (**1**) leads to release of one or more CO molecules, forming an intermediate species (**2**) which then binds to a solvent molecule forming a final product (**3**). Scheme adapted from literature. 9

**Scheme 2.1** Synthesis of *fac*-[Re(CO)<sub>3</sub>(bpy)(H<sub>2</sub>O)](CF<sub>3</sub>SO<sub>3</sub>) (**1**) starting from Re(CO)<sub>5</sub>Cl and the subsequent reactions between **1** and *L*-cysteine or N-acetyl-*L*-cysteine. 41

**Scheme 3.1** Synthesis of **1** from Re(CO)<sub>5</sub>Cl and the subsequent reaction between **1** and sodium thiosulfate to form **4**. 69

## List of abbreviations and symbols

$^1\text{O}_2$	singlet oxygen
$^3\text{O}_2$	molecular oxygen
$^3\text{PS}^*$	triplet photosensitizer
5-FU	fluorouracil
7-MeG	7-methylguanine
9-MeG	9-methylguanine
ampy	2-aminomethylpyridine
ANOVA	analysis of variance
ATCC	American Type Culture Collection
bpy	2,2'-bipyridine
CAFs	cancer associated fibroblasts
CD3OD	deuterated methanol
COHb	carboxyhaemoglobin
CT	charge transfer
d	doublet
D <sub>2</sub> O	deuterated water
dd	doublet of doublets
ddd	doublet of doublet of doublets
DFT	density functional theory
DMEM	Dulbecco's Modified Eagles Medium
dmphen	2,9-dimethyl-1,10-phenantroline
DNA	deoxyribonucleic acid
DPBS	Dulbecco's phosphate-buffered saline
D-Pen	D-Penicillamine
dt	doublet of triplets
ESI-MS	electrospray ionization mass spectrometry
FT-IR	Fourier-transform infrared spectroscopy
GC-TCD	gas chromatography with a thermal conductivity detector

H <sub>2</sub> Cys	<i>L</i> -cysteine
H <sub>2</sub> NAC	N-acetyl- <i>L</i> -cysteine
H <sub>2</sub> O <sub>2</sub>	hydrogen peroxide
HO•	hydroxyl radical
HOMO	highest occupied molecular orbital
HOs	haemoxygenases
IC	internal conversion
ICP-MS	Inductively coupled plasma mass spectrometry
IL	interligand
ISC	intersystem crossing
LC	ligand centred
Log P	partition coefficient
LMCT	ligand-to-metal charge transfer
LUMO	lowest unoccupied molecular orbital
MC	metal centred
MLCT	metal-to-ligand charge transfer
MSC	mesenchymal stem cells
MTs	metallothioneins
NADH	Nicotinamide adenine dinucleotide
NADP	Nicotinamide adenine dinucleotide phosphate
NMR	Nuclear Magnetic Resonance
O <sub>2</sub> • <sup>-</sup>	superoxide
OB-24	2-[2-(4-bromophenyl)ethyl]-2-[(1H-imidazol-1-yl)-methyl]-1,3-dioxolane hydrochloride
PACT	Photoactivated Chemotherapy
PDT	Photodynamic Therapy
phen	1,10-phenantroline
PS	Photosensitizer
py	pyridine
ROS	reactive oxygen species
s	singlet

$S_0$	singlet ground state
$S_1$	singlet excited state
STS	sodium thiosulfate
t	triplet
$T_1$	triplet excited state
td	triplet of doublets
UV	Ultra Violet
XAS	X-ray Absorption Spectroscopy
XFM	X-ray fluorescence microscopy
$\varepsilon$	molar extinction coefficient
$\Phi_{\text{em}}$	fluorescence quantum yield
$\Phi_{\Delta}$	quantum yield

# **Chapter 1: Introduction**

## **1.1 Cancer and Chemotherapy**

### *1.1.1 History*

Cancer is a well-known and detrimental affliction that comes at a great cost humankind. There are over 100 distinct cancer types, and tumour subtypes which are organ specific resulting in a range of different treatments.<sup>1</sup> The first reported cases of cancer date back to ancient Egyptian times of around 1600 B.C. with evidence of human bone cancer discovered in mummies and in ancient manuscripts.<sup>2</sup> Evidence of breast cancer has also been reported during this era with records showing the only available treatments being palliative.<sup>2</sup> As time has progressed, cancer continued to be a growing issue. In 2014 alone an estimated 8.2 million cancer-related deaths were reported.<sup>3</sup> The number of people afflicted by cancer is estimated to be 14 million worldwide with this number set to rise to 22 million over the course of the next two decades.<sup>3</sup> This increase can be associated with a number of factors including environmental ones, such as tobacco smoking, pollution and increased life span, as well as genetic factors such as germ-line mutations of the BRCA1 gene, which result in the development of both familial breast and ovarian cancer.<sup>4, 5</sup> Due to the prevalence and increase of cancer incidences and deaths, the need for successful treatments is apparent.

### *1.1.2 Platinum and Chemotherapy*

Methods of cancer treatment range from chemotherapy, hormonal therapy, immunotherapy, radiotherapy and surgical techniques. Chemotherapy began its inception in the early 1900s through the work of Paul Elrich, a German chemist who first coined the

term with the definition meaning the use of chemicals to treat disease.<sup>6</sup> For example, the discovery of arsphenamine (Salvarsan) for the treatment of syphilis led to him being awarded the Nobel Prize in Physiology and Medicine in 1908.<sup>7</sup> An important milestone in the history of chemotherapy was during 1965, when Barnett Rosenberg made the observation that during electrolysis, Pt electrodes in a solution containing  $\text{NH}_3$  and  $\text{Cl}^-$  inhibited cell division in *Escherichia coli*.<sup>8</sup> The significance of this experiment was that one of the bi-products of the reaction was cisplatin (Figure 1.1). Since its discovery, cisplatin has had an unprecedented amount of success and is used to treat a variety of cancers such as ovarian, cervical, breast, bladder, oesophageal and lung cancer as well as mesothelioma, brain tumours and neuroblastoma.<sup>9</sup> When detected early, patients with testicular cancer who are treated with cisplatin have a near 100% cure rate, displaying its impressive success.<sup>10</sup>

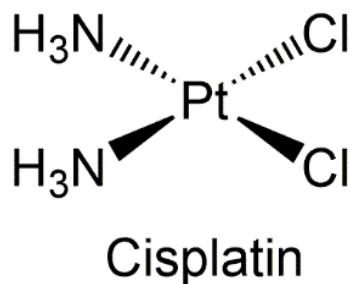


**Figure 1.1** Chemical structure of cisplatin

When intravenously administered, cisplatin is subjected to chloride concentrations of up to 100 mM in the blood plasma, which enables it to reach cells without undergoing hydrolysis of the labile chloro ligands.<sup>11</sup> Once in the cell, the concentration of chloride ions drops significantly to only a few millimolar (~25 mM) resulting in the chloro ligands being displaced to form an aquated species, which is the active form of the drug.<sup>11</sup> The active

form is now positively charged, resulting in an electrostatic attraction between the N7 position of purine DNA base pairs.<sup>12</sup> Upon binding to DNA, the formation of 1,2-intrastrand adducts between two guanine bases [*cis*-Pt(NH<sub>3</sub>)<sub>2</sub>d(pGpG), 1,2-GG], or adenine and guanine [*cis*-Pt((NH<sub>3</sub>)<sub>2</sub>d(pApG), 1,2-AG)] occurs, as shown through *in vitro* studies.<sup>13</sup> This then causes the distortion of DNA, disrupting its repair mechanisms and interfering with cell division, which ultimately induces apoptosis. As well as cisplatin, a number of other platinum-based complexes have been developed including Oxaliplatin, Carboplatin and Nedaplatin (Figure 1.2).<sup>11</sup>

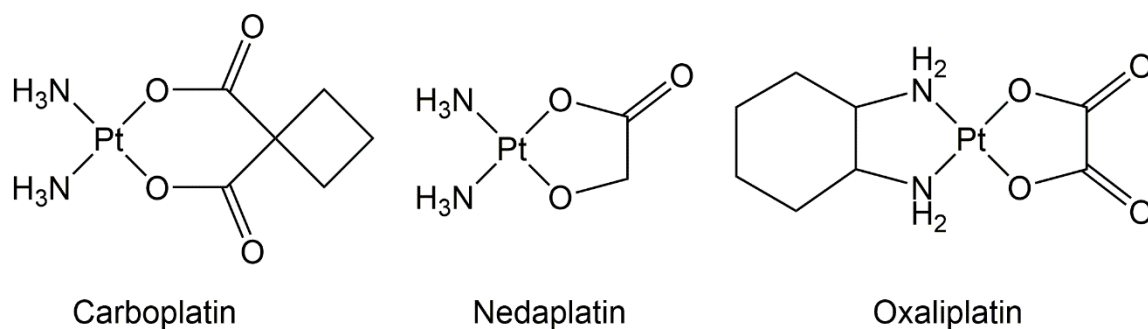


**Figure 1.2** Chemical structures of carboplatin, nedaplatin and oxaliplatin

The development of derivatives of cisplatin was done in an effort to reduce unwanted toxic side effects (eg. nephrotoxicity (kidney damage) and gastrointestinal toxicity.)<sup>14</sup> This, along with the development of resistance mechanisms hinder the efficacy of such platinum-based drugs.

### 1.1.3 Resistance and Toxicity

The success of cisplatin is undeniable, which is exemplified by its use in 32 out of 78 cancer regimes in combination with other drugs as listed in Martindale.<sup>15</sup> Despite its

success, there are drawbacks such as severe toxic side effects and the development of resistance mechanisms.<sup>9</sup> The issue of toxic side effects arises due to the non-specificity of cisplatin, meaning it cannot differentiate between normal and cancerous cells, thus, damaging all cells indiscriminately. The side effects can range from nausea, vomiting, myelosuppression, immunosuppression, fatigue, diarrhea, peripheral neuropathy, alopecia, nephrotoxicity, neurotoxicity (damage of neurons) and ototoxicity (hearing loss).<sup>16-20</sup> This limits the efficacy of the drug and decreases the suitability for a number of patients. For instance, over 70% of pediatric patients treated with cisplatin will experience renal dysfunction, and over 60% will develop irreversible hearing loss.<sup>21-23</sup> Not only is cisplatin hindered by toxic side effects but the existence of primary and development of secondary resistance mechanisms hinder its efficacy against a number of malignancies.<sup>24</sup> This is cause for concern as patients who have undergone treatment with cisplatin are at risk of relapse due to the reduced effectiveness of the drug. For instance, the development of chemoresistance to platinum-based drugs in patients with reoccurring cases of advanced ovarian cancer results in 5-year survival of only 30% of patients.<sup>25</sup> There have also been a number of cisplatin resistance mechanisms identified in platinum-resistant cell lines (e.g. A2780cis, which exhibit decrease cisplatin uptake due to increased efflux from the cell).<sup>26</sup> Mouse models have been used to determine the role of cancer-associated fibroblasts (CAFs), astrocytes and mesenchymal stem cells (MSCs) in the development of resistance to cancer therapies.<sup>27</sup> The models have shown that the close presence of astrocytes to brain metastases derived from either human breast or lung cancers will induce the expression of survival genes in tumour cells of close proximity, which provides protection to the tumour cells from drugs such as cisplatin as well as paclitaxel, vinblastine and fluorouracil (5-



FU).<sup>28</sup> Other studies have shown that by intravenously administering MSCs before beginning cisplatin therapy, the antitumor effect of the drug is reduced in a cell-dose dependent manner.<sup>29</sup> Resistance of tumour cells to other chemotherapeutic drugs such as 5-FU and irinotecan were promoted by the activation of MSCs by cisplatin. This was partly attributed to the secretion of polyunsaturated fatty acids by MSCs, which has also been seen in cancer patients being treated with chemotherapy.<sup>29</sup> It was suggested that the polyunsaturated acids did not directly induce tumour resistance, but instead boosted host intermediate factors which potentially prevented apoptosis in cells exposed to chemotherapeutic drugs.<sup>29</sup> With the negative impact of toxic side effects and resistance mechanisms, there have been many efforts underway to circumvent such issues.

## **1.2 Overcoming Resistance and Toxicity**

### ***1.2.1 Photodynamic Therapy (PDT)***

One method that uses the concept of introducing an organic/inorganic compound into the body to treat cancer is Photodynamic Therapy (PDT). This differs from traditional chemotherapy in that the organic/inorganic compound used, otherwise known as a photosensitizer (PS), is initially non-toxic upon introduction to the body. When the compound is exposed to light it interacts with intracellular oxygen, producing cytotoxic products, inducing localized cell death. By using this approach, issues such as toxicity and resistance that are associated with traditional chemotherapy can be circumvented.<sup>26, 30, 31</sup> This is achieved using 3 different mechanisms of action: generation of reactive oxygen species (ROS) and singlet oxygen ( $^1\text{O}_2$ ) which disrupt the delicate redox balance in the cell; damaging of cellular vasculature leading to tumour infarction; eliciting an immune

response against the tumour cells.<sup>32, 33</sup> The properties of metal complexes have particular benefits making them suitable for PDT. For instance, metal complexes offer a diverse range of excited states that enhance their photochemical properties and possess a relative non-lability in various environments, making them suitable for use in PDT.<sup>10, 34</sup> The mechanism by which PDT works is that upon irradiation with a light of a particular wavelength, the PS undergoes a series of photophysical processes, ultimately leading to the production of cytotoxic products (Figure 1.3).

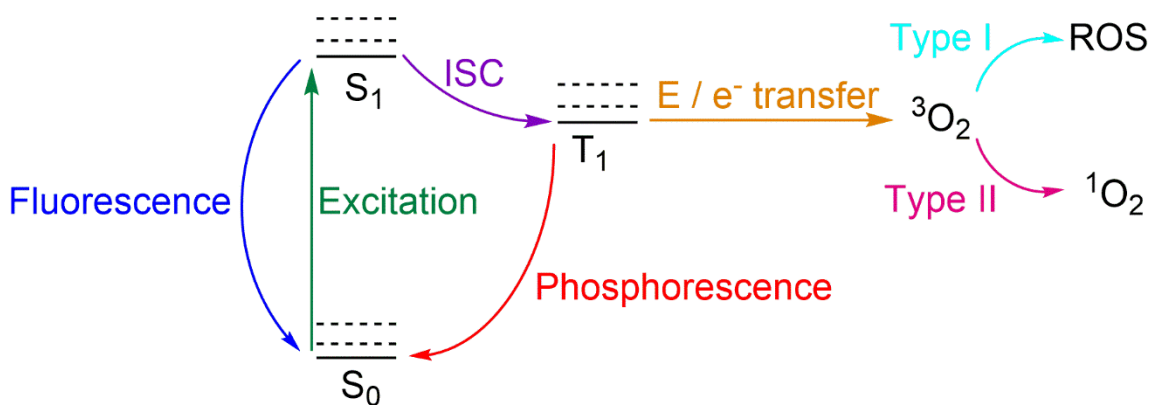


**Figure 1.3** Mechanism showing the energy states for a prototypical photosensitiser and its interaction with molecular oxygen ( $^3\text{O}_2$ ). Singlet states are denoted as S; triplet state is denoted by T. Transition states displayed are all spin allowed.

Upon excitation, the PS absorbs photons of a specific wavelength and is promoted from the ground state ( $\text{S}_0$ ) into different excited states ( $\text{S}_1$ ,  $\text{S}_2$ ) composed of different vibrational sub-levels. The PS then undergoes various processes, such as internal conversion (IC) and vibrational relaxation leading to the population of the first singlet excited state ( $\text{S}_1$ ). Decay back to  $\text{S}_0$  ( $\text{S}_1 \rightarrow \text{S}_0$ ) can occur by a process known as fluorescence, which involves the release of a photon, or through heat dissipation.<sup>35</sup> Alternatively, the PS can enter a triplet state ( $\text{S}_1 \rightarrow \text{T}_1$ ), which exists at a lower energy, via a process known as intersystem crossing (ISC).<sup>36</sup> The association of  $\text{d}^6$ -metal complexes

photochemical properties with this low lying triplet state has been proposed a useful model for studying inorganic systems.<sup>34</sup> The transition between the triplet and singlet states are forbidden resulting in a long-lived triplet state which is beneficial for a PS since it is in this state that energy/electrons can be transferred to molecular oxygen ( $^3\text{O}_2$ ) present in the cell. If the PS does not transfer energy/electrons to  $^3\text{O}_2$  it can alternatively release a photon in a process known as phosphorescence.<sup>35</sup> Once the excited triplet state photosensitiser ( $^3\text{PS}^*$ ) transfers energy to  $^3\text{O}_2$ , a Type I or Type II reaction is initiated. The Type I reaction involves the transfer of electrons to a substrate resulting in the production of ROS such as superoxide ( $\text{O}_2^{\bullet-}$ ), hydrogen peroxide ( $\text{H}_2\text{O}_2$ ), and hydroxyl radicals ( $\text{HO}^\bullet$ ). The Type II reaction involves the transfer of energy to  $^3\text{O}_2$ , which ultimately produces the highly reactive and cytotoxic singlet oxygen ( $^1\text{O}_2$ ) species (Figure 1.4).

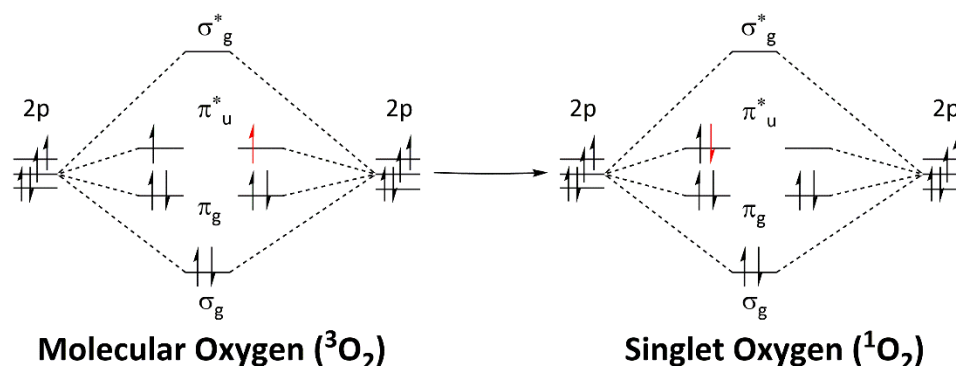


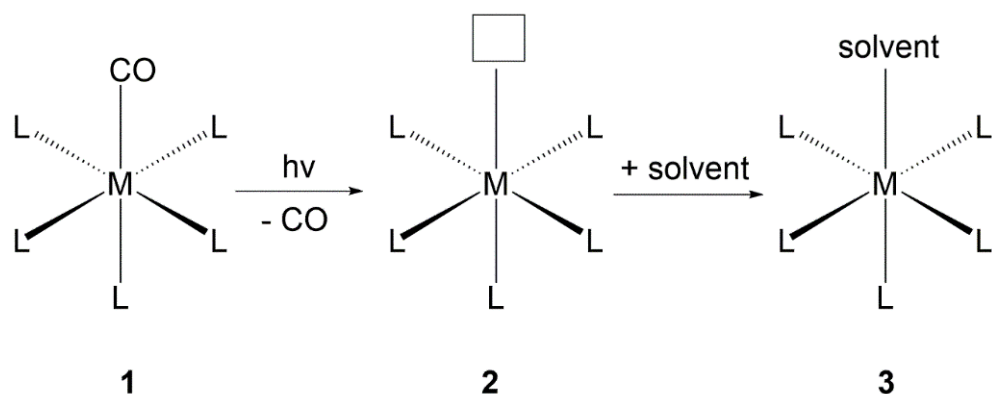
**Figure 1.4** Molecular orbital diagram displaying the generation of  $^1\text{O}_2$

The Type II reaction (Figure 1.3) is the predominant reaction that occurs during PDT and its product  $^1\text{O}_2$ , is a highly reactive antiproliferative species, which activates cellular pathways that initiate and ultimately lead to apoptosis.<sup>37</sup> When the  $^3\text{PS}^*$  interacts with  $^3\text{O}_2$  the spin of one of its outermost electrons in the  $\pi^*$  antibonding orbital is inverted and is paired with the electron present in the other outermost  $\pi^*$  antibonding orbital (Figure

1.4).<sup>38</sup> The pairing of electrons in only one of the outermost  $\pi^*$  antibonding orbital is a violation of Hund's rule, making it relatively unstable. Hund's rule states that every orbital in a subshell is occupied singularly with one electron before any orbital is occupied by two electrons and that all electrons have the same spin in singularly occupied orbitals.<sup>39</sup> As it is unstable,  $^1\text{O}_2$  has a short-lived lifetime in a range of solvents, such as 10-100  $\mu\text{s}$  in organic solvents and around 2  $\mu\text{s}$  in aqueous solvents.<sup>38</sup> Due to its fast reactivity,  $^1\text{O}_2$  can deliver highly selective oxidative damage to the tumour cell which is a beneficial feature for PDT as it reduces damage to neighbouring non-cancerous cells.

### *1.2.2 Photoactivated Chemotherapy (PACT)*

Using the same principles at PDT, the photoactivation of a metal complex can not only induce the production of ROS, but it can also initiate the photorelease of a small cytotoxic molecule. One such family of metal complexes are known as PhotoCORMs (photoactive CO releasing molecules), which was a term coined by Ford and co-workers.<sup>40</sup> <sup>41</sup> PhotoCORMs work in a similar fashion to PDT, as the metal-carbonyl complex remains inactive in the dark and stable in aqueous media. Then upon photo-excitation of a specific wavelength, one or more carbonyl groups can be released to interact with their intended biological target. The remaining metal fragment then likely binds a solvent molecule, thus completing its coordination sphere (Scheme 1.1).



**Scheme 1.1** General concept of PhotoCORMs: Photo-excitation of metal-carbonyl complex (**1**) leads to release of one or more CO molecules, forming an intermediate species (**2**) which then binds to a solvent molecule forming a final product (**3**). Scheme adapted from literature.<sup>42</sup>

The biological effects of CO are more commonly known due to its affinity for haemoglobin, a protein responsible for the transport of oxygen from the lungs, to other tissues in the body. The affinity of CO to haemoglobin, is approximately 220 times stronger than that of oxygen and the reaction between the two forms the product carboxyhemoglobin (COHb).<sup>43</sup> Once up to 50-60% of total haemoglobin has been occupied by CO, the body can fall into a coma and/or experience convulsions and respiratory depression, all of which are potentially fatal.<sup>44</sup> Despite this, high concentrations of COHb aren't necessarily associated with inhibition of the transport of oxygen in the bloodstream.<sup>45</sup> This has led to an exploration of the medicinal properties of CO, with cancer therapy being one area of investigation.

CO can also be produced in the body via an endogenous process which occurs through the breakdown of heme. In the presence of the cofactors, NADP and O<sub>2</sub>, the porphyrin IX ring of heme collapses producing CO, Fe<sup>2+</sup>, biliverdin IX and then bilirubin

IX.<sup>46</sup> This process produces approximately 16  $\mu\text{mol CO/h}$ . The reaction itself is catalyzed by a family of enzymes known as hemeoxygenases (HOs).<sup>46</sup> Three isoforms of the enzyme have been identified being HO-1, HO-2 and HO-3. HO-1, which is mainly found in the spleen and liver, is of interest in cancer therapy as an antitumor target. The overexpression of HO-1 in tumour types, such as pancreatic and prostate cancer, Kaposi sarcoma and melanoma have been previously demonstrated.<sup>47</sup> The inhibition of HO-1 using 2-[2-(4-bromophenyl)ethyl]-2-[(1H-imidazol-1-yl)-methyl]-1,3-dioxolane hydrochloride (OB-24) has been shown to limit advanced prostate growth and metastasis in mice.<sup>48</sup> In addition, the co-administration of OB-24 with paclitaxel (Taxol) led to an improvement of antitumor effects. This highlights the oncological relevance of targeting the HO-1/CO system. Additionally, increased levels of CO ( $\geq 300$  ppm) have been shown to shut down respiration and release cytochrome *c* from the mitochondrial membrane which then initiates apoptotic cascade via caspase activation.<sup>49</sup> Despite this, photoCORMs remain in the preclinical stage but this is an ever-expanding area of research with promising cancer therapy applications.

### *1.2.3 Sodium Thiosulfate (STS)*

When considering the issue of toxicity, one method of combatting this is the co-administration of an ameliorating agent to negate toxic side effects. The combination of cisplatin and sodium thiosulfate (STS) was shown to protect against nephrotoxicity in mice.<sup>45</sup> This work led to clinical trials which displayed a reduction of nephrotoxicity in patients treated intravenously with STS after the administration of cisplatin and allowed the overall dosage of cisplatin to be increased.<sup>46, 47</sup> More recently, this method has been used to combat ototoxicity (hearing loss) in pediatric patients.<sup>50</sup> This study involved the use of randomized pediatric patients with localized hepatoblastoma who were undergoing

treatment with cisplatin with or without coadministration of STS. The results indicated that the delayed administration of STS results in a significant lowering of cisplatin-induced hearing loss incidences.<sup>50</sup> In patients treated with both cisplatin and STS, there was a 48% reduction in risk of hearing loss, as well as hearing loss of grade 1 or higher was found to occur in 63% of pediatric patients who did not receive STS compared to only 33% of patients who did.<sup>50</sup> This provides evidence of the success of using a combination of cisplatin and STS. Investigations into the chemistry of the interaction between cisplatin and sodium thiosulfate using X-ray absorption spectroscopy (XAS) and density functional theory (DFT) showed the formation of a tetrakis-thiosulfato platinum(II) entity (Figure 1.5).<sup>49</sup>

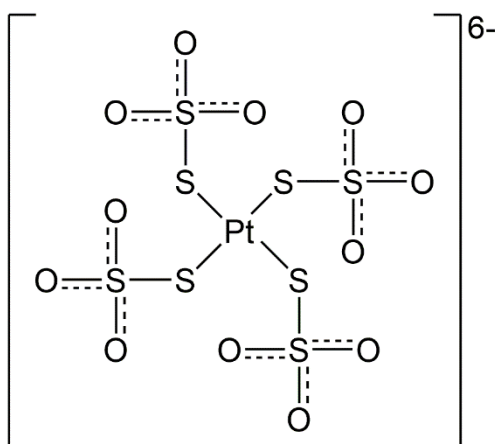


**Figure 1.5** Structure of the *tetrakis*-thiosulfato platinum(II) complex.<sup>51</sup>

The inactivation of a certain amount of toxic aquated cisplatin products by STS while leaving intact enough to exhibit the desired anti-cancer activity leading to beneficial therapeutic effects was thought to be the mode of action.<sup>51</sup> Further work still remains in the

exploration of cisplatin in the body but the study provides an interesting method into exploring the structural characterization of such products.

## 1.3 Rhenium

### 1.3.1 History

As stated previously, metal and organometallic complexes offer the properties necessary to be applicable as chemotherapeutics and photosensitizers for use in PDT and as PACT agents. One metal of interest is Re which was predicted by Mendeleev in 1869 and discovered in 1925 by Noddack, Tacke and Berg through the processing of 660 kg of molybdenite to obtain one gram of rhenium.<sup>52</sup> Although, this discovery was contested by the work of Masataka Ogawa who, in 1908, claimed he had discovered element 43 (Tc), calling it nipponium, but was discredited at the time. It emerged in 2004 that Ogawa had in fact isolated rhenium instead.<sup>53</sup> Re has the most diverse range of oxidation states ranging from -3 to +7. In particular  $\text{Re}^{(I)}$ , a  $d^6$  low spin transition metal ion that forms complexes with the general structure,  $fac\text{-}[\text{Re}(\text{CO})_3(\text{N,N})(\text{X})]^{+/-0}$  ( $\text{N,N} = \{\text{N,N} = 2,2'\text{-bipyridine (bpy)}, 1, 10'\text{-phenanthroline (phen)}, \text{etc.}; \text{X} = \text{halides}, \text{H}_2\text{O}, \text{pyridine derivatives}, \text{PR}_3\}$ ) offers both cytotoxic and photochemical properties desirable for chemotherapy and PDT.

The chemistry of Re is intertwined with that of Tc, which has origins tracing back to radio imaging. Tc was first isolated in 1938 by Segré and Perrier through the bombardment of a Mo target plate with deuterons, performed at the Berkely cyclotron. There are 20 known isotopes of Tc ( $^{91}\text{Tc}$ - $^{110}\text{Tc}$ ), with seven being nuclear. The isotope with medical relevance is  $^{99}\text{Tc}$ , which consists of approximately 80% of all nuclear imaging applications.<sup>54</sup> In 1998, Alberto *et al.* provided the first report of a  $^{99}\text{Tc}$ -tricarbonyl core,



$[^{99m}\text{Tc}(\text{H}_2\text{O})_3(\text{CO})_3]^+$  which spurred a number of ligand systems coordinated to the  $[\text{M}(\text{CO})_3]^+$  core.<sup>55</sup> This research has included an investigation into Re(I) tricarbonyl analogues as well as Tc. The investigation into the photophysics of Re(I) tricarbonyl complexes pre-dates 1998 with some of the first studies occurring in the 1970s.<sup>56-58</sup> Coupling both promising biological and photophysical activity, a plethora of research involving Re(I) tricarbonyl complexes have been performed over the past few decades.

### 1.3.2 Chemotherapy

The chemotherapeutic properties of Re based compounds are a growing area of investigation, but currently, there aren't any candidates in clinical trials. In fact, there have only been seven reports of the *in vivo* activity of Re compounds.<sup>59</sup> This is not to say the investigation of such complexes isn't worthwhile, but more so it is a relatively unexplored research topic that could potentially warrant promising results. For instance, a study in 2017 displayed the anticancer *in vitro* activity of a series of Re(I) complexes with the general structure, *fac*-[Re(CO)<sub>3</sub>(N,N)(H<sub>2</sub>O)](OTf) (OTf = CF<sub>3</sub>SO<sub>3</sub>).<sup>60</sup> The addition of the aqua ligand provided water solubility, an attractive prospect in chemotherapeutics. The diimine ligand itself was a variation between substituted bpy and phen ligands. The functionalization of the diimine ligands led to increased lipophilicity, another attractive prospect for drug candidates. From this study one candidate, *fac*-[Re(CO)<sub>3</sub>(2,9-dimethyl-1,10-phenanthroline)(H<sub>2</sub>O)](OTf) (Figure 1.6) was selected for further testing and was shown to display *in vivo* antitumor activity with limited side effects.<sup>59</sup> Additionally, using inductively-coupled-plasma mass spectrometry (ICP-MS), high levels of Re were detected in the mitochondria indicating this was the site of accumulation of the complex, as opposed to the cytoplasmic vacuolization which had initially been proposed.<sup>59</sup> Other *in vivo* studies

have shown the synergistic action of Re based complexes with that of cisplatin.<sup>61, 62</sup> There has also been an abundance of studies displaying the anticancer *in vitro* activity of Re based compounds.<sup>63</sup>

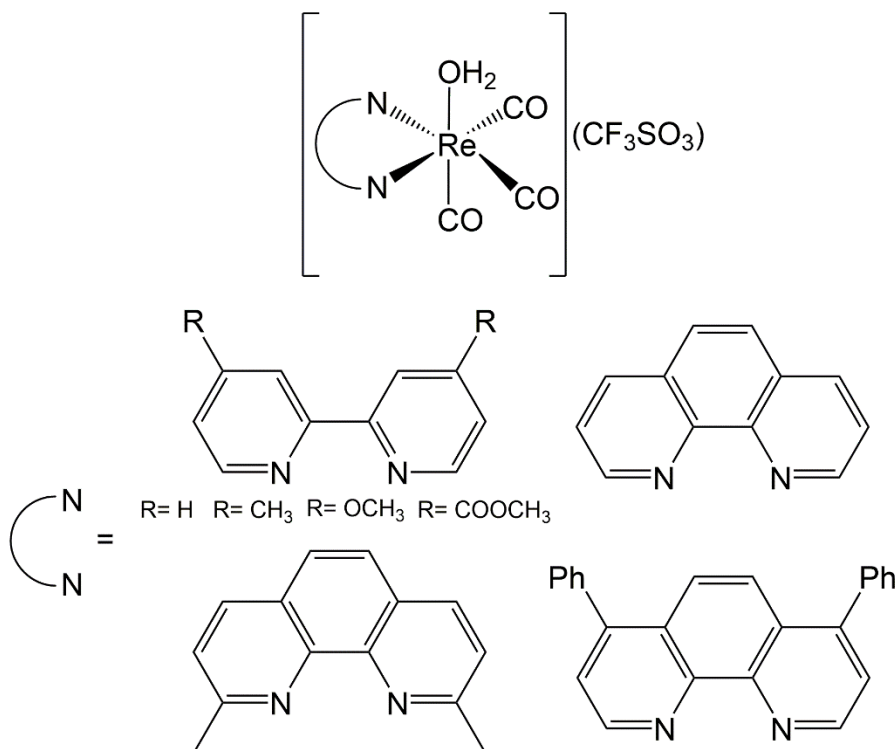


**Figure 1.6** Structure of *fac*-[Re(CO)<sub>3</sub>(N,N)(H<sub>2</sub>O)](OTf) and associated diimine ligands.<sup>60</sup>

### 1.3.3 PDT and PACT

Development of phototoxic Re based complexes is a relatively unexplored area, even less so than potential chemotherapeutics. One of the first instances of this was the research by Kastl et al., who were able to introduce a novel class of photosensitisers that differed from the more commonly used porphyrin, prophyenes and phthalocyanines scaffolds. This involved the synthesis of Re(I) tricarbonyl complexes based on the metallo-pyridocarbazole scaffold which displayed visible-light-induced anti-proliferative activity.

There are a handful of studies investigating the phototoxic properties of such complexes.<sup>64</sup>

65

In addition to producing photosensitizers for use in PDT, the investigation of photoCORMs and Re has also been a topic of investigation. Ford *et al.* investigated a series of Re complexes with the general structure, *fac*-[Re(CO)<sub>3</sub>(N,N)(PR<sub>3</sub>)] (N,N= diimine; PR<sub>3</sub> = 1,3,5-triaza-7-phosphaadamantane, tris-(hydroxymethyl)phosphine, and 1,4-diacetyl-1,3,7-triaza-5-phosphabicyclo[3.3.1]nonane) (Figure 1.7).<sup>66</sup> Upon irradiation of these complexes with UV-A light, the authors assessed their CO releasing and <sup>1</sup>O<sub>2</sub> generation properties. All complexes displayed little cytotoxicity in the dark, but upon irradiation, with 365 nm light, the phototoxic products were produced, thus initiating cell death.

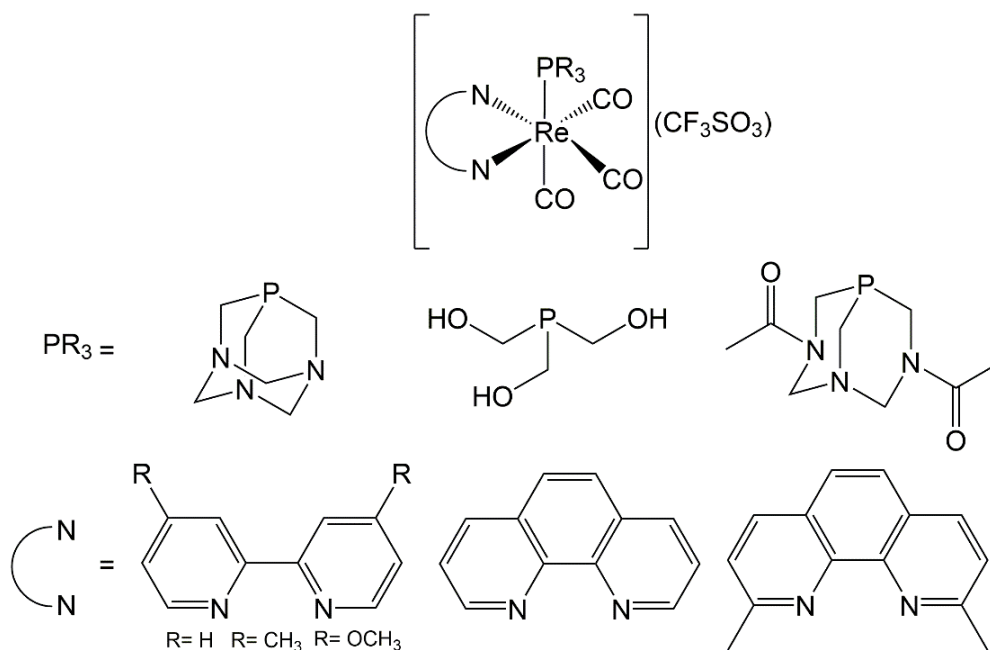


**Figure 1.7** Re(I) compounds with the general structure, *fac*-[Re(CO)<sub>3</sub>(N,N)(PR<sub>3</sub>)(CF<sub>3</sub>SO<sub>3</sub>)].<sup>67</sup>

## 1.4 Scope of thesis

The purpose of this study will be to further investigate a previously reported complex, *fac*-[Re(CO)<sub>3</sub>(bpy)(H<sub>2</sub>O)](CF<sub>3</sub>SO<sub>3</sub>) (**1**) that has shown to have *in vitro* anticancer activity. This study will look at the interactions of **1** with *L*-cysteine, N-acetyl-*L*-cysteine and STS, and the photophysical and cytotoxic properties of the products formed.

Chapter 2 and 3 have been produced in manuscript format. Their corresponding information can be found in the Appendix at the end of the thesis. References to figures in the Appenidix will be reffered to as A2 or A3 (A2.1, A3.1).

### 1.4.1 Single-Crystal X-ray diffraction

The characterization of products were performed using NMR and IR spectroscopic techniques as well as electrospray ionization mass spectrometry (ESI-MS), elemental analysis, and single-crystal X-ray diffraction. Single-crystal X-ray diffraction was also employed, which provides the 3-D structure. The technique gives a wealth of information such as the crystal system, space group, atom locations, bond lengths, and bond angles, as well as the chemical composition within the unit cell. A monochromatic X-ray beam is generated using an X-ray tube. The beam then is reflected by a single crystal which upon interaction, scatters the X-ray to produce a unique scattering pattern (Figure 1.8). X-ray diffraction is a result of a phenomenon known as coherent interference as X-rays can be thought of as waves. The diffracted X-rays form diffraction spots, which are made up of contributions from the atoms present in the crystal. The diffraction spots are collected using a two-dimensional detector which allows for the acquisition of large numbers of diffraction spots and significantly reduces the time taken to analyze a crystal.

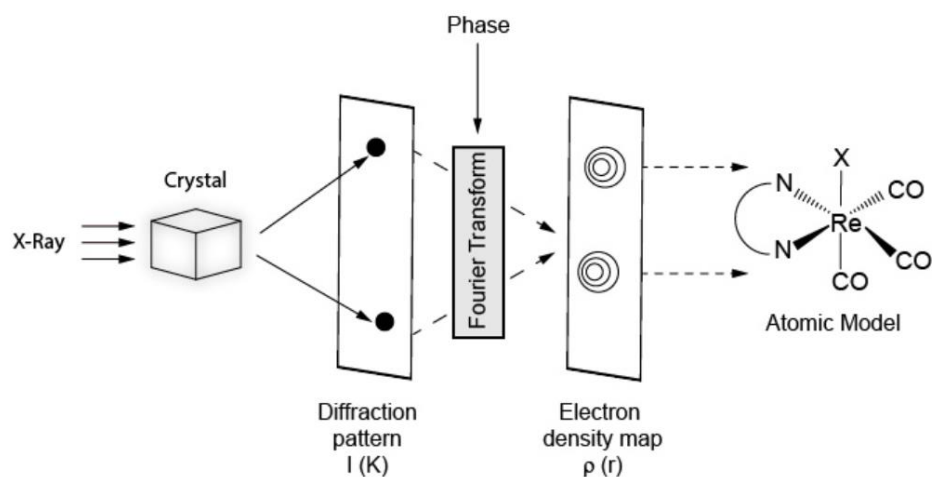


**Figure 1.8** Schematic displaying the experimental set up used for single-crystal X-ray diffraction.<sup>68</sup>

To interpret the results there are three basic equations which are derived from three fundamental facts of the principles of X-ray crystallography. The three fundamental facts are:

- i) Inside of the crystal electron density has a periodicity, i.e. the infinite repetition in three directions
- ii) Each crystal consists of atoms and the electron density in different crystals remain similar.
- iii) Electron density of the crystal causes the scattering of X-rays and the summation of the scattering wave of each electron is the scattering amplitude which when squared is proportional to the scattering intensity

Based on these facts, equations are derived enabling the analysis of collected data and production a molecular model.

#### *1.4.2 Photophysics*

UV-visible absorbance and fluorescence spectroscopy were performed to provide an insight into the photophysical characteristics of the products. As mentioned previously in relation to PDT, the use of “light” is a key component of this study. When discussing light, it is in reference to electromagnetic radiation in the UV, visible and near-infrared range. The nature of light can be described using two models: the wave model and the quantum model. Electronic absorption spectroscopy involves passing light through a sample, in a cuvette and measuring the intensity of light that is able to pass through the sample at each wavelength. Using the Beer-Lambert law the measured absorbance can be converted into a constant known as the molar extinction coefficient ( $\epsilon$ ). The spectrum itself provides information about the various electronic transitions that are occurring (Figure 1.9).

Classification and explanation of the transitions are as follows,

- i) Metal-centered (MC)
- ii) Ligand-centred (LC)
- iii) Charge-transfer (CT)

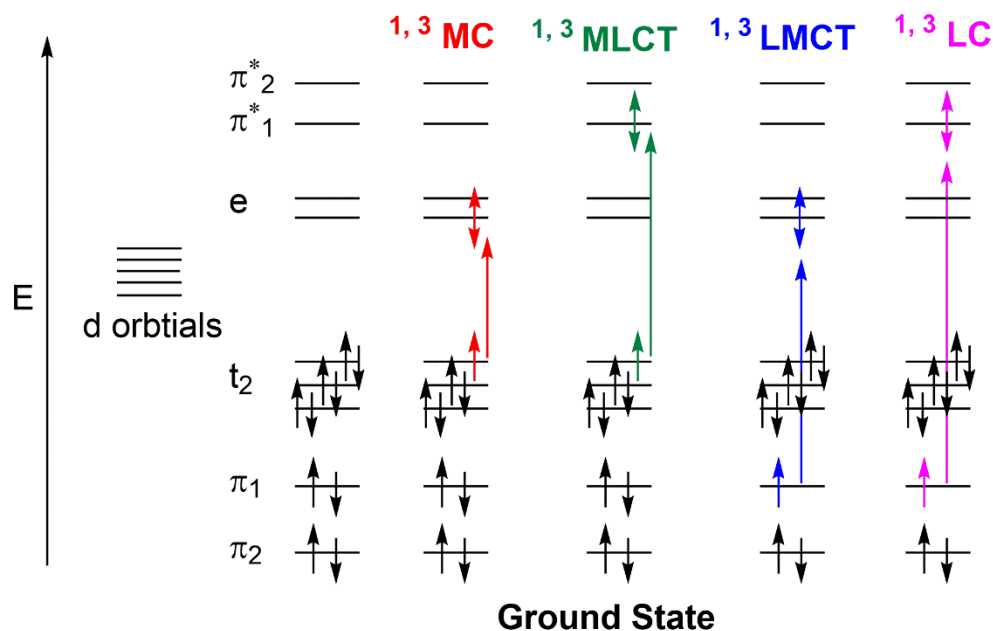


**Figure 1.9** Simplified orbital/excited-state diagram of an octahedral  $d^6$  metal complex where strong crystal field is assumed.  $\uparrow\downarrow$  = electron with associated spin.  $\uparrow$  = electron involved in electronic transition.<sup>34</sup>

MC (d-d) transitions are Laporte forbidden as well as being spin forbidden if there is a change in spin state. They have weak absorption bands that can be masked by formally allowed CT transitions. LC (interligand (IL) transitions) are often observed in large delocalised system and involve only ligand-centred orbitals. CT transitions {metal-to-ligand (MLCT), ligand-to-metal (LMCT)} are typically more intense transitions that can lead to the generation of radicals, which under biological conditions are a well-known mechanism of causing oxidative damage to cellular organelles. The presence and position of the MLCT band is particularly important for PDT and PACT applications as this will dictate the wavelength of excitation light that activates the photoreaction. For instance, the irradiation of the LMCT band of  $\text{Co}^{\text{III}}$  induces photoreduction giving rise to  $\text{Co}^{\text{II}}$ , whereas the irradiation of the MC band cause photosubstitution/aquation.<sup>69</sup>

This information can be supplemented through the use of fluorescence spectroscopy. Similar to absorbance, fluorescence spectroscopy uses a light source but in this case, it is of a specific wavelength to excite a molecule in solution which corresponds to its wavelength of maximum absorption ( $\lambda_{\text{max}}$ ). When entering a singlet excited state (Figure 1.3), a PS undergoes fluorescence, i.e the emission of a photon upon relaxation from singlet excited state to ground state. This is what is measured along with an absorption excitation spectrum in fluorescence spectroscopy. An absorption excitation spectrum provides information about the different vibrational levels that a molecule undergoes upon excitation before reaching its lowest vibrational state. From the fluorescence emission, lifetime and fluorescence quantum yield can be determined.

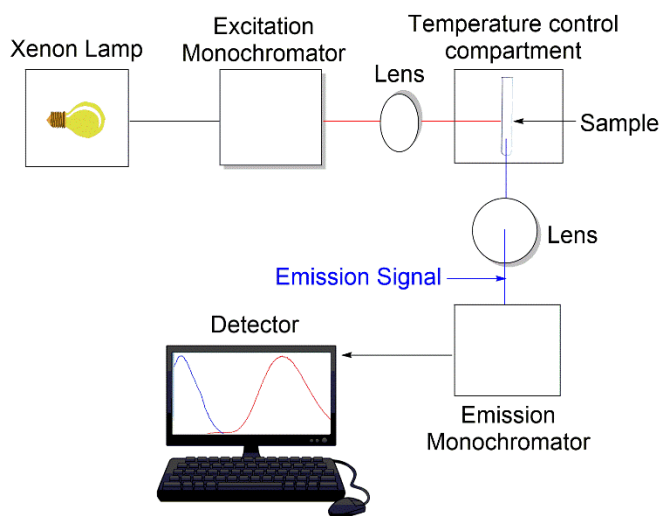


**Figure 1.10** General schematic of fluorescence spectroscopy apparatus.<sup>70</sup>

Other than undergoing fluorescence, a singlet excited state molecule can undergo ISC entering a triplet state to interact with  $^3\text{O}_2$  to produce  $^1\text{O}_2$ . The method chosen to determine the production of  $^1\text{O}_2$  for this study was direct detection (Figure 1.11). This works via the excitation of a sample using a laser as the excitation source which provides



light of a specific wavelength. The choice of wavelength is typically based upon the absorption profile of the sample being measured. The sample is irradiated using a diode-pumped laser which delivers pulses of a few nanosecond pulse-width, energy in the microjoule region and a working repetition rate of 1-100 kHz.<sup>71</sup> A thermoelectric-cooled photomultiplier detector then measures the phosphorescence emission of  $^1\text{O}_2$  in the near-infrared region at 1275 nm. To isolate  $^1\text{O}_2$  phosphorescence from the fluorescence and phosphorescence of the PS, lenses and filters are used to isolate emitted photons and block scattered excitation light. Comparing this recorded data of an unknown sample to that of a reference compound, which in the context of this study was  $[\text{Ru}(\text{bpy})_3]^{2+}$ , the  $^1\text{O}_2$  quantum yield ( $\Phi_\Delta$ ) can be determined. This is a quantitative measure of the efficiency in which a PS can use light energy to convert  $^3\text{O}_2$  to  $^1\text{O}_2$ .

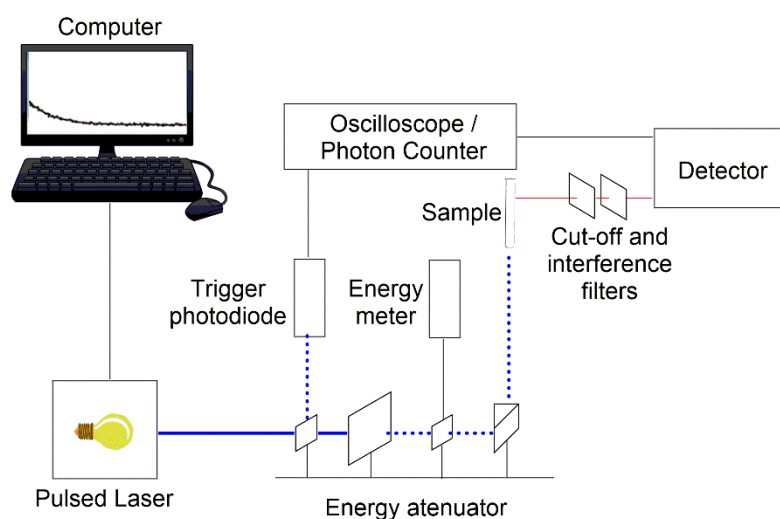


**Figure 1.11** General schematic of singlet oxygen direct detection apparatus.<sup>72</sup>

This technique is favourable compared to indirect techniques such as the *N*, *N*-dimethyl-4-nitrosoaniline (RNO)/imidazole assay.<sup>73</sup> Upon irradiation, the PS produces  $^1\text{O}_2$  which forms an intermediate with imidazole that causes the photobleaching of RNO and

reduces its absorbance. This process can be monitored using UV-visible absorbance spectroscopy and  $^1\text{O}_2 \Phi_{\Delta}$  can also be determined using a reference compound such as phenalenone.<sup>73</sup> The drawbacks with such a technique in this study would be the coordinating nature of imidazole and that it would most likely replace the axially attached ligands, thus giving an inaccurate measure of  $^1\text{O}_2$  generation.

Another product needed to be measured is the release of CO. This can be performed in a number of ways, but the methods chosen for this study are UV-visible absorbance spectroscopy and gas chromatography with a thermal conductivity detector (GC-TCD). When considering the mechanism in which CO is released (Scheme 1.1), there is the production of a new species. Upon sample irradiation, a change in the UV-vis spectrum and isosbestic points would indicate the formation of a new species and release of CO. The CO release could further be confirmed performing the same irradiation in a Schlenk cuvette under an inert atmosphere and removing gas samples using a gas-tight syringe, monitored using GC-TCD (Figure 1.12). The combination of these methods has been previously reported.<sup>67</sup> Using a reference complex, *fac*-[Re(CO)<sub>3</sub>(bpy)(P(CH<sub>2</sub>OH)<sub>3</sub>)(OTf)] the same procedure was repeated to ascertain the suitability of the equipment being used for the present study.<sup>67</sup> When comparing the spectra seen in Figure 1.13, the presence of isosbestic points indicate that upon irradiation of the complex CO is released. When performing the same irradiation experiment while measuring with GC-TCD, comparable amounts of CO release were observed further indicating the suitability of the irradiation apparatus being used for the present study.

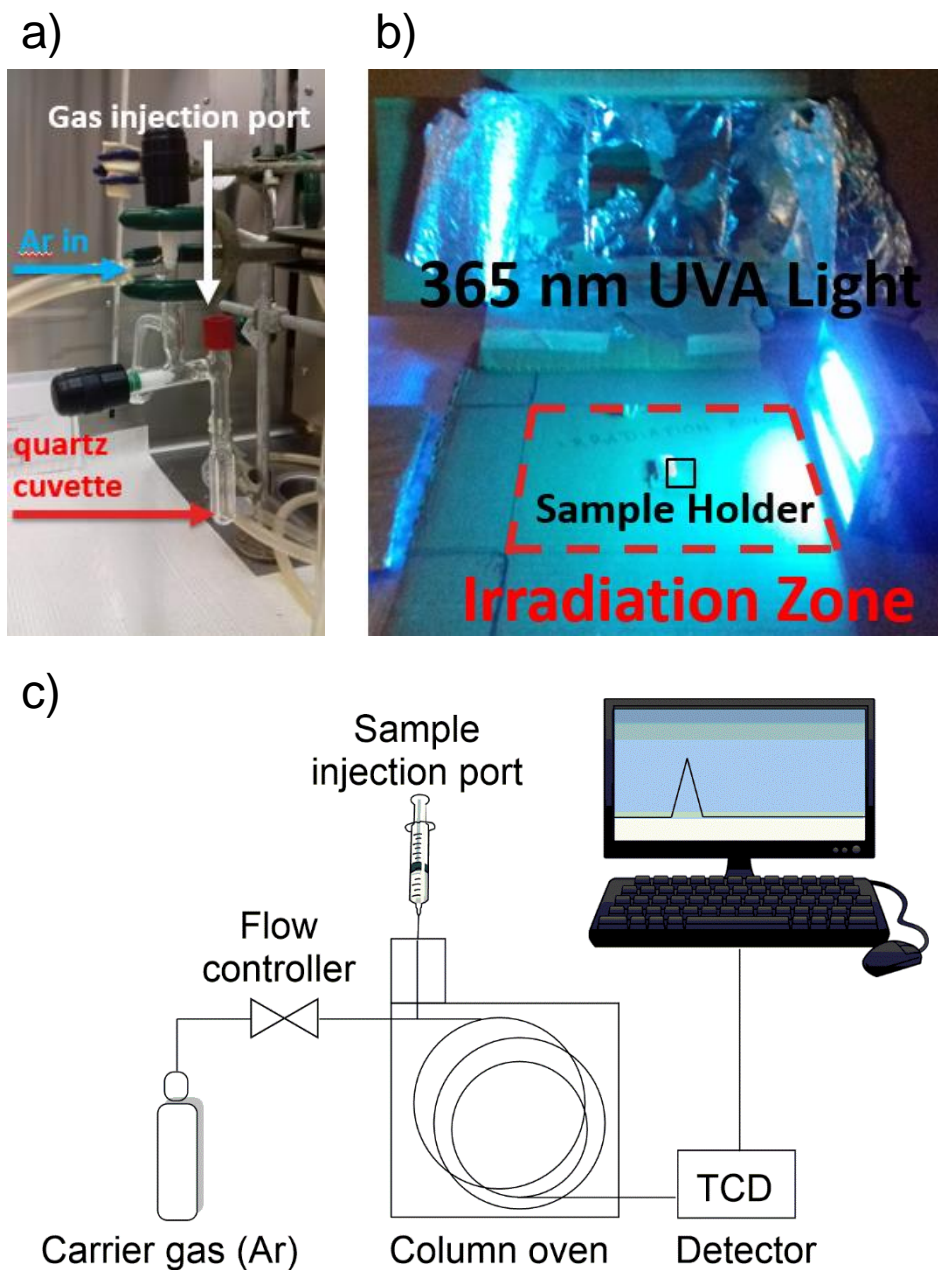


**Figure 1.12** a) Schlenk cuvette made based on Ref 67. b) Irradiation apparatus equipped with 365 nm UV-A light ( $7.105 \text{ mW/cm}^2$ ) placed at 7.2 cm from the sample position. c) General schematic of gas chromatography with a thermal conductivity detector (GC-TCD).<sup>74</sup>

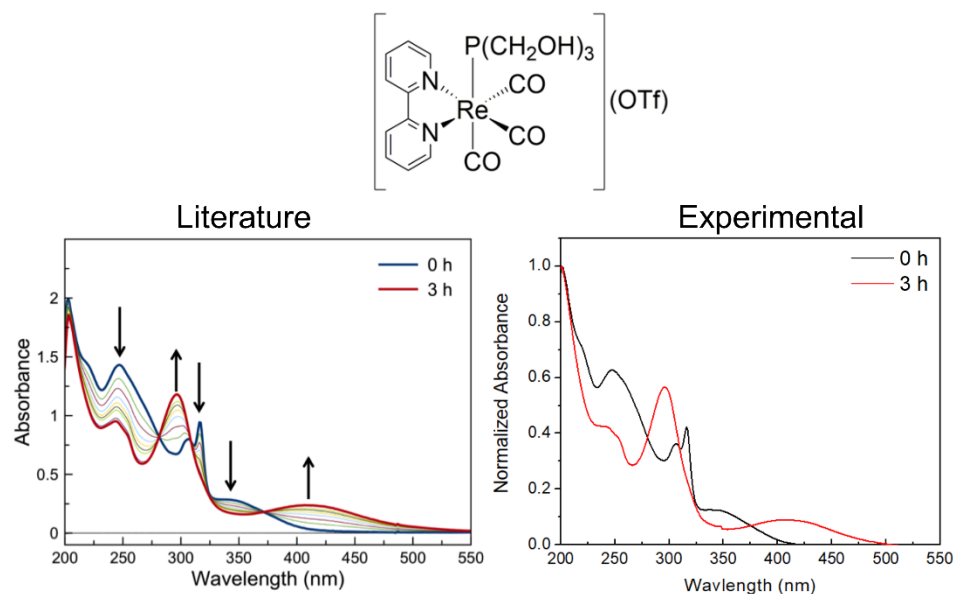


**Figure 1.13** Comparison between literature<sup>67</sup> and experimental UV-visible absorbance spectra obtained in the present study for  $fac-[Re(CO)_3(bpy)(P(CH_2OH)_3)(OTf)]$  when irradiated with 365 nm light.

### 1.4.3 Cytotoxicity and cellular localization

Cytotoxicity was assessed using the alamarBlue cell viability assay. This is a relatively simple test where a 10% solution of alamarBlue is added to the cell medium, in a 96-well plate of which the fluorescence is then measured. One component of alamarBlue is resazurin, a weakly fluorescent organic molecule (Figure 1.14). When in living cells, it is reduced to resorufin by the oxidation of NADH to NAD<sup>+</sup>. This resorufin is pink and highly fluorescent and indicates the presence of living cells.<sup>75</sup>

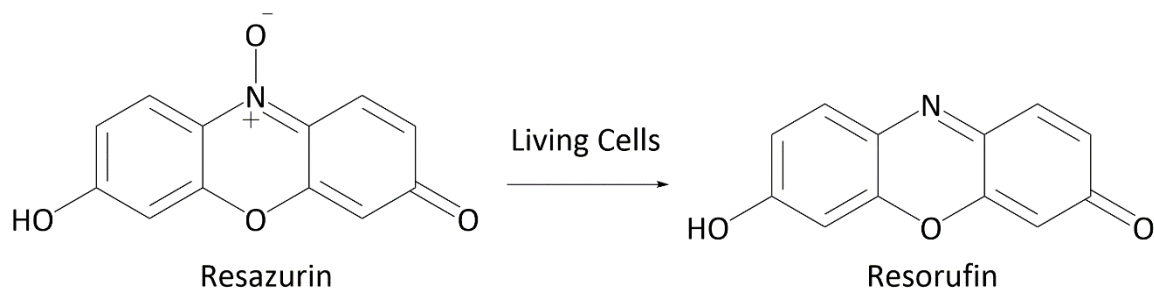


**Figure 1.14** Reduction of Resazurin in the presence of living cells to form Resorufin.<sup>75</sup>

To ascertain how the complexes behave in a cellular environment, synchrotron-based X-ray fluorescence microscopy (XFM) was used. Synchrotron radiation is produced via the acceleration of charged particles (electrons) in a circular path. With the use of bending magnets and/or special insertion magnets known as wigglers and undulators, radiation is emitted tangent to the trajectory of accelerated electrons.<sup>76</sup> In the case of XFM, an undulator is generally used. A micro-focused beam is produced and directed towards the sample, using various optical components such as mirrors, a monochromator, two Fresnel zone plates and an order sorting aperture (Figure 1.15). The incident energy is tuned above the threshold energy ( $E_0$ ) of the elements of interest in the sample. The data is collected in fluorescence mode, as the elemental concentrations are typically lower than  $100 \mu\text{g g}^{-1}$ , meaning weak X-ray absorptions would occur if measured in transmission mode. In fluorescence mode, the position of the sample is at  $75^\circ$  to the incident beam. The sample is placed in a He filled chamber to prevent attenuation of X-ray fluorescence by air. This will

also increase the fluorescence signal that reaches the detector. An energy resolving solid-state multi-detector is placed at  $90^\circ$  to the incoming beam.<sup>77</sup>

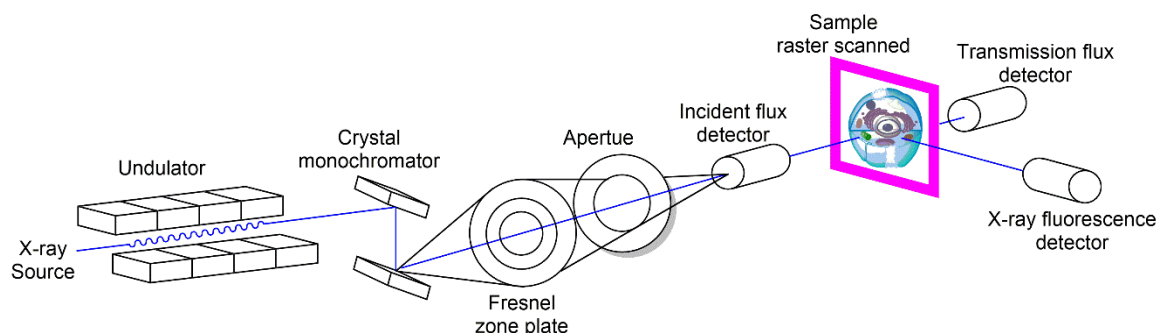


**Figure 1.15** Schematic of a synchrotron-based X-ray fluorescence microscopy experiment.<sup>78</sup>

Once the X-ray beam with high enough energy (in this study, 12.8 keV) hits the sample, the core electrons of the elements of interest are ejected. Each core electron has a specific binding energy which creates an absorption edge (e.g. K, L, M edge) when becoming excited. The K edge corresponds to the 1s core electrons, L-edges correspond to the 2s and 2p electrons, and M-edges to the 3s, 3p and 3d electrons. Following the ejection of a core electron, the element undergoes radiative relaxation and outer shell electrons fill the vacancy (core hole), thus producing a characteristic X-ray fluorescent photon, the energy of which its energy is equal to the difference between the two electronic level binding energies. In the case of Re, when excited by 12.8 keV radiation, it emits two X-ray emission lines at 8,652.5 and 8586.2 eV which are denoted  $L_{\alpha 1}$  and  $L_{\alpha 2}$ . It also produces photons with 10010.0 eV energy, which corresponds to its  $L_{\beta 1}$  emission line. If the XFM images were fitted according to the  $L_{\alpha 1}$  and  $L_{\alpha 2}$  energies there would be an overlap with the Zn  $K_{\alpha}$  (8,638.9 eV) fluorescence line which would produce incorrect images. Instead, the images can be obtained by monitoring and fitting to its  $L_{\beta 1}$  emission line (10,010.0 eV).

Since binding energies of core electrons are different for every element, and emission lines are characteristic for each element, XFM is element specific.<sup>79</sup> This is advantageous as samples can be analyzed without alteration such as the attachment of fluorophores which may have an affect on their natural elemental distribution.<sup>80</sup>

In the next two chapters, cytotoxicity, cellular uptake and photophysical properties of *fac*-[Re(CO)<sub>3</sub>(bpy)X]<sup>+0/-</sup> complexes (X= H<sub>2</sub>O, HCys<sup>-</sup>, NAC<sup>2-</sup>, S<sub>2</sub>O<sub>3</sub><sup>2-</sup>; bpy=2,2'-bipyridine) will be discussed.

## Chapter 2: Cytotoxic and photophysical properties of Re(I) tricarbonyl complex coordinated *L*-cysteine and its derivative

### 2.1 Abstract

The investigation into  $fac-[Re(CO)_3(N,N)X]^{0/+}$  (N-N = a bidentate diimine such as 2,2'-bipyridine (bpy) and 1,10'-phenanthroline (phen); X = halides, H<sub>2</sub>O, pyridine derivatives, PR<sub>3</sub>, etc.) complexes have gained interest due to their chemotherapeutic and photochemical properties. The aqua complex  $fac-[Re(CO)_3(bpy)(H_2O)](CF_3SO_3)$  (**1**) with potential anticancer activity is a member of such family of compounds. We have investigated reactions of **1** with the amino acid *L*-cysteine (H<sub>2</sub>Cys), and its derivative N-acetyl-*L*-cysteine (H<sub>2</sub>NAC) under physiological conditions (pH 7.4, 37 °C), and the impact of such coordination on the photophysical properties and cytotoxicity of **1**, as a model for its interaction with thiol-containing proteins and peptides. We report the syntheses and characterization of  $fac-[Re(CO)_3(bpy)(HCys)] \bullet 0.5H_2O$  (**2**) and  $Na(fac-[Re(CO)_3(bpy)(NAC)])$  (**3**) using spectroscopic methods (<sup>1</sup>H-, <sup>13</sup>C-NMR, IR) and electrospray ionization spectrometry (ESI-MS), as well as the crystal structure of  $\{fac-[Re(CO)_3(bpy)(HCys)]\} \cdot 4 \cdot 9H_2O$  (**2** + 1.75 H<sub>2</sub>O). The emission spectrum of **1** displays a variance in Stokes shift upon coordination of cysteine and H<sub>2</sub>NAC. Irradiating methanol solutions of **1** - **3** with  $\lambda = 355$  nm excitation laser and measuring their ability to produce <sup>1</sup>O<sub>2</sub> using direct detection methods. The cytotoxicity of **1** and its cysteine-bound complex **2** were assessed against the MDA-MB-231 breast cancer cell line, showing that the replacement of the aqua ligand on **1** with *L*-cysteine significantly reduced the cytotoxicity of the Re(I) tricarbonyl complex. Probing the cellular uptake of **1** and **2** using synchrotron-



based X-ray fluorescence microscopy (XFM) revealed an accumulation of **1** in the nuclear region, whereas the uptake of **2** was hindered, explaining its reduced cytotoxicity.

## 2.2 Introduction

Despite the great success of platinum-based chemotherapeutics, drugs with a different mode of action other than the platinum antineoplastic family are highly desirable due to their unwanted toxic side effects and prevalence of platinum resistance mechanisms.<sup>81</sup> Treatment of cancer using Photodynamic Therapy (PDT) and Photoactivated Chemotherapy (PACT) is a burgeoning area of research due to its multimodal approach.<sup>82</sup> PDT uses a combination of a nontoxic photosensitizer (PS), light and oxygen to generate cytotoxic products inducing localized cell death. PDT initiates cell death through different mechanisms which involve the generation of reactive oxygen species (ROS) such as singlet oxygen ( $^1\text{O}_2$ ) that disrupts the delicate cellular redox balance, damaging cellular vasculature, leading to tumour infarction and eliciting an immune response against the tumour cells.<sup>32, 33, 83</sup>

PACT offers an oxygen-independent alternative to PDT that is particularly useful when considering the characteristically hypoxic environment in cancer cells.<sup>84</sup> Photoactivation can induce ligand substitution reactions in PACT agents, leading to the release of a small cytotoxic molecule such as CO or NO.<sup>34</sup> The antiproliferative effect of CO is thought to be caused by its binding to cytochrome *c* oxidase, which inhibits mitochondrial pathway thus metabolically exhausting the cancer cell.<sup>85, 86</sup> A dual-action approach can help circumvent unwanted side effects, such as toxicity and resistance, associated with some of the currently used chemotherapeutics such as cisplatin.<sup>81</sup>

Transition metal complexes are particularly interesting candidates for potential PDT and PACT agents. They offer benefits such as DNA intercalating properties and a diverse range of excited states that enhance photochemical properties.<sup>10, 34</sup> In particular, the investigation of rhenium(I) tricarbonyl polypyridine complexes *fac*-[Re(CO)<sub>3</sub>(N,N)X]<sup>0/+</sup> as potential anticancer therapeutics, as well as both PACT and PDT agents has attracted a great deal of interest.<sup>63</sup>

The investigation on the photoinduced cytotoxic products of diimine rhenium(I) tricarbonyl complexes is a relatively new area of research that has expanded in the last decade.<sup>63</sup> Ford *et al.* demonstrated that irradiation of *fac*-[Re(bpy)(CO)<sub>3</sub>(P(CH<sub>2</sub>OH)<sub>3</sub>)](CF<sub>3</sub>SO<sub>3</sub>) (bpy = 2,2'-bipyridine) in the near-UV region initiated the photo-release of axially coordinated CO.<sup>66</sup> The intracellular location of the complex could also be monitored due to its emissive properties, which was detectable using confocal microscopy. Kastl *et al.* introduced a novel class of photosensitizers that differed from the more commonly used organic compounds that have consisted of porphyrins, porphycenes and phthalocyanines.<sup>87</sup> This involved the synthesis of rhenium(I) tricarbonyl complexes based on the metallo-pyridocarbazole scaffold, which displayed visible-light-induced ( $\lambda \geq 505$  nm) anti-proliferative activity.<sup>88</sup> Leonidova *et al.* introduced two *N,N*-bis(quinolinoyl) Re(I) tricarbonyl complex derivatives as excellent <sup>1</sup>O<sub>2</sub> generators in a lipophilic environment. They also showed significant enhancement in the cytotoxicity of these complexes and their bioconjugates with receptor targeting peptides upon irradiation ( $\lambda = 350$  nm).<sup>89</sup>

Zobi *et al.* found that 7-methylguanine (7-MeG) and 9-methylguanine (9-MeG) can form [Re(CO)<sub>3</sub>(guanine)L]<sup>0/+</sup> complexes (L = H<sub>2</sub>O, Br) with two different conformations:

head-to-head (HH) and head-to-tail (HT) around the Re centre.<sup>90</sup> Cellular targets other than DNA can include metallothioneins (MT) which are cysteine-rich proteins with high affinity for zinc and heavy metals such as Re(I) and Tc(I).<sup>91</sup> Hyper-accumulation of zinc in breast tissue is an indication of malignancy, and high level of zinc can lead to apoptosis. So the over-expression of MT, as well as Zn transporter ZnT2 in malignant breast cancer cells, is thought to be a method of protection from hyper-accumulation of Zn, preventing tumour cell death.<sup>92, 93</sup> The syntheses of a series of in-vitro anticancer diimine rhenium(I) tricarbonyl aqua complexes, *fac*-[Re(CO)<sub>3</sub>(N,N)(H<sub>2</sub>O)]<sup>+</sup>, have recently been reported.<sup>60</sup> The *fac*-[Re(CO)<sub>3</sub>(dmphen)(H<sub>2</sub>O)]<sup>+</sup> complex (dmphen = 2,9-dimethyl-1,10-phenantroline) showed high affinity for binding to 9-ethylguanine, *N*-acetylcysteine and *N*-acetylhistidine, but not for other amino acids such as methionine, glycine and serine.

Cysteine residues of proteins and peptides could be a potential target and binding site for these anticancer Re(I) aqua complexes. Here, we report the results of our investigations on the reaction products of *fac*-[Re(CO)<sub>3</sub>(bpy)(H<sub>2</sub>O)](CF<sub>3</sub>SO<sub>3</sub>) (**1**) with *L*-cysteine (H<sub>2</sub>Cys) and *N*-acetyl- cysteine (H<sub>2</sub>NAC), and discuss the impact of such binding on the cellular uptake, cytotoxicity and photophysical properties of the Re(I) complex.

## 2.3 Experimental Section

### 2.3.1 Materials

All chemicals and solvents were of reagent grade or higher. Rhenium pentacarbonyl chloride (98%), 2, 2'-bipyridine, Tris(2,2'-bipyridine)ruthenium(II) chloride hexahydrate, *L*-cysteine, *N*-acetyl-*L*-cysteine and glutathione were purchased from Sigma Aldrich and used without further purification. Degassed water was prepared by bubbling argon through boiled distilled water until cooled down to room temperature. Oxygen-free NaOH<sub>(aq)</sub> (1.0 M) was prepared by dissolving NaOH solid in degassed water. By refluxing toluene with Na metal and benzophenone under Ar, dry toluene was prepared.<sup>94</sup> The pH of solutions were measured using a calibrated Thermo Scientific Orion Star pH meter, using standard buffers.

### 2.3.2 Cell Culture

MDA-MB-231 breast cancer cells were acquired from the American Type Culture Collection (ATCC). Dulbecco's Modified Eagles Medium (DMEM) (Invitrogen/Gibco) was supplemented with heat-inactivated foetal bovine serum (10% v/v; Sigma Life Sciences), L-glutamine (2 mM, Invitrogen), Penicillin (100 units/mL), Streptomycin (100 µg/mL). Cells were cultured as monolayers using the above mentioned DMEM solution at 37°C in a 5% CO<sub>2</sub>-humidified incubator and were sub-cultured every 3–4 days.

### 2.3.3 Syntheses

#### 2.3.3.1 *fac*-[Re(CO)<sub>3</sub>(bpy)(H<sub>2</sub>O)](CF<sub>3</sub>SO<sub>3</sub>) (**1**).

The complex was prepared using a previously described method, through syntheses of *fac*-[Re(CO)<sub>3</sub>(bpy)Cl] (see Appendix).<sup>67</sup> Solutions of *fac*-[Re(CO)<sub>3</sub>(bpy)Cl] (2.69 mmol) in acetone (80 mL) and AgCF<sub>3</sub>SO<sub>3</sub> (2.69 mmol) in acetone (20 mL) were mixed. The mixture was refluxed at 70 °C for 2 h under Ar. AgCl precipitate was filtered off and the solvent was removed in vacuo. The crude yellow solid was recrystallized using acetone/H<sub>2</sub>O (1:3 v/v) mixture and left in the desiccator under vacuum for 4 days. The yellow crystals formed were vacuum filtered and washed with diethyl ether. The unit cell parameters of these crystals were the same as those previously reported.<sup>95</sup> Yield: 94%. <sup>1</sup>H NMR (600 MHz, D<sub>2</sub>O) δ 9.19 (d, J = 5.3 Hz, 2H), 8.57 (d, J = 8.1 Hz, 2H), 8.36 (t, J = 7.9 Hz, 2H), 7.78 (t, J = 7.0 Hz, 2H). <sup>13</sup>C {<sup>1</sup>H} NMR (600 MHz, D<sub>2</sub>O) δ 156.4, 154.1, 141.4, 128.1, 124.3. IR  $\tilde{\nu}_{\text{co}}$  = 2033<sub>axial</sub>, 1914<sub>eq</sub> cm<sup>-1</sup>. Anal. Cald. for (*fac*-[Re(CO)<sub>3</sub>(bpy)(H<sub>2</sub>O)](CF<sub>3</sub>SO<sub>3</sub>) (ReC<sub>14</sub>H<sub>10</sub>N<sub>2</sub>O<sub>7</sub>SF<sub>3</sub>): Found: C, 28.46; H, 1.67; N, 4.65%.

#### 2.3.3.2 *fac*-[Re(CO)<sub>3</sub>(bpy)(HCys)]•0.5H<sub>2</sub>O (**2**).

Solid *L*-cysteine (2.53 mmol) was added to a completely dissolved, yellow solution of **1** (0.253 mmol) in 20 mL of degassed water under argon atmosphere to avoid oxidation of cysteine thiol group. The pH of the solution (4.55) was adjusted to 7.40 by dropwise addition of 1.0 M degassed NaOH, then allowing the orange solution to stir for 48 h at 37 °C. The resulting precipitate was vacuum filtered and washed with water. The crude solid was further purified by dissolving it in methanol and then filtering the solution. The filtrate was then concentrated to dryness using a rotary evaporator; the orange solid was dried

under vacuum. Yield: 58%. Complex **2** is insoluble in water but soluble in methanol; it was initially stable in CD<sub>3</sub>OD although some decomposition was observed over a period of 7 days. <sup>1</sup>H NMR (600 MHz, CD<sub>3</sub>OD) δ 9.06 (dddd, J = 11.3, 5.5, 1.6, 0.8 Hz, 2H), 8.58 (dt, J = 8.2, 1.0 Hz, 2H), 8.24 – 8.19 (m, 2H), 7.66 (dddd, J = 7.8, 5.5, 2.5, 1.2 Hz, 2H), 3.27 (dd, J = 10.7, 3.7 Hz, 1H), 2.99 (dd, J = 13.3, 3.7 Hz, 1H), 2.60 (dd, J = 13.3, 10.7 Hz, 1H). <sup>13</sup>C {<sup>1</sup>H} NMR (600 MHz, CD<sub>3</sub>OD) δ 173.4 (C12), 157.07 (C1, C1'), 154.4 (C3, C3'), 140.7 (C4, C4'), 128.7 (C5, C5'), 125.3 (C6, C6'), 60.1 (C11), 32.5 (C10). Anal. Cald. for *fac*-[(CO)<sub>3</sub>Re(bpy)(HCys)]•0.5H<sub>2</sub>O (ReC<sub>16</sub>H<sub>15</sub>N<sub>3</sub>O<sub>5.5</sub>S): C, 34.59; H, 2.72 ; N, 7.56% (1.62% H<sub>2</sub>O). Found: C, 34.20; H, 2.43; N, 7.37%. TGA: 1.6 % H<sub>2</sub>O). IR:  $\tilde{\nu}_{\text{co}} = 2005_{\text{axial}}$ , 1907<sub>eq</sub>, 1877<sub>eq</sub> cm<sup>-1</sup>.

### 2.3.3.3 Na(*fac*-[Re(CO)<sub>3</sub>(bpy)(NAC)]) (**3**).

The above procedure was repeated, mixing 0.17 mmol of complex **1** and 1.68 mmol *N*-acetyl-*L*-cysteine in 20 mL of degassed water under argon, and adjusting the solution pH (2.11) to 7.40. The final product (**3**) was a dark orange solid that was not water-soluble. It displayed poor stability in a range of solvents, undergoing rapid decomposition. Yield: 54%. Anal. Cald. for Na(*fac*-[(CO)<sub>3</sub>Re(bpy)(NAC)]): (ReC<sub>18</sub>H<sub>15</sub>N<sub>3</sub>O<sub>6</sub>SNa): C, 35.41; H, 2.48; N, 6.88%. Found: C, 35.79; H, 2.54; N, 6.77%. IR:  $\tilde{\nu}_{\text{co}} = 2002_{\text{axial}}$ , 1869<sub>eq</sub> cm<sup>-1</sup>. For <sup>1</sup>H NMR measurement, a small portion of the filtrate (when separating the crude solid and solution) was passed through a Sephadex G-15 size exclusion column chromatography to separate unreacted **1** and excess *N*-acetyl-*L*-cysteine. The eluted orange solution was evaporated in dryness and then dissolved in D<sub>2</sub>O and further analyzed by <sup>1</sup>H NMR. (400 MHz, D<sub>2</sub>O) δ 9.12 (d, J = 5.5 Hz), 8.53 (d, J = 8.5 Hz), 8.25 (t, J = 8.0 Hz), 7.70 (d, J = 8.1

Hz), 3.98 (d, J = 9.2 Hz, 1H), 2.77 (d, J = 9.8 Hz, 1H), 2.64 – 2.56 (d, 1 H), 1.96 (s, J = 0.9 Hz, 3H). Slight impurities were due to uncoordinated *N*-acetyl-*L*-cysteine (Figure A2.3).

### 2.3.3 Physical Measurements and Methods

#### 2.3.3.1 Electronic spectroscopy.

UV-vis spectra were recorded using a Cary 50 spectrophotometer. Samples were measured in a quartz cuvette (1 cm path length) using water and/or methanol as a reference. The molar extinction coefficients ( $\epsilon$ ) of compounds **1** - **3** were evaluated from absorbance data using Beer-Lambert law.

#### 2.3.3.2 Fluorescence emission spectroscopy.

Fluorescence emission spectra were carried out using a Photon Technology International QuantaMaster 400 steady-state spectrofluorimeter (Horiba Scientific). Fluorescence quantum yields of **1**, **2** and **3** were determined via a relative method, as described elsewhere, using  $[\text{Ru}(\text{bpy})_3]^{2+}$  in MeOH ( $\phi = 0.31$ )<sup>96</sup> or Quinine sulfate in 0.1 N  $\text{H}_2\text{SO}_4$  ( $\phi = 0.55$ )<sup>97</sup> in a deoxygenated MeOH solution as standards. The absorbance at the excitation wavelength for Quinine sulfate and **2** at 290 nm, and for  $[\text{Ru}(\text{bpy})_3]^{2+}$ , **1** and **3** at 360 nm were kept below 0.05.

#### 2.3.3.3 Single Crystal X-Ray Diffraction

Single crystals of  $\{\text{fac-}[\text{Re}(\text{CO})_3(\text{bpy})(\text{HCys})]\}_4 \cdot 9\text{H}_2\text{O}$  (**2** + 1.75  $\text{H}_2\text{O}$ ) were grown by using the same reaction conditions as previously described (section 2.3.3.2). Instead of being continuously stirred at 37 °C, the flask was sealed under Ar and left in the fridge (T = 4°C). After 5 days orange crystals had formed. Single-crystal X-ray diffraction data were

collected at 173 K on a Bruker SMART APEX II CCD diffractometer using graphite-monochromated Cu-K $\alpha$  radiation ( $\lambda = 1.5406 \text{ \AA}$ ). The single crystal was mounted on nylon CryoLoops (Hampton Research) with Paraton-N (Hampton Research). The data integration and reduction were processed with the INTEGRATE program of the APEX3 software.<sup>98</sup> Multi-Scan absorption correction was applied to the collected reflections. Using Olex2,<sup>99</sup> the structure was solved with the ShelXT<sup>100</sup> structure solution program using Intrinsic Phasing and refined with the ShelXL<sup>101</sup> refinement package using Least Squares minimization. All non-hydrogen atoms were refined anisotropically. The water hydrogen atoms were located in difference Fourier maps and refined by using the HTAB command. The organic hydrogen atoms were generated geometrically. The refinement parameters are summarized in Table A2.3.

#### **2.3.3.4 <sup>1</sup>O<sub>2</sub> Direct Detection**

<sup>1</sup>O<sub>2</sub> 1270 nm phosphorescence kinetic traces were acquired with a time-resolved near-infrared (TRNIR) detection system in air-equilibrated methanol. A diode-pumped Nd:YAG laser (FTSS355-Q3, CryLas, Germany) working at 1 kHz repetition rate and tuned at 355 nm was used as the excitation source for [Ru(bpy)<sub>3</sub>]<sup>2+</sup>. An 1150 nm cut-on long pass filter (FEL1150, ThorLabs, Newton, NJ) and a 1064 nm notch filter (NF1064-44, ThorLabs) were mounted side by side at the entry port of a monochromator (Digikröm CM110 1/8 m, Spectral Products, Putnam, CT). A TE-cooled PMT (model H10330A-45, Hamamatsu, Japan) working at -908 V was used as the detector at the exit port of the monochromator. The PMT output was amplified to a voltage pulse using a 1.1 GHz preamplifier module (PAM-102-T, PicoQuant GmbH, Germany) connected to a multichannel scaler (TimeHarp 260-Nano, PicoQuant). The signal monitored at 1270 nm



was collected for 200 s with 256 ns resolution for each time-resolved  $^1\text{O}_2$  emission curves recorded. The time-resolved curves were chi-squared fitted to equation (1) using Prism 7.0 (GraphPad Software Inc., La Jolla, CA) with  $\tau_\Delta$ ,  $\tau_T$  and  $S_0$  as free parameters. The goodness of the fittings was assessed by the residual plots.

$$S(t) = S_0 \frac{\tau_\Delta}{(\tau_\Delta - \tau_T)} \left( \exp\left(\frac{-t}{\tau_\Delta}\right) - \exp\left(\frac{-t}{\tau_T}\right) \right) \quad (\text{eq. 1})$$

### 2.3.3.5 CO Release detection.

Possible release of CO gas upon irradiating solutions of **1** - **3** with light ( $\lambda = 365$  nm) was monitored using UV-vis spectroscopy, and gas chromatography with thermal conductivity detection (GC-TCD) using *fac*-[Re(CO)<sub>3</sub>(bpy)(P(CH<sub>2</sub>OH)<sub>3</sub>)(CF<sub>3</sub>SO<sub>3</sub>)] (See Appendix) as a standard.<sup>67</sup> Solutions of **1**, **2** and **3** (50  $\mu\text{M}$ , 5 mL) in degassed MeOH were injected in a Schlenk cuvette (internal volume of 23.6 mL) under argon. Each sample was then exposed to  $\lambda = 365$  nm light (7.105 mW/cm<sup>2</sup>) for two hours, measuring its UV-vis spectrum at 20 minutes intervals. This process was repeated with the GC-TCD method, but after each 20 minutes interval, a gastight syringe was used to remove a 100  $\mu\text{L}$  sample from the headspace of the cell (in Schlenk cuvette) through a special screw-top fitted with a three-layer laminated silicone GC septum. This sample was analyzed by a GC-TCD using an Agilent 6890N gas chromatograph fitted with a Carboxen 1010 PLOT fused silica capillary column ( $L \times \text{I.D.} = 30 \text{ m} \times 0.53 \text{ mm}$ , average thickness 30  $\mu\text{m}$ ). The GC inlet temperature was 230  $^\circ\text{C}$ . The oven was held at 35  $^\circ\text{C}$  for 14 min, then ramped at 20  $^\circ\text{C}/\text{min}$  to 245 $^\circ\text{C}$ , and finally held at 245  $^\circ\text{C}$  for 10 min. The retention time for carbon monoxide (CO) is about 11.2 min, and that for carbon dioxide (CO<sub>2</sub>) is 21 min.<sup>102</sup> Oxygen and

nitrogen from ambient air have retention times of about 8.2 and 8.4 min, respectively.<sup>102</sup>

The ChemStation auto-integration function was used to calculate the peak area for CO.

#### ***2.3.3.6 Lipophilicity and partition coefficient (log P)***

Partition coefficients (log P) were determined by the shake flask method using n-octanol and water.<sup>103</sup> Complex **1** was dissolved in water to give 50 µM solution whereas **2** was dissolved in aqueous ethanol (7.5 mL) to improve solubility and then added to water to give a 1.5% aqueous ethanol 50 µM solution. The molar extinction coefficients (ε) of these complexes at 243 nm ( $\lambda_{\text{max}}$ ) were evaluated from absorbance data using Beer-Lambert law (Figure A2.13). The aqueous solutions and n-octanol were mixed at different ratio and were shaken using a mechanical shaker for 24 h at 25 °C. The mixtures were then centrifuged at 5000 rpm for 10 min at 25 °C. UV-vis spectra were taken at room temperature of the aqueous phase of each sample. The absorption of each complex at 243 nm was then correlated to its concentration in the aqueous phase. Log P values were calculated using the following equation,

$$\log P = \log \left( \frac{\text{Concentration } n - \text{octanol phase}}{\text{Concentration water phase}} \right) \text{ (eq. 2)}$$

#### ***2.3.3.7 Cell Viability.***

The cell viability of complexes **1** and **2** as well as cisplatin were measured using the alamarBlue Cell Viability Reagent Assay (Invitrogen). 7,500 MDA-MB-231 breast cancer cells were seeded per well in black-walled 96-well plates for 48 h in a 37°C in a 5% CO<sub>2</sub>-humidified incubator. Fresh stock solutions of **1** and cisplatin were prepared in DMEM whereas for **2**, 1.5% EtOH in DMEM was used. Drug exposure times were 24 and

48 h. Supernatants were then removed using suction and each well washed with PBS before being treated with 10% v/v alamarBlue reagent and left at 37 °C in a 5% CO<sub>2</sub>-humidified incubator for 2.5 h. After incubation, fluorescence was measured on a SpectraMax M2e Multi-detection reader using the respective excitation and emission wavelengths of 565-575 nm and 585-595 nm. Using Prism GraphPad Prism Version 5.03 software, cell viability were determined as a percentage of the fluorescence of cells when treated with **1** or **2** with respect to the control (DMEM) or vehicle control (1.5% EtOH in DMEM in the case of **2**). By curve fitting-plots of cell viability (%) vs. log of drug concentration, IC<sub>50</sub> values were calculated. All data were gathered from three independent experiments using 9 biological replicates and their standard deviations were calculated.

#### ***2.3.3.8 X-ray fluorescence microscopy sample preparation***

Stock solutions (800 µM) of **1** and **2** were prepared in DMEM (solution **2** contained 1.5% EtOH for solubility purposes) and were then diluted to 20 µM with DMEM. As described elsewhere,<sup>104</sup> cells were grown on 1.5 mm x 1.5 mm x 500 nm Si<sub>3</sub>N<sub>4</sub> windows, by seeding 225,000 cells per well in 6-well plates which were then allowed to attach at 37°C in a 5% CO<sub>2</sub>-humidified incubator for 24 h. Using 20 µM solutions of **1** or **2**, or only a control, cells were treated for a period of 6 h. Upon removal of the medium, cells were washed with Dulbecco's phosphate-buffered saline (D-PBS), fixed with 4% paraformaldehyde (prepared fresh in DPBS) solution for 1 h, and then washed with PBS, ammonium acetate (in Milli-Q water) two times.<sup>105, 106</sup>

### **2.3.3.9 XFM data collection**

Details of data collection and data analysis for X-ray Fluorescence Microscopy (XFM) have been described elsewhere.<sup>104</sup> XFM images of the cells were obtained at undulator beamline 2-ID-D of the Advanced Photon Source (APS), Illinois, USA, using an incident energy of 12.8 keV using a double crystal monochromator. Using two Fresnel zone plate, the beam size was focused to 0.35  $\mu\text{m}$ ; the images were obtained with a spatial resolution of 0.5 x 0.5  $\mu\text{m}$  in step-scan mode and 1 s dwell time. Using a single element silicon drift energy dispersive detector (Vortex EX, SII Nano-technology, Northridge, CA), X-ray fluorescent spectra were collected from samples that had been in a He atmosphere set at 75° to the incident beam. Four to five individual cells per sample were selected using an optical microscope.

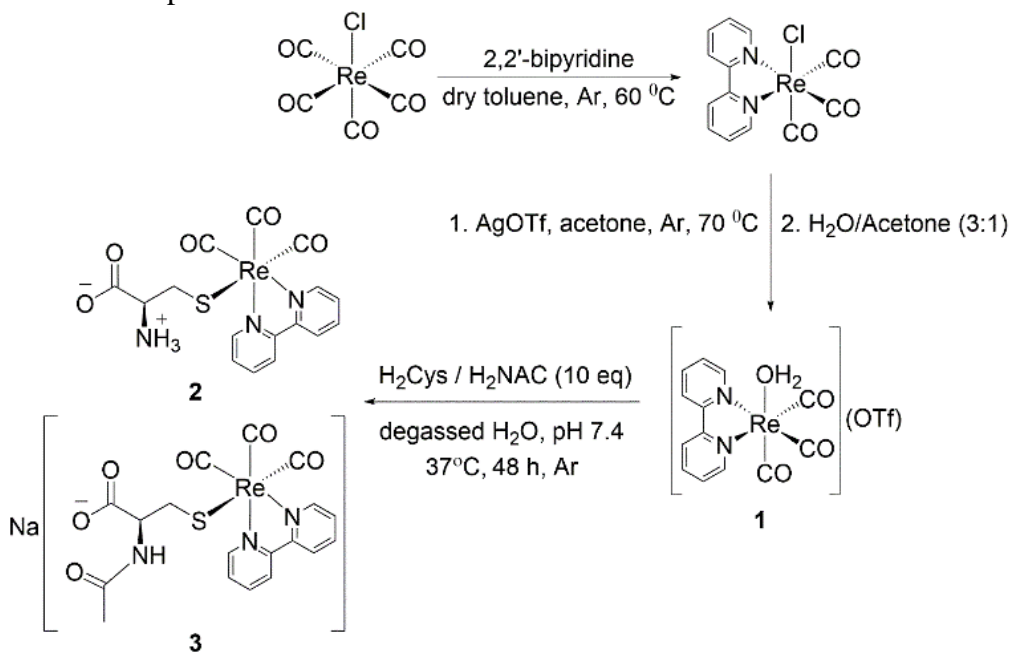
### **2.3.3.10 XFM data analysis**

By fitting the raw fluorescence emission spectra to Gaussians at each spatial point, elemental maps (in units of  $\mu\text{g cm}^{-2}$ ), as well as regions of interest (ROIs), were generated.<sup>107, 108</sup> To obtain Re images, its  $L_{\beta}$  emission line (10010.0 eV) were used for fitting, as its  $L_{\alpha}$  line (8586.2 eV) has overlap with the Zn  $K_{\alpha}$  (8638.9 eV) fluorescence line (See Figure A2.19). Comparison of X-ray fluorescence intensity to those of the thin-film standards, NBS-1832 and NBS-1833, from the National Bureau of Standards (Gaithersburg, MD) allowed for quantification. All data analysis were performed using MAPS software.<sup>108, 109</sup>

## 2.4 Results and Discussion

### 2.4.1 Characterization of Re(I)-thiolate complexes **2** and **3**

Using yellow crystals of *fac*-[Re(CO)<sub>3</sub>(bpy)(H<sub>2</sub>O)](CF<sub>3</sub>SO<sub>3</sub>) (**1**), we successfully prepared two orange/ dark-orange Re(I) tricarbonyl thiolate complexes with bound cysteinate and N-acetylcysteinate ligands under physiological conditions (pH = 7.4 and 37 °C): *fac*-[Re(CO)<sub>3</sub>(bpy)(HCys)] (**2**) and Na(*fac*-[Re(CO)<sub>3</sub>(bpy)(NAC)]) (**3**), both of which have poor water solubility. Scheme 2.1 provides an overview for the syntheses of these Re(I) thiolate compounds:



**Scheme 2.1** Synthesis of *fac*-[Re(CO)<sub>3</sub>(bpy)(H<sub>2</sub>O)](CF<sub>3</sub>SO<sub>3</sub>) (**1**) starting from Re(CO)<sub>5</sub>Cl and the subsequent reactions between **1** and *L*-cysteine or N-acetyl-*L*-cysteine.

The complexes **2** and **3** were characterized using <sup>1</sup>H-, <sup>13</sup>C-NMR and vibrational spectroscopy (IR), as well as electrospray ionization mass spectrometry (ESI-MS). The <sup>1</sup>H NMR spectra of **2** measured in CD<sub>3</sub>OD displayed clear, well-resolved peaks whereas in the same solvent, among others (CD<sub>3</sub>CN, CDCl<sub>3</sub>, CD<sub>3</sub>COCD<sub>3</sub>), **3** displayed rapid

decomposition (see Figure A2.3). The small difference between cysteine and N-acetyl cysteine, appears to have a significant effect on the stability of the Re-thiolate coordination in various solvents. Based on previous NMR data of **1** in CD<sub>3</sub>OD the *fac*-[Re(CO)<sub>3</sub>(bpy)(H<sub>2</sub>O)]<sup>+</sup> complex also undergoes a ligand exchange between H<sub>2</sub>O and CD<sub>3</sub>OD, establishing an equilibrium, as evidenced by observing two sets of bipyridine peaks in the aromatic region. The addition of D<sub>2</sub>O shifted the equilibrium to the intended product of **1**, observed through coalescence of the signals.<sup>60</sup>

In the ESI-Mass spectra of **2**, mass peaks at  $+m/z = 548.03$  and  $570.01$  amu in (+) ion mode were attributed to [Re(CO)<sub>3</sub>(bpy)(HCys) + H<sup>+</sup>]<sup>+</sup> and [Re(CO)<sub>3</sub>(bpy)(HCys) + Na<sup>+</sup>]<sup>+</sup>, respectively, with peaks at  $-m/z = 389.94$ ,  $546.01$  and  $581.99$  amu in (-) ion mode assigned to respective ions: [Re(CO)<sub>3</sub>(Cys)]<sup>-</sup>, [Re(CO)<sub>3</sub>(bpy)(Cys)]<sup>-</sup> and [Re(CO)<sub>3</sub>(bpy)(HCys) + Cl]<sup>-</sup> (see Figures A2.6-A2.7, and Tables A2.1-A2.2). For complex **3**, a small peak was detected at  $+m/z = 590.04$  amu for [Re(CO)<sub>3</sub>(bpy)(NAC) + 2H<sup>+</sup>]<sup>+</sup> ion, while mass peaks for [Re(CO)<sub>3</sub>(NAC)]<sup>-</sup> and [Re(CO)<sub>3</sub>(bpy)(NAC)]<sup>-</sup> ions were observed at  $-m/z = 431.95$  and  $588.02$  amu (see Figures A2.6-A2.7, and Tables A2.1-A2.2). Characteristic CO bond stretching vibrational frequencies were observed in the IR spectra of complexes **1**, **2** and **3** at 2033, 2005, 2002 cm<sup>-1</sup> respectively which corresponds to the totally symmetric in-phase ν(CO) vibration, denoted as A'(1) (Figure A2.4).<sup>110</sup> The shift of the C≡O stretching vibration to lower frequencies for **2** and **3** could be attributed to the increased electron density on Re(I) from the coordinated thiolate groups, which is then back-donated to the π\* orbital of carbonyl ligands, making the C≡O bond weaker. Additional vibrations are at 1913 cm<sup>-1</sup> in **1**, 1907 and 1877 cm<sup>-1</sup> in **2**, and 1869 cm<sup>-1</sup> in **3**

which correspond to the out-of-phase totally symmetric  $A'(2)$  vibration and the asymmetric vibration of the equatorial CO ligands denoted  $A''$  (Figure A2.4).<sup>110</sup>

#### 2.4.2 Single Crystal X-ray Diffraction

Single crystals of  $\{fac-[Re(CO)_3(bpy)(HCys)]\}_4 \cdot 9H_2O$  (**2** + 1.75  $H_2O$ ) were obtained by mixing the reactant in water, adjusting the pH to 7.40 and then leaving the reaction mixture in the fridge (see the Experimental section). After 5 days small orange crystals had formed which were suitable for crystallography (see Figure 2.1).

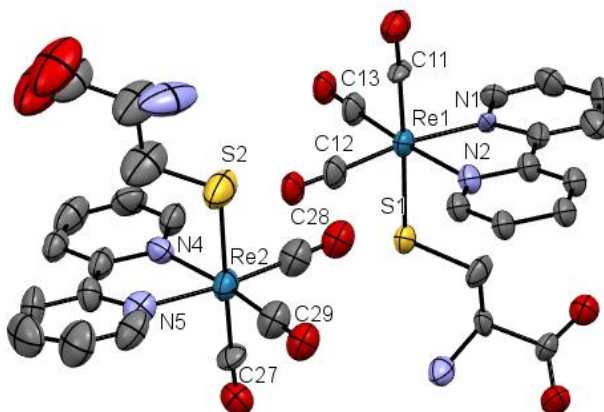


**Figure 2.1** Crystal Structure of  $\{fac-[Re(CO)_3(bpy)(HCys)]\}_4 \cdot 9H_2O$  (**2** + 1.75  $H_2O$ ). Ellipsoids are drawn at the 50% probability level.  $H_2O$  solvent molecules and H atoms have been omitted for clarity.

Interatomic distances and bond angles have been reported in Supporting Information (Tables A2.4). The Re-S bond distances of 2.503(7) and 2.496 (10) Å in the two  $fac-[Re(CO)_3(bpy)(HCys)]$  entities are similar to the reported Re-S bond length for a  $Re(CO)_3(bpy)^+$  complex bound to a pyridine-2-thiolate ligand (Re-S 2.4945(13) Å).<sup>111</sup> However, in the latter the Re-C<sub>(axial)</sub> bond 1.931(3) Å appears to be somewhat longer than

the corresponding distance in the Re(I) cysteinate complex (1.879(24) Å and 1.909 (20) Å). It is noteworthy that the reported Re-C<sub>(axial)</sub> distance in the Re(I)-aqua complex **1** is 1.882(10) Å.<sup>112</sup>

### 2.4.3 Photophysical Properties

Further characterization was done by measuring the UV-vis absorption, excitation and emission spectra of the three complexes (**1-3**) in MeOH. Fluorescence quantum yield ( $\Phi_{\text{em}}$ ) and lifetime were also measured. Absorbance data of **1** has been previously reported in DMF showing the respective absorbance and emission maxima at  $\lambda_{\text{max}}$ =350 nm and  $\lambda_{\text{em}}$ =540 nm.<sup>113</sup>

**Table 2.1** Photophysical properties of complexes **1-3** in MeOH\*

Complex	$\lambda_{\text{max}}$ (nm) $\epsilon$ (M <sup>-1</sup> cm <sup>-1</sup> )	$\lambda_{\text{em}}$ (nm)	$\Phi_{\text{F}}$
<b>1</b>	243 (18,000), 293 (13,200), 303 (13,000), 317 (9,350), 358 (3,250)	587	0.037
<b>2</b>	243 (18,900), 291 (12,500), 370 (2,260), 475 (500)	458	0.001
<b>3</b>	244 (20,000), 290 (14,100), 360 (3,300), 484 (550)	608	0.007

\* see Figures A2.8, A2.9 and A2.10

The absorbance spectra of **1**, **2** and **3** display two intense bands (Figure 2.2, Table 2.1) centred at 243 and 291-293 nm which correspond to the respective spin allowed intra-ligand, <sup>1</sup>IL transitions,  $\pi \rightarrow \pi^*$  and  $n \rightarrow \pi^*$ .<sup>114</sup> The changes in axial ligand appears to have no effect on the  $n \rightarrow \pi^*$  transition whereas the  $\pi \rightarrow \pi^*$  appears to be more sensitive with the peak being blue-shifted from **1**  $\rightarrow$  **3**. The substitution of the aqua ligand with HCys<sup>-</sup>



and NAC<sup>2-</sup> appears to result in a bathochromic shift in the <sup>1</sup>MLCT (singlet metal-to-ligand charge-transfer) bands in UV-vis spectra of **2** and **3**. These lower energy <sup>1</sup>MLCT bands, in **1**, **2** and **3** at 358, 475 and 484 nm respectively occur as a result of Re(dπ) → bpy(π\*) transitions.<sup>114</sup>

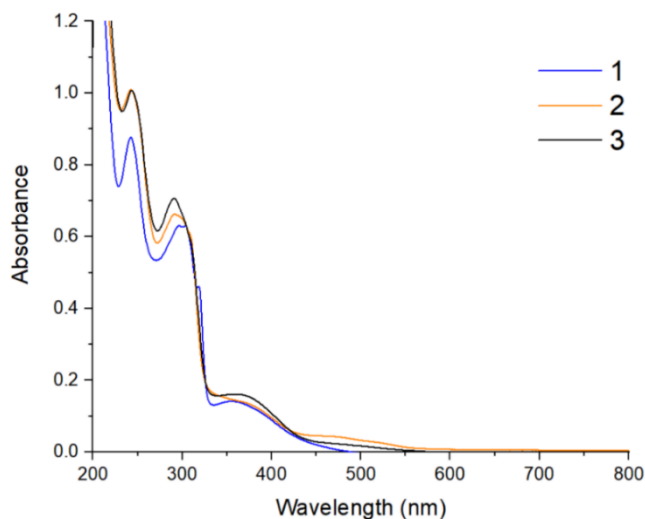


**Figure 2.2** UV-vis absorbance spectra of 50 μM MeOH solutions of **1** (blue), **2** (orange) and **3** (black).

Emission and excitation spectra of **1**, **2** and **3** were also measured in MeOH at 298 K (see Figure 2.3). The emission spectra of **1** and **2** displayed intense peaks at 587 and 458 nm respectively whereas **3** displayed a less intense peak at 442 nm and an intense peak at 608 nm (Figure 2.3). Based on previous literature involving thiol-containing diimine Re(I) tricarbonyl complexes, the emission bands can be assigned to <sup>3</sup>MLCT (triplet metal-to-ligand charge-transfer) transitions.<sup>111</sup>

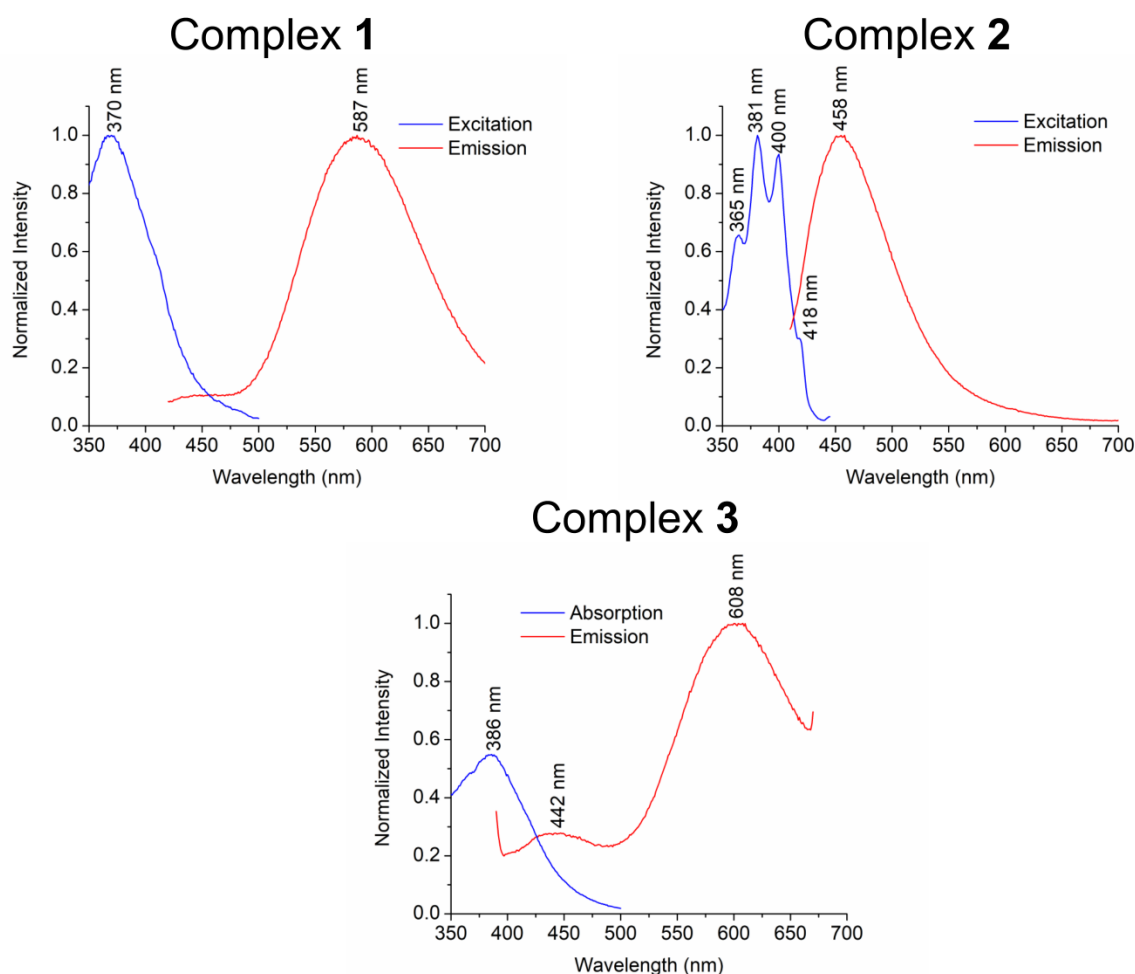


**Figure 2.3** Excitation and emission spectra of **1** , **2** and **3** in MeOH at 298 K.

The coordination of cysteine to **1** appeared to cause a large reduction in Stokes shift. In the case of **3**, this was the opposite with coordination of N-acetyl-*L*-cysteine appearing to cause an increase in Stokes shift. The increased Stokes shift and move towards the red region of the spectrum of MLCT emission band could be attributed to a difference in  $\pi$ -donation character between the *L*-cysteine and N-acetyl-*L*-cysteine as well as the aqua ligand. Complexes that possess better  $\pi$ -donating ligands will experience an increase in electron density at the metal centre, thus making the complex more susceptible to

oxidation, which in turn will cause a reduction in the MLCT energy through the destabilization of the HOMO orbitals, shifting the emission band from 587 to ca. 608 nm in the case of **1** and **3** (see Figure 2.3).<sup>115</sup> When comparing **1** and **2**, there is a change from cationic to a neutral complex with a large reduction in Stokes shift and when comparing this observation to previous literature, it could be an indication of fluorescence processes taking place due to a <sup>1</sup>ILCT (singlet intra-ligand charge-transition).<sup>111</sup> The excitation spectrum of **2** shows a vibronic band (Figure 2.3) displaying a range of electronic and vibrational states originating from the bipyridine ligand. This can be determined through conversion of the peak maxima in the vibronic band to its corresponding wavenumber. The difference between wavenumbers of the peak maxima (nm) are in the range of 1076 – 1246 cm<sup>-1</sup> which corresponds to in-plane ring and C-H bending of the bpy.<sup>116</sup> The change in emission intensity and wavelength could have potentially useful applications for cellular imaging techniques. The ability to distinguish emission peaks between drugs and the products generated through their interactions with biomolecules could provide more in-depth information on how a drug behaves in a cellular environment. Similar complexes have been used in the fluorescence imaging of yeast and human adenocarcinoma cells.<sup>117</sup> The fluorescence quantum yield ( $\Phi_F$ ) decreased upon replacement of the aqua ligand in both complexes **2** and **3**. Previous research has also shown the choice of diimine ligand on similar complexes affects the  $\Phi_F$  when replacing bipyridine with 1,10-phenanthroline (phen), causing an increase in the overall  $\Phi_F$  value.<sup>118</sup>

#### 2.4.4 Singlet Oxygen Measurements

The investigation into whether complexes **1-3** were able to produce <sup>1</sup>O<sub>2</sub> was carried out using direct detection method, measuring the near-IR luminescence of <sup>1</sup>O<sub>2</sub> at 1270 nm.

$^1\text{O}_2$  quantum yields were calculated using tris(2,2-bipyridine) ruthenium(II),  $[\text{Ru}(\text{bpy})_3]^{2+}$  ( $\Phi_\Delta = 0.81$  in air-saturated methanol) as the reference.<sup>119</sup> As seen in Table 2.2, quantum yields could only be obtained in MeOH. For complexes **1-3**, when in  $\text{H}_2\text{O}/\text{MeOH}$ , no signal could be detected upon excitation at 355 nm, neither when **1** was in  $\text{H}_2\text{O}$ .

**Table 2.2** Singlet oxygen quantum yields ( $\Phi_\Delta$ ) of **1**, **2** and **3** in air-equilibrated MeOH at 298 K

Compound	$\Phi_\Delta$ , %
	MeOH
<b>1</b>	$15.0 \pm 1.8$
<b>2</b>	$1.2 \pm 0.1$
<b>3</b>	$8.5 \pm 1.0$

The best  $^1\text{O}_2$  generator appears to be **1**, with a  $\Phi_\Delta$  of  $15.0 \pm 1.8\%$  in comparison to **2** and **3** which have  $\Phi_\Delta$  of  $1.2 \pm 0.1$  and  $8.5 \pm 1.0 \%$ , respectively. When cysteine is coordinated, no  $^1\text{O}_2$  signal could be detected indicating cysteine may have a quenching effect on the complex. The quenching effect of thiol-containing biomolecules on  $^1\text{O}_2$  has been previously demonstrated.<sup>120</sup> Interestingly, introducing the acetyl group in **3** enables it to produce  $^1\text{O}_2$  in comparison to **2**. The choice of axially attached ligand appears to play an important role in helping the complex to generate  $^1\text{O}_2$ . In a complex biological environment, the aqua ligand of **1** would be susceptible to substitution with a variety of thiol-containing biomolecules. Earlier research has shown that Re(I) tricarbonyl complexes with a diimine ligand (phen or bpy) and the axial ligand being either Cl, pyridine (py) or 2-aminomethylpyridine (ampy) have produced  $^1\text{O}_2$   $\Phi_\Delta$  of 28-55%.<sup>118</sup> This highlights the

importance of ligand choice, both axial and equatorial, when designing Re(I) tricarbonyl based photosensitizers, taking into account their lability and its potential effect on their photophysical properties. The abundance of glutathione within the cellular environment and breast cancer cells that display overexpression of metallothioneins could present an issue for such complexes in terms of reducing their efficiency.<sup>92 121</sup>

#### 2.4.5 CO Release Measurements

To further assess the photoactivity, solutions of **1** (25  $\mu$ M), **2** (12.5  $\mu$ M) and **3** (20  $\mu$ M) in MeOH were irradiated using a 365 nm UV-A hand lamp (7.105 mW/cm<sup>2</sup>), measuring their UV-vis spectra at 20-minute time intervals (see Figure A2.12). The changes in IL and MLCT bands in spectra, as well as observation of isosbestic points, would indicate conversion of one species to another through the release of a CO ligand.<sup>122</sup> The release of CO was also measured using gas chromatography with a thermal conductivity detector (GC-TCD). 50  $\mu$ M solutions of **1-3** in MeOH were irradiated using the same apparatus over a period of 2 hours with minimal to no CO being detected (see Table A2.8). The spectral changes observed for all complexes was minimal (see Figure A2.12). Earlier studies have shown that the nature of the ligand trans to CO<sub>(axial)</sub>, such as phosphine-based ligands, can have an influence on the release of axially bound CO, due to their *trans*-directing abilities.<sup>67, 102, 122</sup> For, *fac*-[Re(bpy)(CO)<sub>3</sub>(P(CH<sub>2</sub>OH)<sub>3</sub>)](CF<sub>3</sub>SO<sub>3</sub>) as a reference, the same experiment was repeated which yielded near identical results to literature values indicating the apparatus used were sufficient for monitoring CO release.<sup>67</sup> In the present study, both the HCys<sup>-</sup> and NAC<sup>2-</sup> ligands were not good *trans*-directors, and therefore, didn't induce CO release.

#### 2.4.6 Lipophilicity and partition coefficient ( $\log P$ )

Determining lipophilicity is an important indicator of the pharmacokinetic behavior of successful drugs and is most commonly quantified using the water–octanol partition coefficient ( $\log P$ ).<sup>123</sup> To estimate the lipophilicity of complex **1** and **2**, the UV-vis spectra of their solutions (**1** in H<sub>2</sub>O and **2** in 1.5% aqueous EtOH) were measured at different concentrations (see Figure A2.13) to make calibration curves. Then samples of **1** and **2** were prepared in water-octanol (see the list of samples in Figures A2.14 – A2.15.) After shaking the samples for 24 h at 25 °C, the solutions were centrifuged and aliquots from aqueous phase were taken for UV-vis measurement (see Figures A2.14 – A2.15). The amount of each complexes (**1** or **2**) in each aqueous phase was determined by comparing its absorption at 243 nm ( $\lambda_{\max}$ ) with the calibration curve. Subsequently, the concentration of complex in octanol phase could be obtained ( $C_{\text{original}} - C_{\text{aqueous}} = C_{\text{octanol}}$ ) allowing for the partition coefficient ( $\log P$ ) to be calculated. A larger  $\log P$  value correlates with increased lipophilicity. Complex **1** appears to be slightly more lipophilic than **2** with the more positive  $\log P$  value (Table 2.3).

**Table 2.3** Partition coefficient and  $\log P$  values of complexes **1** and **2**

Complex	$K_{ow}$	Log (P)
1	0.32	-0.49
2	0.31	-0.51

#### 2.4.7 Cell Viability

Complexes **1** and **2** were chosen for further cell viability assessment, tested against the MDA-MB-231 breast cancer cell line using the Alamar Blue assay. Cisplatin was also measured for comparison. The instability of complex **3** in various solvents resulted led to no further investigation on this complex. Experiments were performed at the time points of 24 and 48 hr (Figure 2.4, Table 2.4). Complex **1** displayed cytotoxicity and an  $IC_{50}$  value of  $38 \pm 6 \mu M$  over the course of 24 hours which appears to outperform cisplatin which doesn't display significant cytotoxicity at 24 h. At the time point of 48 hours, the  $IC_{50}$  value of **1** drops to  $26 \pm 3 \mu M$ , whereas that of cisplatin is  $11 \pm 2 \mu M$  (Table 2.4). An  $IC_{50}$  value of  $15.5 \pm 5.5 \mu M$  against the HeLa cell line for **1** has been previously reported.<sup>60</sup>

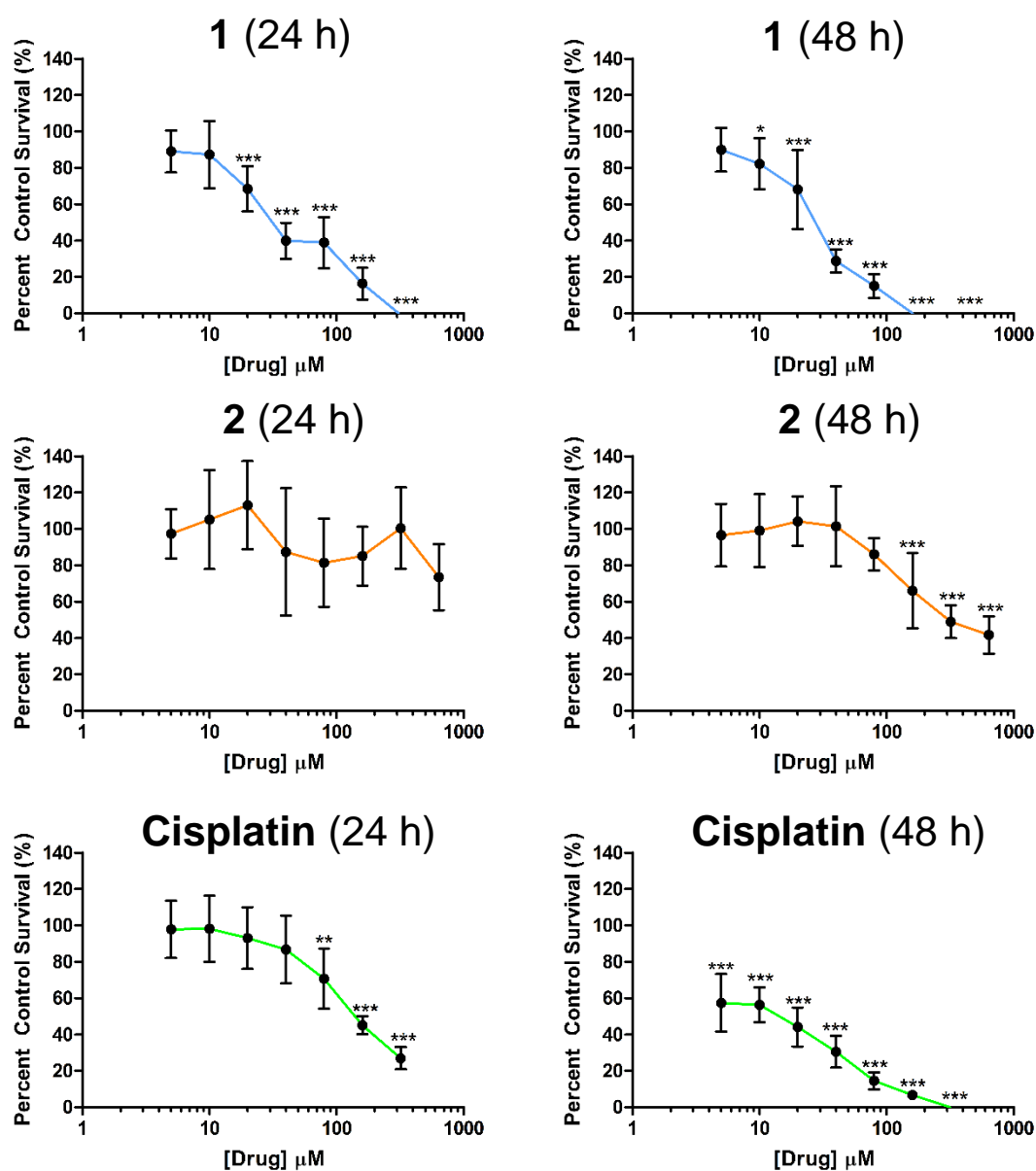


**Figure 2.4** Dose-response curve of **1**, **2** and cisplatin at 24 hrs and 48 hrs. Data are represented as means  $\pm$  standard deviations from three independent experiments with 9 biological replicates per concentration level. Data were analyzed with a one-way ANOVA followed by Dunnet post-tests from comparisons between treated and control cells.



**Table 2.4** IC<sub>50</sub> values of **1**, **2** and cisplatin in MDA-MB-231 breast cancer cells (see Fig 2.4).

	IC <sub>50</sub> (μM) <sup>a</sup>	
	24 Hours	48 Hours
<b>Re-Aqua</b>	38 ± 6	26 ± 3
<b>Re-HCys</b>	>100	>100
<b>Cisplatin</b>	>100	11 ± 2

a) Data are represented as means ± standard deviations from three independent experiments with 9 biological replicates per concentration level.

Since complex **1** displayed cytotoxic activity in the dark, its photocytotoxicity was not measured, despite its ability to produce <sup>1</sup>O<sub>2</sub> upon irradiation. An ideal photosensitizer would not be toxic in the dark, rendering applicability of complex **1** as a photosensitizer doubtful. Despite this, its activity as a chemotherapeutic drug is somewhat promising, beside other complexes with the general formula, *fac*-[Re(CO)<sub>3</sub>(N,N)(H<sub>2</sub>O)]<sup>+</sup>.<sup>60</sup> When considering **2**, the replacement of the aqua ligand in **1** with *L*-cysteine appears to have a significant impact on cytotoxicity. At both time points, IC<sub>50</sub> values of over 100 μM were recorded for **2**. An earlier study has shown that the co-administration of *L*-cysteine with cisplatin reduced the number of apoptotic cells in rats, indicating it can act as a protecting agent.<sup>124</sup> Additionally, *N*-acetyl-*L*-cysteine has been used as a protecting agent to reduce cytotoxicity caused by cisplatin.<sup>125</sup> Comparing that study with the data collected in this paper, we suggest that similar to cisplatin, the formation of a metal-sulfur bond by *L*-cysteine can reduce the cytotoxicity of the complex **1**.

#### 2.4.8 Synchrotron-based X-ray Fluorescence Microscopy (XFM)

The cellular uptake of complexes **1** and **2** were assessed and their elemental distribution maps were obtained using XFM. Due to the minimal  $\Phi_F$  values measured (Table 2.1), especially in the case of **2**, the use of XFM was preferred. XFM is different compared to other techniques such as confocal or fluorescence microscopy, since it does not rely on emissive properties of the complexes that is essential for their detection by other techniques. Additionally, there have been reports of quenching of the luminescence properties of Re organometallic in the cellular environment.<sup>65, 126, 127</sup> Figures 2.5 and A2.16 show elemental distribution maps of MDA-MB-231 breast cancer cells treated for 6 h with a solution of **1** in DMEM (20  $\mu$ M). It can be seen that there is some accumulation of Re in the nuclear region. The nuclear region can be identified via morphology in the optical image as well as by the presence of Zn, which is predominantly found in the nucleus, probably in zinc finger proteins. Zn, which is highly accumulated in the nuclear region, likely due to its presence in zinc finger proteins.<sup>106, 128</sup> When comparing the Zn and Re maps, in cells treated with **1**, there appears to be some overlap between the signal indicating colocalization between the two elements.

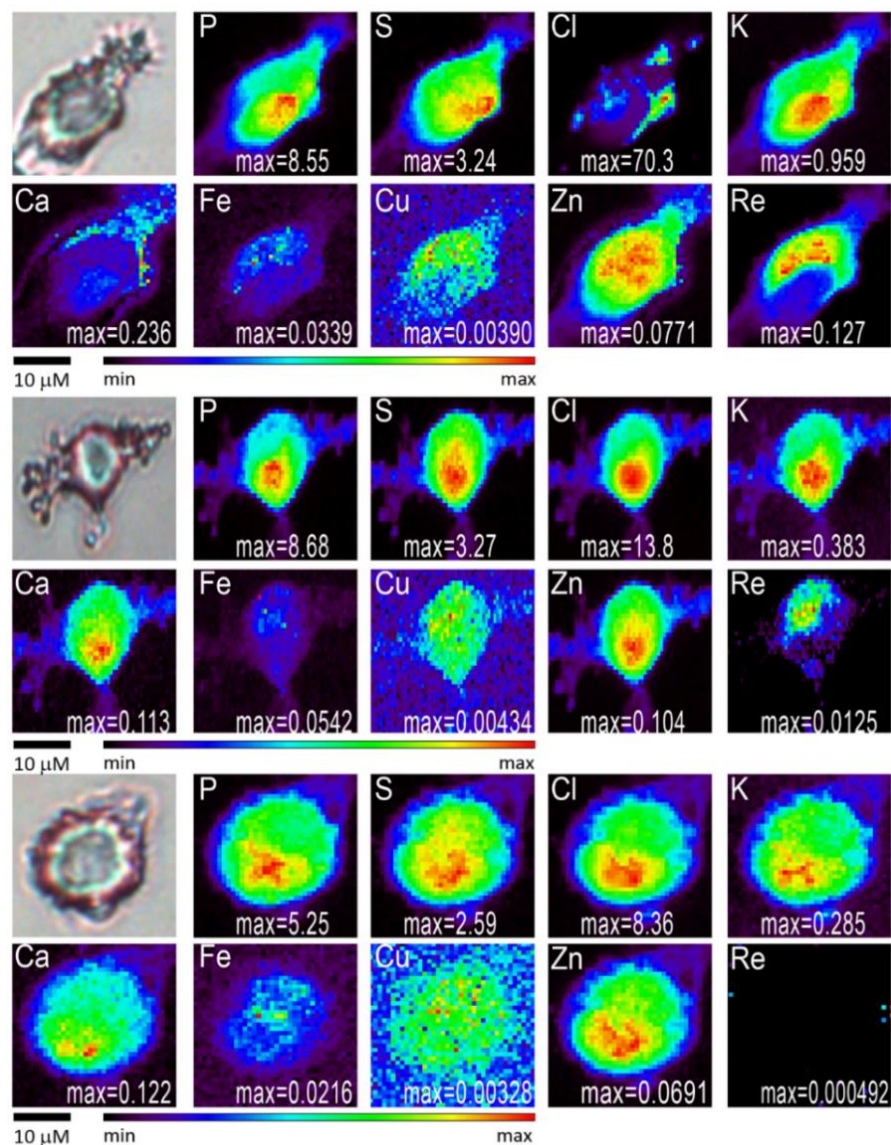


**Figure 2.5** Optical micrographs (top left), and XRF elemental distribution map of MDA-MB-231 cells treated for 6 h with **1** (top), **2** (middle) and DMEM as a control (bottom). The maximum elemental area densities (quantified from standards and expressed in  $\mu\text{g cm}^{-2}$ ) are given in the bottom of each map.

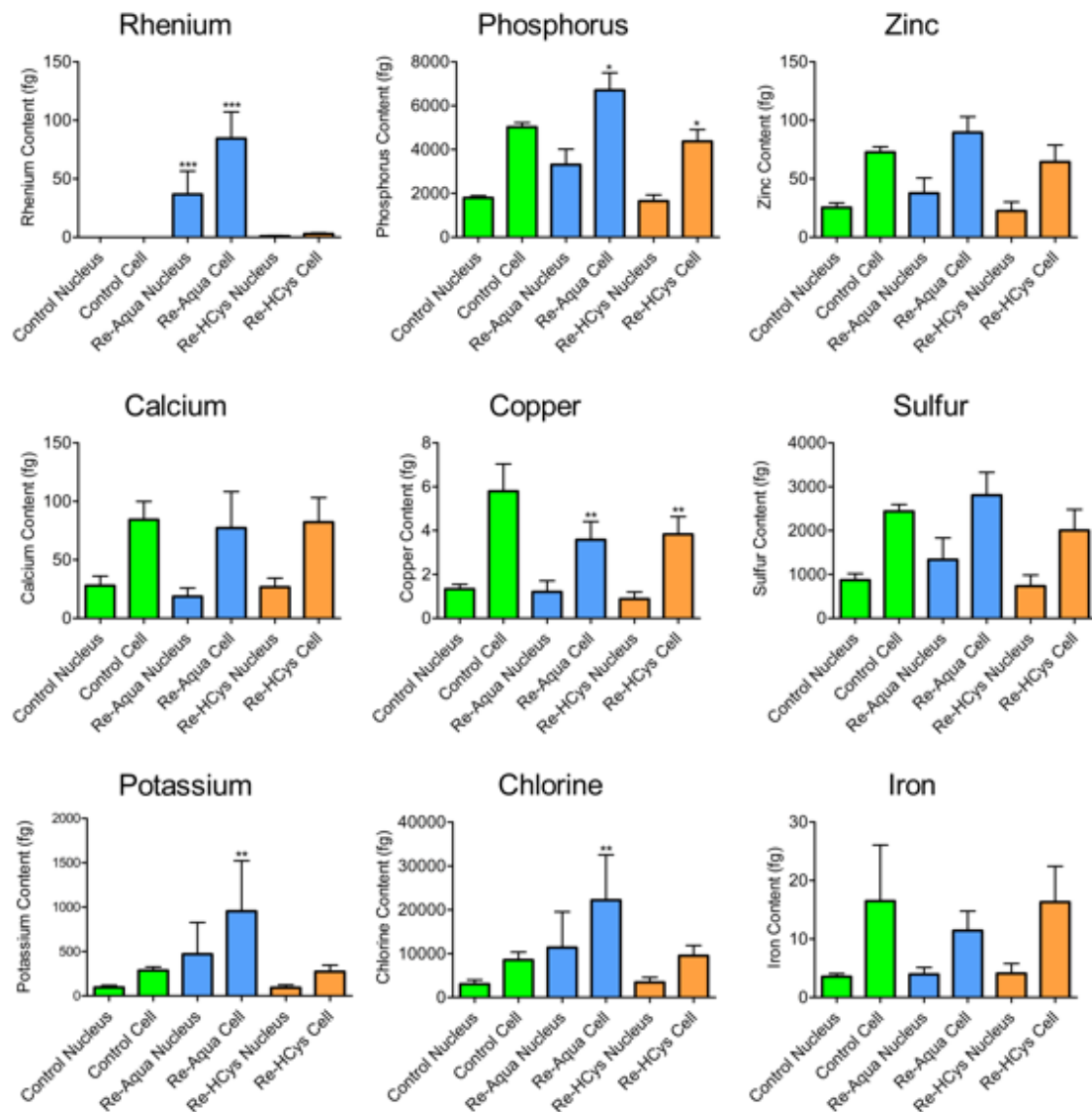


**Figure 2.6** Intracellular content of P, S, Cl, K, Ca, Fe, Cu, Zn, and Re obtained by quantification using XFM as compared with the nuclear content of MDA-MB-231 cells treated for 6 h with control (green, n=5) as well as 20  $\mu$ M solutions of **1** in DMEM (blue, n=4) and **2** in 1.5% EtOH in DMEM (orange, n=5). Error bars represent standard deviations. Data were analyzed with a one-way ANOVA followed by Tukey post-tests: \*p < 0.05; \*\* p < 0.01; \*\*\* p < 0.001 from comparisons between treated and control cell/nucleus regions.

A previous report on Re(I) tricarbonyl tetrazolato complex has shown localization of Re within the diffuse reticular network in the nuclear/perinuclear region using the same technique.<sup>128</sup> Interestingly, a complex similar to **1**, *fac*-[Re(CO)<sub>3</sub>(2,9-dimethyl-1,10-phenanthroline)(H<sub>2</sub>O)](OTf) (Figure 1.6), was initially thought to be localized in cytoplasmic vacuoles, as well as localizing diffusely throughout the cytosol, based on confocal fluorescence microscopy.<sup>60</sup> This was proven to be incorrect and later determined, through ICP-MS, that accumulation of Re occurred in the mitochondria.<sup>59</sup> It was thought that the speciation of the Re complex and its interaction with endogenous ligands affect its luminescence properties, thus limiting the effectiveness and accuracy of the technique. In the present study, the photophysical data (see Table 2.1) provides strong evidence to attest to this observation. This also highlights the importance of using alternate techniques, such as synchrotron-based XFM, to ascertain the cellular accumulation of metals. Additionally, the change in ligand appears to alter the site of cellular accumulation, which is important when targeting cellular organelles other than DNA, offering novel modes of cell death helping overcome issues such as platinum resistance mechanisms.<sup>9</sup> In the present study, it is particularly difficult to pinpoint the exact position of complex **1** in the cell, other than being present in the nuclear region, as the distribution images themselves are two-dimensional projection of three dimensional objects (dried cells).<sup>128</sup> This also applies to quantification of elemental concentrations which includes the area both over and under the nucleus such as endoplasmic reticulum.<sup>128</sup> When looking at all cells treated with **1**, an increase in K and Cl can be seen when compared to cells treated with DMEM and **2** (Fig. 2.6). An explanation to this would be that during sample preparation, DPBS is used, thus, exposing cells to higher concentrations of K and Cl.

When considering the cytotoxic activity and  $IC_{50}$  value of **2**, which was significantly reduced in comparison to **1** (Table 2.4), the elemental distribution maps offer an explanation (Fig 2.5). The Re signal in cells treated with **2** is significantly low, with no strong overlap with Zn in the nuclear region. The quantification histograms (Figure 2.6) show increased amounts of Re in the cells treated with complex **1** (n=4) as compared to complex **2**, which has little to no Re in a range of cells treated (n=5). This may indicate that the replacement of the aqua ligand in **1** with *L*-cysteine (in **2**) hinders its cellular uptake and the passage through the cell membrane. Chemotherapeutic drugs are typically administered intravenously, resulting in exposure to blood plasma and a variety of amino acids and biomolecules which become potential interaction sites before the drug reaches the cellular environment.<sup>129</sup> This highlights the importance of studies as ours which examine the interaction between potential anticancer agents and biomolecules and how this would affect activity and cellular uptake.

## 2.5 Conclusion

This study reports the syntheses of two complexes formed from the reaction of a known anticancer active complex, *fac*-[Re(CO)<sub>3</sub>(bpy)(H<sub>2</sub>O)](*CF*<sub>3</sub>*SO*<sub>3</sub>) (**1**) with thiol-containing biomolecules, i.e. the amino acid *L*-cysteine, and *N*-acetyl-*L*-cysteine, which is a potent antioxidant and has clinical applications. The crystal structure of {*fac*-[Re(CO)<sub>3</sub>(bpy)(HCys)]}<sub>4</sub>·9H<sub>2</sub>O (**2** + 1.75 H<sub>2</sub>O) is also reported. Cell viability experiments against the MDA-MB-231 breast cancer cell line using **1**, **2** and cisplatin showed **1** had a significant increase in cytotoxicity over the course of 24 hrs. When measured again at a 48 hr time point the activity of cisplatin had surpassed that of **1** indicating a different mechanism of action between the two. At both time points, the cytotoxic activity of **2** was

significantly reduced, highlighting the affect of replacing the aqua ligand in **1** with *L*-cysteine was causal. The cellular uptake was monitored using synchrotron-based X-ray fluorescence microscopy (XFM). The results showed **1** accumulated in the nuclear region co-localizing with Zn, while the entry of **2** into the cell appeared significantly hindered, explaining its reduced cytotoxic activity.

The photophysical properties of all three complexes were also assessed which included measuring the absorbance and emission spectra. The excitation and emission spectra displayed a large variance in Stokes shift between all complexes. The major change in the emission spectra when comparing **1** and the cysteine complex **2** highlights the impact of complex formation with biomolecules on emission properties and visibility by confocal / fluorescence microscopy. The generation of  $^1\text{O}_2$  in MeOH was observed for complexes **1** and **3**, but not for **2**. This indicates that the coordination of cysteine deactivates  $^1\text{O}_2$  generation. The release of CO upon irradiation with UV-A light ( $\lambda = 365 \text{ nm}$ ) was not observed for any of the complexes showing that these thiol-containing biomolecules or the aqua ligand are not good *trans*-directors for activating their trans CO group, and therefore, their Re(I) diimine tricarbonyl complexes would not be efficient as a Photodynamic Chemotherapy (PACT) agent.

## Chapter 3: The effect of sodium thiosulfate on cytotoxicity of a Re(I) tricarbonyl aqua complex

### 3.1 Abstract

Recently, diimine Re(I) tricarbonyl complexes have attracted great interest due to their promising cytotoxic effects, which in some cases surpass that of cisplatin. We will present results from our recent investigations on the cytotoxic properties and cellular uptake of two Re(I) complexes *fac*-[(Re(CO)<sub>3</sub>(bpy)(H<sub>2</sub>O)](CF<sub>3</sub>SO<sub>3</sub>) (**1**) and Na(*fac*-[(Re(CO)<sub>3</sub>(bpy)(S<sub>2</sub>O<sub>3</sub>))]·H<sub>2</sub>O (bpy = 2,2'-bipyridine) (**4**), for which the crystal structure is also reported. Their cytotoxicity was tested against the MDA-MB-231 breast cancer cell line. The cellular localization was investigated using synchrotron-based X-ray fluorescence microscopy (XFM). The results show that replacement of the aqua ligand with thiosulfate renders the complex non-toxic. This effect is similar to the chemoprotective effect of thiosulfate against cisplatin, for which the common side effects, such as hair loss and hearing changes, may be reduced through the administration of sodium thiosulfate.

### 3.2 Introduction

The treatment of cancer using metal-based drugs has risen to prominence since the discovery of cisplatin in 1965 by Barnet Rosenberg.<sup>8</sup> Following the success of cisplatin certain issues have evolved that reduce the drug's efficacy which includes toxic side effects, as well as the development of resistance mechanisms.<sup>9</sup> The side effects of cisplatin has been attributed to high lability of its leaving groups, and ease of aquation.<sup>15</sup> Co-



administration of sodium thiosulfate (STS) with cisplatin has been shown to reduce its side effects, with STS acting as a protecting agent.<sup>51, 130</sup>

Many efforts are underway to explore other metal-based chemotherapeutic agents with higher selectivity and fewer side effects. This can be achieved by taking advantage of the reactivity of transition metal complexes towards biomolecules which can be modified by varying their geometries, coordination numbers, charge, nature of coordinated ligands and redox properties, allowing specific design of complexes with anticancer activity.<sup>10</sup> Among transition metals that have been investigated are Ru(II) and Re(I) based complexes which have shown promising results.<sup>63, 131</sup> Rhenium(I) complexes with low spin  $d^6$  configuration are kinetically inert and their ligand exchange reactions are generally slow. Earlier examples of biomedical usage of Re as well as Tc, include their use as radionuclides in radiopharmaceuticals due to their respective  $\beta$  and  $\gamma$  emitting properties.<sup>54</sup>

More recently, Re(I) tricarbonyl diimine complexes with the general formula *fac*-[Re(CO)<sub>3</sub>(N,N)X]<sup>0/+</sup> (N-N = a bidentate diimine such as 2,2'-bipyridine (bpy) and 1,10-phenanthroline (phen); X = halides, H<sub>2</sub>O, pyridine derivatives, PR<sub>3</sub>) are a growing area of interest due to their anti-proliferative, photophysical and luminescence imaging properties.<sup>63</sup> In many cases, such complexes have been shown to rival cisplatin cytotoxicity against a range of human cancer cell lines, highlighting their potential as chemotherapeutic agents.<sup>126, 132-136</sup> The mechanism of action in which the complexes initiate cell death is not yet fully understood, although in many cases localization of such complexes has been shown to occur in the cytoplasm and mitochondria.<sup>63</sup> This is particularly useful when considering mechanisms of cellular resistance to platinum-based drugs in which damaged cells are able to repair the DNA adducts at an increased rate or are able to withstand

unrepaired DNA lesions.<sup>81</sup> The targeting of other cellular organelles may be an alternate method to circumvent this issue.<sup>81</sup> The emissive properties of rhenium-based complexes allow visualization with confocal and fluorescence microscopy and give a better understanding of their cellular localization. Despite this beneficial feature of Re(I) tricarbonyl complex, reliance on such emissive properties to study intracellular distribution and drug activity can be fraught with issues such as the quenching of the complex when inside the cell.<sup>65, 126, 127</sup> This has led scientists to explore other methods of investigation to understand, uptake and distribution and how complexes of this kind behave in a cellular environment.

Synchrotron-based X-ray fluorescence microscopy (XFM) is a particularly useful method since it doesn't rely on the luminescence properties, which may be limited, but instead involves X-ray fluorescence radiation. This occurs when X-rays are absorbed by an atom, leading to the ejection of an inner-shell electron. When an electron from higher energy level relaxes, it emits a fluorescent photon.<sup>137</sup> The fluorescent photon can then be detected by an energy-dispersive detector allowing for the detection and quantification of an element in a sample.<sup>137</sup> This technique has been previously used by Wedding et al. in combination with optical epifluorescence microscopy to study the cellular uptake and distribution of a neutral aryltetrazolato Re(I) complex, *fac*-[Re(CO)<sub>3</sub>(phen)X] (Re-I; X = 5-(4-Iodophenyl)tetrazolate) in 22Rv1 prostate cancer cells.<sup>128</sup> Earlier investigations had shown that tetrazolato Re(I) complexes can accumulate in different organelles, depending on the nature of the substituent group on the tetrazolate ligand.<sup>128</sup> The XFM study confirmed the stability of the Re-I complex after its uptake, remaining intact inside the cell, and provided images of its diffuse reticular localization in the nuclear/ perinuclear regions

approximately following the cell thickness, with preferential localization in cytoplasmic areas around the nucleus.

In the current study, we have investigated the cytotoxicity, cellular uptake and intracellular distribution of two Re(I) complexes: *i*) *fac*-[Re(CO)<sub>3</sub>(bpy)(H<sub>2</sub>O)](CF<sub>3</sub>SO<sub>3</sub>) (**1**) which recently has been shown to display anticancer activity,<sup>60</sup> and *ii*) Na(*fac*-[Re(CO)<sub>3</sub>(bpy)(S<sub>2</sub>O<sub>3</sub>)]·H<sub>2</sub>O (**4**), obtained from the reaction of **1** with Na<sub>2</sub>S<sub>2</sub>O<sub>3</sub> in aqueous solution. Dissolving **1** and **4** in water generates cationic *fac*-[Re(CO)<sub>3</sub>(bpy)(H<sub>2</sub>O)]<sup>+</sup> and anionic *fac*-[Re(CO)<sub>3</sub>(bpy)(S<sub>2</sub>O<sub>3</sub>)]<sup>-</sup> species in aqueous solution. The cytotoxicity of both complexes was assessed against the MDA-MB-231 breast cancer cell line, and its cellular distribution was probed using XFM. Our results show that substitution of thiosulfate renders the toxicity of the Re(I) complex, inhibiting its cellular uptake. We also report the crystal structures of Na(*fac*-[Re(CO)<sub>3</sub>(bpy)(S<sub>2</sub>O<sub>3</sub>)]·1.75 H<sub>2</sub>O·C<sub>2</sub>H<sub>5</sub>OH (**4** + 0.75 H<sub>2</sub>O + C<sub>2</sub>H<sub>5</sub>OH) and (*fac*-[Re(CO)<sub>3</sub>(bpy)(H<sub>2</sub>O)] (*fac*-[Re(CO)<sub>3</sub>(bpy)(S<sub>2</sub>O<sub>3</sub>)]·4H<sub>2</sub>O (**5**).

### 3.3 Experimental Section

#### 3.3.1 Materials

All chemicals and solvents were of reagent grade or higher. Rhenium pentacarbonyl chloride (98%), 2, 2'-bipyridine and hydrated sodium thiosulfate were obtained from Sigma Aldrich and used without further purification. Dry toluene was prepared by refluxing (110 °C) with benzophenone and Na metal under Ar.<sup>94</sup> MDA-MB-231 breast cancer cells obtained from the American Type Culture Collection (ATCC), were cultured as monolayers with Dulbecco's Modified Eagles Medium (DMEM) (Invitrogen/Gibco) supplemented with heat-inactivated foetal bovine serum (10% v/v; Sigma Life Sciences), L-glutamine (2 mM, Invitrogen), Penicillin (100 units/mL), Streptomycin (100 µg/mL) at 37°C in a 5% CO<sub>2</sub>-humidified incubator (Thermo) and were sub-cultured every 3–4 days. Complex **1** was prepared and characterized as described in Chapter 2.

#### 3.3.2 Syntheses

##### 3.3.2.1 *Na(fac-[Re(CO)<sub>3</sub>(bpy)(S<sub>2</sub>O<sub>3</sub>))]·H<sub>2</sub>O (4).*

Sodium thiosulfate (4.21 mmol) was added as solid to a completely dissolved yellow solution of **1** (0.42 mmol) in 20 mL of water; the suspension was left to stir for 48 h at room temperature. Unreacted sodium thiosulfate salt was removed by filtering the solution; the filtrate was then concentrated through rotary evaporation at 45 °C and left in the fridge in a sealed container for 48 h. The resulting yellow needle shape crystals were collected using a polyethersulfone (PES) membrane filter and washed with water and ether. Yield: 67%. <sup>1</sup>H NMR (600 MHz, D<sub>2</sub>O) δ 9.05 (ddd, J = 5.5, 1.6, 0.8 Hz, 1H), 8.49 (dt, J = 8.3, 1.0 Hz, 1H), 8.14 (td, J = 7.9, 1.6 Hz, 1H), 7.58 (ddd, J = 7.6, 5.5, 1.3 Hz, 1H), 4.82

(s, 3H).  $^{13}\text{C}$  NMR (600 MHz, 155.4 (C1, C1'), 153.2 (C3, C3'), 139.4 (C4, C4'), 127.0 (C5, C5'), 123.4 (C6, C6'). Anal. Cald. for  $\text{Na}(\text{fac}[\text{Re}(\text{CO})_3(\text{bpy})(\text{S}_2\text{O}_3)])\cdot\text{H}_2\text{O}$  ( $\text{ReC}_{13}\text{H}_{10}\text{N}_2\text{O}_7\text{S}_2\text{Na}$ ): C, 26.94; H, 1.74; N, 4.83% (3.1%  $\text{H}_2\text{O}$ ). Found: C, 27.12; H, 1.46; N, 4.88% (TGA:  $\approx$  3.0%  $\text{H}_2\text{O}$ ). IR  $\tilde{\nu}_{\text{co}}$ :  $\tilde{\nu}_{\text{co}} = 2018_{\text{axial}}, 1914_{\text{eq}}, 1882_{\text{eq}} \text{ cm}^{-1}$ . The single crystal prepared for crystallography was taken from mother liquor (ethanol/ pentane) and had the composition of  $\text{Na}(\text{fac}[\text{Re}(\text{CO})_3(\text{bpy})(\text{S}_2\text{O}_3)]) \cdot 1.75\text{H}_2\text{O} \cdot \text{C}_2\text{H}_5\text{OH}$  (**4** + 0.75  $\text{H}_2\text{O}$  +  $\text{C}_2\text{H}_5\text{OH}$ ).

### 3.3.3 Physical Measurements and Methods

#### 3.3.3.1 Single Crystal X-Ray Diffraction.

Single crystals of (**4** + 0.75  $\text{H}_2\text{O}$  +  $\text{C}_2\text{H}_5\text{OH}$ ) were grown using vapor diffusion method in EtOH/pentane, while those of  $\text{fac}[\text{Re}(\text{CO})_3(\text{bpy})(\text{H}_2\text{O})](\text{fac}[\text{Re}(\text{CO})_3(\text{bpy})(\text{S}_2\text{O}_3)])\cdot 4\text{H}_2\text{O}$  (**5**) were obtained using the same method with water/pentane as solvent. Suitable crystals were selected and mounted on a glass loop using Paratone. Diffraction experiments were performed on a Bruker Smart diffractometer equipped with an Incoatec Microfocus (graphite monochromated Cu  $\text{K}_\alpha$ ,  $\lambda = 1.54178 \text{ \AA}$ ) and an APEX II CCD detector. The crystals were kept at 173 K during data collection. Diffractions spots were integrated and scaled with SAINT<sup>138</sup> and the space groups were determined with XPREP.<sup>139</sup> Using Olex2,<sup>99</sup> the structures were solved with the ShelXT<sup>100</sup> structure solution program using Intrinsic Phasing and refined with the ShelXL<sup>101</sup> refinement package using Least Squares minimization.

### 3.3.3.2 Lipophilicity and partition coefficient (log P).

Partition coefficients (log P) were determined by the shake flask method using n-octanol and water.<sup>103</sup> Complex **1** and **4** were first dissolved in water to give 50 µM solution. Using Beer-Lambert law, the molar extinction coefficients (ε) of compounds **1** and **4** at the λ<sub>max</sub> (243 nm) were evaluated. Different ratios of complexes **1** and **4** in water (50 µM) and n-octanol were mixed using a mechanical shaker for 24 h at 25 °C. The layers were then separated using centrifugation at 5000 rpm for 10 min at 25 °C. UV-vis spectra were then taken at room temperature of the aqueous phases. Log P values were calculated using the following equation,

$$\log P = \log \left( \frac{\text{Concentration in } n - \text{octanol phase}}{\text{Concentration in water phase}} \right) \text{ (eq. 2)}$$

### 3.3.3.3 Cell Viability.

In black-walled 96-well plates, 7,500 MDA-MB-231 breast cancer cells were seeded per well at 37 °C in a 5% CO<sub>2</sub>-humidified incubator for 48 h. Stock solutions of **1** and **4** were freshly prepared in DMEM. Drug exposure periods were 24 and 48 h. The supernatants were removed via suction and each well was washed with PBS and then treated with 10% v/v alamarBlue reagent (Invitrogen) at 37 °C in a 5% CO<sub>2</sub>-humidified incubator. After 2-2.5 h, fluorescence was measured on a SpectraMax M2e Multi-detection Readers using excitation and emission wavelengths of 55-570 nm and 585-595 nm, respectively. Data were processed using GraphPad Prism Version 5.03 software.<sup>140</sup> Cell viability is reported as a percentage of the fluorescence of cells treated with either **1** or **4**

with respect to the control and were determined by three independent experiments using nine biological replicates and their standard deviations were calculated. IC<sub>50</sub> values were determined by curve fitting-plots of cell viability (%) vs. log of drug concentration.

#### ***3.3.3.4 XFM Sample preparation.***

Fresh stock solutions of **1** and **4** were prepared in DMEM (800 µM) before treatment. These solutions were then diluted with DMEM to the treatment concentration of 20 µM. Samples for XFM imaging were prepared by growing the cells on 1.5 x 1.5 mm x 500 nm silicon nitride windows (Silson, UK) in 6-well plates as described previously.<sup>141</sup> The plates were seeded at 225,000 cells per well and were allowed to attach at 37°C in a 5% CO<sub>2</sub>-humidified incubator for 24 h prior to treatment. Cells were then treated for 6 h with 20 µM solutions of **1** and **4**, or with DMEM as a vehicle-only control. At the end of the treatment time, medium was removed and cells washed with Dulbecco's phosphate-buffered saline (D-PBS). Cells were then fixed with 4% paraformaldehyde (prepared fresh in D-PBS) solution for 1 h in a 37 °C in a 5% CO<sub>2</sub>-humidified incubator. Fixed windows were then washed ammonium acetate in Milli-Q water (100 mM) two times to remove excess fixatives (and NaCl) and left to dry overnight.<sup>105, 106</sup>

#### ***3.3.3.5 XFM data collection.***

Elemental distribution maps of single cells were recorded on beamline 2-ID-D at the Advanced Photon Source (APS), Argonne National Laboratory, Illinois, USA. The X-ray beam was tuned to an incident energy of 12.8 keV to excite the Re L<sub>β</sub> emission line (E= 10,010.0 eV) using a double crystal monochromator. The X-ray beam was focused to a spot size of 0.35 µM on the sample using two Fresnel zone plates. A single element silicon

drift energy dispersive detector (Vortex EX, SII Nano-technology, Northridge, CA), was used to collect the X-ray fluorescent spectra from the samples which were placed under a He atmosphere at 75° to the incident beam. All elemental maps were recorded using the step-scan mode, with a 0.5  $\mu\text{m}$  step-size and a 1000 ms dwell time. Four to five cells were selected using an optical microscope to be imaged.

#### ***3.3.3.6 XRF imaging data analysis.***

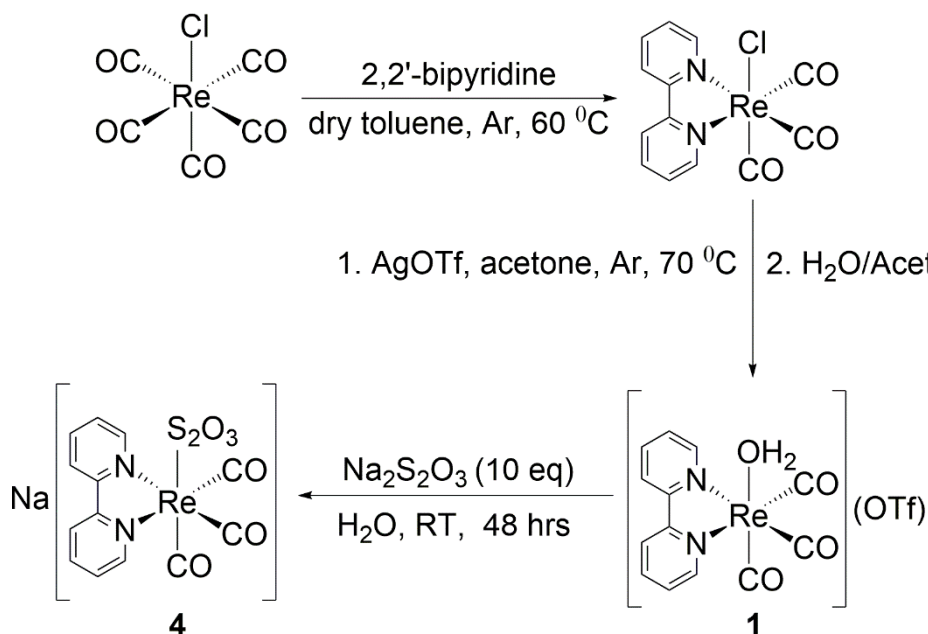
The fitting of raw fluorescence emission spectra to Gaussians at each spatial point allowed for the generation of elemental maps (in units of  $\mu\text{g cm}^{-2}$ ) as well as regions of interest (ROIs).<sup>107, 108</sup> Rhenium images were obtained by fitting its  $L_{\beta}$  emission line (10010.0 eV), since its  $L_{\alpha}$  line (8586.2 eV) almost overlaps with the Zn  $K_{\alpha}$  (8638.9 eV) fluorescence line (See Figure A3.9). Quantification was performed through comparison of X-ray fluorescence intensity to the thin-film standards, NBS-1832 and NBS-1833, from the National Bureau of Standards (Gaithersburg, MD). The analysis was performed using MAPS software.<sup>108, 109</sup>



### 3.4 Results and Discussion

#### 3.4.1 Syntheses and characterization of the Re(I) thiosulfate complex

*fac*-[Re(CO)<sub>3</sub>(bpy)(H<sub>2</sub>O)](CF<sub>3</sub>SO<sub>3</sub>) (**1**) was synthesized as previously described from *fac*-[Re(CO)<sub>3</sub>(bpy)(Cl)] (See Supporting Information).<sup>60, 95</sup> The reaction between **1** and Na<sub>2</sub>S<sub>2</sub>O<sub>3</sub> in water led to the formation of crystalline Na(*fac*-[Re(CO)<sub>3</sub>(bpy)(S<sub>2</sub>O<sub>3</sub>)]·H<sub>2</sub>O (**4**). Both complexes **1** and **4** displayed good solubility in water. Scheme 3.1 provides an overview of syntheses of the Re(I) complexes **1**, **4**:



**Scheme 3.1** Synthesis of **1** from Re(CO)<sub>5</sub>Cl and the subsequent reaction between **1** and sodium thiosulfate to form **4**.

Complex **4** was characterized using NMR and FT-IR spectroscopy as well as electrospray ionization mass spectrometry (ESI-MS). Its ESI-mass spectrum in (-) ion mode displayed peaks at  $-m/z = 382.87$  and  $538.94$  amu for [Re(CO)<sub>3</sub>(S<sub>2</sub>O<sub>3</sub>)]<sup>-</sup> and [Re(CO)<sub>3</sub>(bpy)(S<sub>2</sub>O<sub>3</sub>)]<sup>-</sup>, respectively. Also, intense mass peaks at  $+m/z = 427.01$ ,  $540.95$  and  $557.98$  amu, corresponding to [Re(CO)<sub>3</sub>(bpy)]<sup>+</sup>, [Re(CO)<sub>3</sub>(bpy)(S<sub>2</sub>O<sub>3</sub>) + 2H<sup>+</sup>]<sup>+</sup> and

$[\text{Re}(\text{CO})_3(\text{bpy})(\text{S}_2\text{O}_3) + \text{H}^+ + \text{NH}_4^+]^+$ , were detected in the (+) ion mode (see Figure A3.4, Table A3.1).

The  $^1\text{H}$  and  $^{13}\text{C}$  NMR signals observed for **4** were shifted up-field in comparison to **1** which can be explained by the increased electron density experienced by  $\text{Re}(\text{I})$  ion donated by S, when replacing the aqua ligand with the thiosulfate group (Figure A3.1). A similar effect is observed when comparing the characteristic  $\text{C}\equiv\text{O}$  bond stretching frequencies in the FT-IR spectra of complexes **1** and **4**, which occur at  $2033$  and  $2018\text{ cm}^{-1}$ , respectively, corresponding to the totally symmetric in-phase  $\nu(\text{CO})$  vibration, denoted as  $\text{A}'(1)$ . (Figure A3.2).<sup>110</sup> The reason for observing this shift to a lower frequency is that the increased electron density on  $\text{Re}(\text{I})$  ions in **4** is  $\pi$ -back donated to the  $\pi^*$  of the carbonyl groups, thus weakening the C-O bond which in turn, reduces its vibrational frequency. Further vibrations correspond to the out-of-phase totally symmetric  $\text{A}'(2)$  vibration and the asymmetric vibration of the equatorial CO ligands denoted  $\text{A}''$ , were seen at  $1914\text{ cm}^{-1}$  in **1**, and  $1914$  and  $1884\text{ cm}^{-1}$  in **4** (Figure A3.2).<sup>110</sup> The appearance of a single broad band in **1**, and two sharper peaks in **4** relate to the electron density of the axial ligand. Typically, the separation of two lower frequency bands are observed in complexes bearing halide, O- or P- coordinated ligands whereas one broad band occur in N-coordinated ligands although this is not the case for **1**.<sup>110</sup> The separation of the  $\text{A}'(2)$  and  $\text{A}''$  vibrations is in agreement with similar  $\text{Re}(\text{I})$  tricarbonyl diimine complexes that contain axially bound S-containing ligands.<sup>142, 143</sup>

### 3.4.2 Single Crystal X-ray Diffraction

Initially, the crystalline bulk solid of **4** was recrystallized using vapour diffusion methods in water/pentane. This produced crystals with the formula (*fac*-[Re(CO)<sub>3</sub>(bpy)(H<sub>2</sub>O))](*fac*-[Re(CO)<sub>3</sub>(bpy)(S<sub>2</sub>O<sub>3</sub>))] $\cdot$ 4H<sub>2</sub>O (**5**) which was contradictory to elemental analysis and NMR data of **4**. Instead, using EtOH/pentane as solvent produced single crystals with the formula Na(*fac*-[Re(CO)<sub>3</sub>(bpy)(S<sub>2</sub>O<sub>3</sub>))] $\cdot$ 1.75H<sub>2</sub>O  $\cdot$  C<sub>2</sub>H<sub>5</sub>OH (**4** + 0.75 H<sub>2</sub>O + C<sub>2</sub>H<sub>5</sub>OH). Crystal data and refinement parameters for both Re(I) crystal structures are presented in Table A3.2 and A3.5, with interatomic distances and bond angles reported in Tables A3.3 - A3.4 and A3.6 - A3.7.

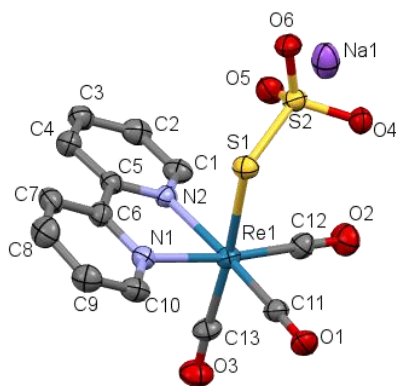


**Figure 3.1** Crystal Structure of Na(*fac*-[Re(CO)<sub>3</sub>(bpy)(S<sub>2</sub>O<sub>3</sub>)])·1.75H<sub>2</sub>O·C<sub>2</sub>H<sub>5</sub>OH (**4** + 0.75 H<sub>2</sub>O + C<sub>2</sub>H<sub>5</sub>OH) Ellipsoids are drawn at the 50% probability level. H<sub>2</sub>O and EtOH solvent molecules and H atoms attached to C atoms have been omitted for clarity.

The crystal structure of solvated **4** contains four crystallographically different Re(I) centres, in which the Re-S bond lengths are in a narrow range of 2.511(2) and 2.525(2) Å for each subunit (Table A3.3). This is in agreement with the reported range for Re-S bond distances in similar [Re(CO)<sub>3</sub>(N,N)X] complexes with varying axially bound S-donor

ligands including thiolates, thiones and thiocarbamates (See Table A3.8).<sup>142, 144, 145</sup> The replacement of the aqua ligand in **1** with thiosulfate in **4** appeared to slightly elongate the bond length of the axially bound CO ligand from Re-C<sub>axial</sub> 1.88(1) Å in **1**<sup>95</sup> to 1.906(7) – 1.933(7) Å in **4** (see Table A3.3), however, it did not have any significant impact on other Re-ligand distances. Similar complexes containing P-, N- and O- coordinating ligands also display limited variance in other Re-ligand distances further highlighting the distinct relationship between both the axially bound CO and ligand of the complex.<sup>60</sup>

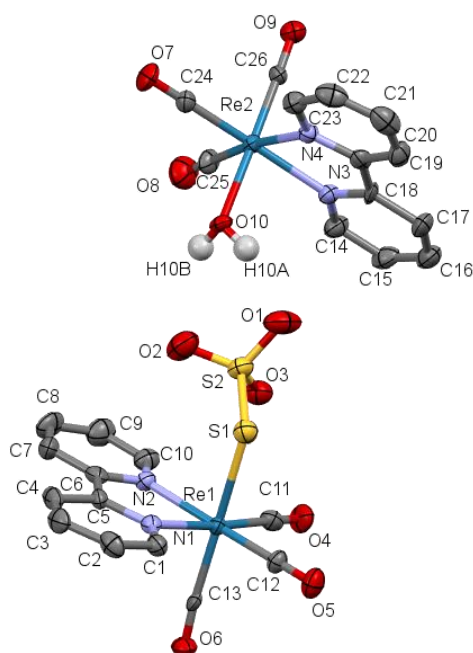


**Figure 3.2** Crystal Structure of *fac*-[Re(CO)<sub>3</sub>(bpy)(H<sub>2</sub>O)](*fac*-[Re(CO)<sub>3</sub>(bpy)(S<sub>2</sub>O<sub>3</sub>)]·4H<sub>2</sub>O (**5**) Ellipsoids are drawn at the 50% probability level. H<sub>2</sub>O solvent molecules and H atoms attached to C atoms have been omitted for clarity.

In the *fac*-[Re(CO)<sub>3</sub>(bpy)(S<sub>2</sub>O<sub>3</sub>)]<sup>−</sup> complex ion in the crystal structure of **5** (shown in Figure 3.2), the Re-S distance of 2.481(3) Å is considerably shorter, and consequently

the trans carbonyl Re-C bond length 1.941(10) Å is longer than the corresponding distances in **4**. In the counter Re(I)-aqua cation, the Re-C<sub>axial</sub> trans to the aqua ligand is 1.889(10) Å. When using vapour diffusion methods with water as the solvent and pentane as the precipitant, long needle like crystals of **5** form almost instantaneously once exposed to a lower temperature (4 °C). Under similar conditions, when EtOH is the solvent, smaller more dense crystals of **4** are grown. The difference in preparation, time and visual characteristics along with the solved structures indicate a different mechanism of growth when using the two methods. It appears that using water/pentane leads to a significantly faster rate of supersaturation and nucleation that produces a different product. Solvent-solute interactions have been shown to impact nucleation and growth kinetics which includes the metastable zone width that ultimately effects the products particle size distribution and final crystal shape.<sup>146</sup>

### 3.4.3 Lipophilicity and partition coefficient (log P)

The activity of drug candidates may often be correlated to their lipophilicity. The choice of ligands can have an impact on the lipophilicity of metal complexes and their overall charge. Lipophilicity is an important general determinant of the pharmacokinetic behavior of successful drugs and is commonly quantified in terms of the water-octanol partition coefficient (log P).<sup>123</sup> The amount of each complexes (**1** or **4**) in each aqueous phase was determined by comparing its absorption at 243 nm ( $\lambda_{\text{max}}$ ) with the calibration curve (see Figure A3.5). The concentration of the complex in the octanol layer can then be calculated allowing for the calculation of the partition coefficient (log P).

**Table 3.1** Partition coefficient and log P values of complexes **1** and **4**.

Complex	P	Log (P)
1	0.32	-0.49
4	0.0092	-2.04

When considering the log P values in Table 3.1 for **1** and **4**, it can be seen that the replacement of the aqua ligand with thiosulfate, results in a more negative value. This indicates that **4** will be less lipophilic than that of **1**. The decreased lipophilicity of **4** could have an effect on the complex cytotoxicity, i.e. it will not pass through the cell membrane barrier as easily as **1**.

### 3.4.3 Cell Viability

The cell viability of complexes **1**, **4** and cisplatin were assessed against the MDA-MB-231 breast cancer cell line using the alamarBlue assay and IC<sub>50</sub> values were determined (Table 3.1). The cytotoxicity of **1** had been previously measured against the HeLa cell line displaying an IC<sub>50</sub> value of  $15.5 \pm 5.5 \mu\text{M}$ .<sup>60</sup> In the current study, complex **1** displayed moderate cytotoxicity of  $38 \pm 6 \mu\text{M}$  over the course of 24 h (Table 3.1) whereas both cisplatin and **4** were both  $>100 \mu\text{M}$ . The cytotoxicity of cisplatin we obtained corresponds with a previously reported IC<sub>50</sub> value of  $>100 \mu\text{M}$  measured over the course of 24 h using the MTT assay.<sup>147</sup> At 24 h, it appears that **1** is more toxic towards the MDA-MB-213 breast cancer line. At the time point of 48 h, the IC<sub>50</sub> of **1** decreased to  $26 \pm 3 \mu\text{M}$

whereas cisplatin was  $11 \pm 2 \mu\text{M}$ . An  $\text{IC}_{50}$  value of  $23 \mu\text{M}$  at 48 h measured using the MTT assay was previously reported for cisplatin.<sup>147</sup>

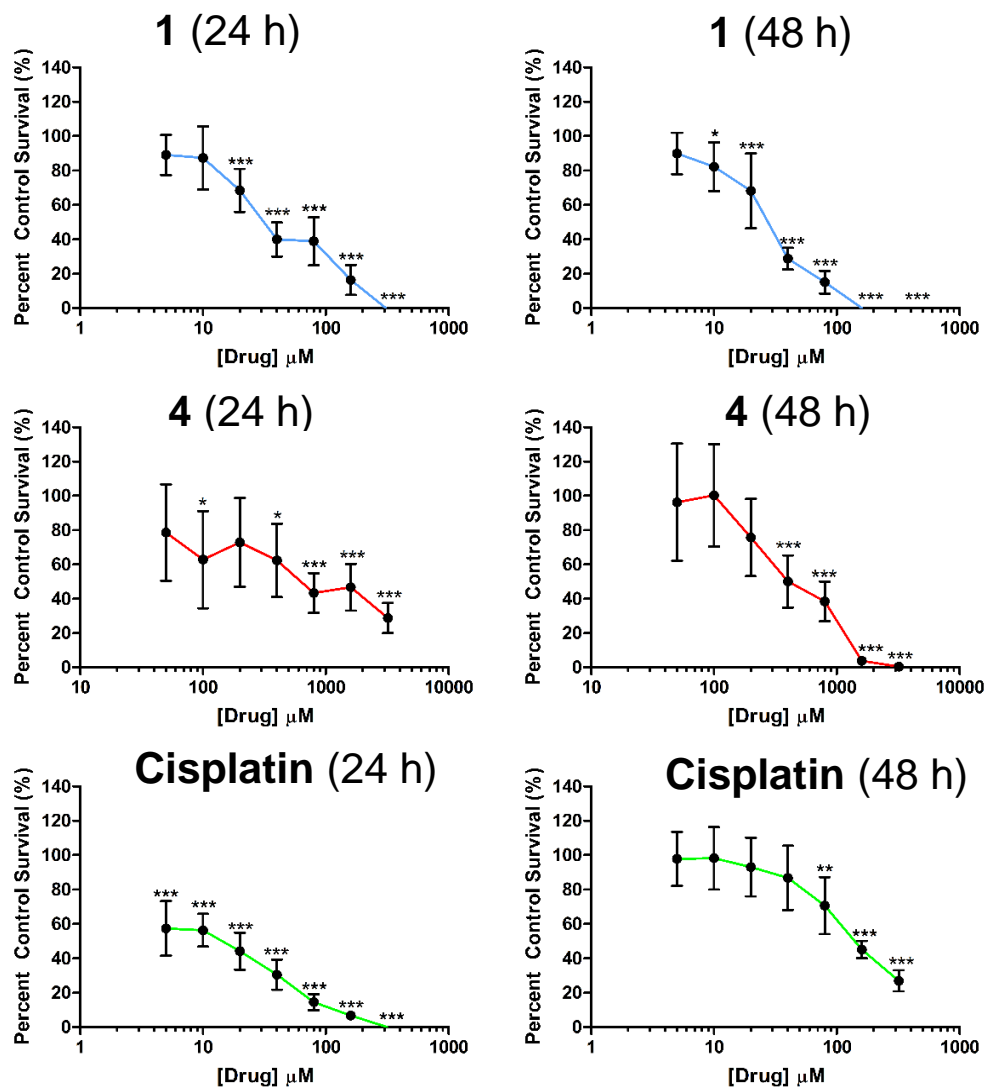


**Figure 3.3** Cell viability data in MDA-MB-231 breast cancer cells when treated with **1**, **4** and cisplatin for 24 h and 48 h. Data are represented as means  $\pm$  standard deviations from three independent experiments with 9 biological replicates per concentration level. Data were analyzed with a one-way ANOVA followed by Dunnet post-tests: \*p < 0.05; \*\* p < 0.01; \*\*\* p < 0.001 from comparisons between treated and control cells.

**Table 3.2** IC<sub>50</sub> values of **1**, **4** and cisplatin against MDA-MB-231 breast cancer cells.

Complex	IC <sub>50</sub> (μM)	
	24 Hours	48 Hours
<b>1</b>	38 ± 6	26 ± 3
<b>4</b>	>100	>100
<b>Cisplatin</b>	>100	11 ± 2

a) Data are represented as means ± standard deviations from three independent experiments with 9 biological replicates per concentration level.

When initially assessing the cytotoxicity **4**, concentrations of up to 800 μM were used but minimal cytotoxicity was observed. The dosage was increased 10-fold in comparison to concentrations used for **1** and cisplatin. Cell death occurred at concentrations of over 1600 μM of cell treated with **4**. When comparing the dose-response curve for both complexes (Figure 3.3), it can be seen that the cytotoxicity in **1** occurs at a much lower dosage in comparison to **4**. This indicates that the replacement of the aqua ligand in **1** with thiosulfate decreases its overall cytotoxicity, highlighting the importance of the nature of the axial ligand, and the counteracting effect of sodium thiosulfate on such chemotherapeutics.

#### *3.4.5 Synchrotron-based X-ray Fluorescence Microscopy (XFM)*

Cellular uptake and localization of complexes **1** and **4** in MDA-MB-231 breast cancer cells were monitored using XFM. Comparison between the elemental distribution images in Figure 3.4 and the quantification histograms in Figure 3.5 shows a significant



accumulation of Re in cells treated with **1** as opposed to cells treated with **4**. This indicates that replacing the aqua ligand in **1** with thiosulfate (in **4**) hinders its transportation into the cell, explaining the reduced cytotoxicity of **4** (Table 1). Moreover, a closer look at the Re distribution inside the cells treated with **1** reveals an accumulation in the nuclear region, which can be recognized from the optical image.<sup>106</sup> Moreover, the Re distribution map of **1** (Figure 3.4) shows that Re is co-localized with Zn, which is highly accumulated in the nuclear region due to its presence in zinc finger proteins.<sup>128</sup> Interestingly, it does not colocalize with P, which is found in the backbone of DNA and RNA, phospholipids (cell membrane proteins) and other P-containing proteins, as well as adenosine triphosphate (ATP) and other P-containing biomolecules.

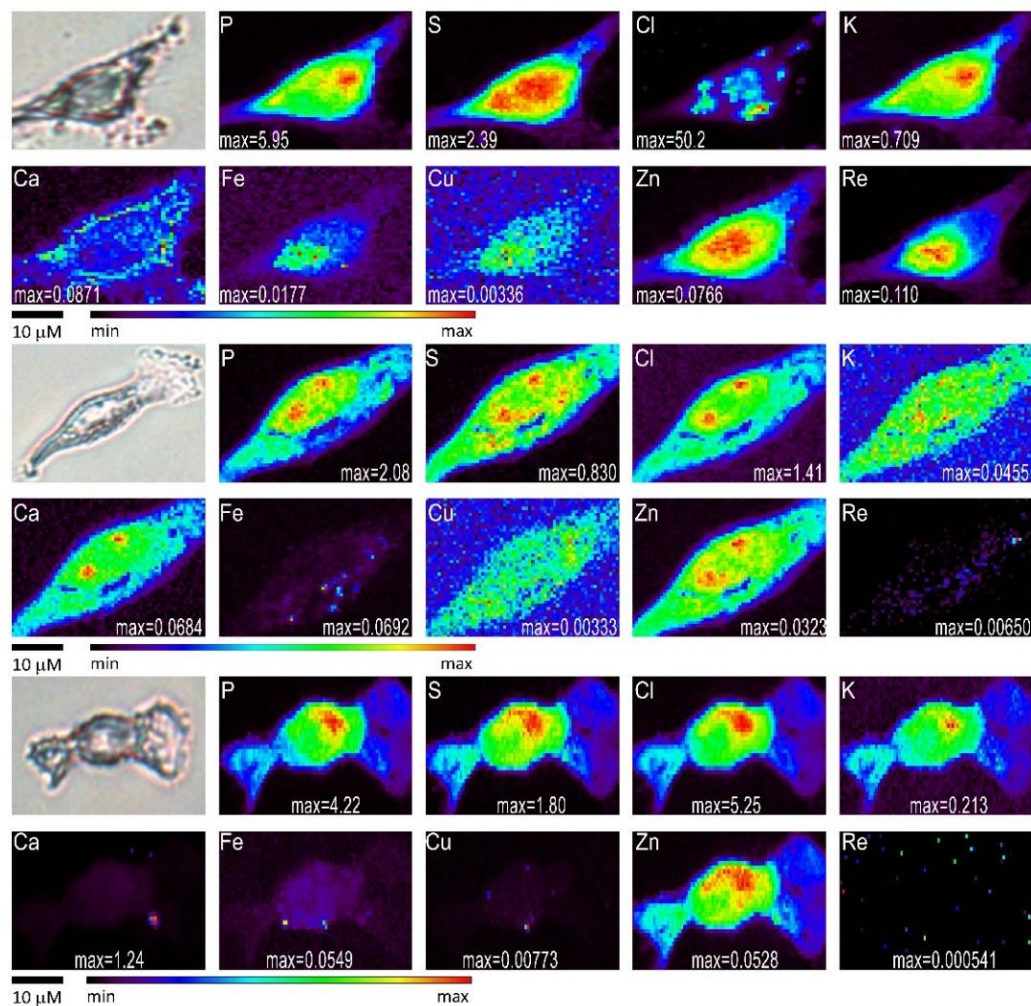


**Figure 3.4** Optical micrographs (top left), and XRF elemental distribution map of MDA-MB-231 cells treated for 6 h with **1** (top), **4** (middle) and DMEM (bottom; control). The maximum elemental area densities (quantified from standards and expressed in  $\mu\text{g cm}^{-2}$ ) are given in the bottom of each map.

Similar Re localization within the diffuse reticular network in the nuclear/perinuclear region has been previously reported for a neutral Re(I) tricarbonyl tetrazolato complex with co-localization also occurring between only Zn and Re.<sup>128</sup>. A change in axial ligand appears to affect the accumulation area for such Re based complexes.

For instance, the replacement of the axial ligand in complexes with the formula *fac*-[Re(CO)<sub>3</sub>(bpy)(X)] (X= 3-chloromethyl pyridyl) result in localization in the mitochondria.<sup>148</sup>

Quantification of each element was performed by measuring the counts of each element vs. the standards. Increased amounts of K and Cl seen in cells treated by complex **1** in comparison to both cells treated with DMEM as control and **4** can be explained by the use of D-PBS when preparing the sample windows which would expose cells to higher concentrations of these elements. An increase in Ca, seen in cells treated with **4**, is thought to be down to a single anomalous result in one cell. This is highlighted by the large statistical difference (Figure 3.5) and it is not thought that **4** is having any specific activity on Ca levels. A slight decrease in Cu levels is also seen in cells treated with **1** in comparison to cells treated with **4** and DMEM. The reduction of Cu level is a strategy in cancer treatment which involves the use of copper chelators such as D-Penicillamine (D-Pen), tetrathiomolybdate, clioquinol, and trientine which have been shown both in *vitro* and in *vivo* to inhibit angiogenesis.<sup>149</sup> It should be noted that due to the complex nature of angiogenesis, there isn't any in *vitro* assay that can model this process. Without angiogenesis, tumor cells cannot be supplied with essential oxygen and nutrients limiting their growth size to 1-2 mm in diameter.<sup>150</sup> It is uncertain as to the mechanism of which **1**

but investigation of essential element concentrations in the cellular environment could provide a window into the mechanism of action of such complexes.

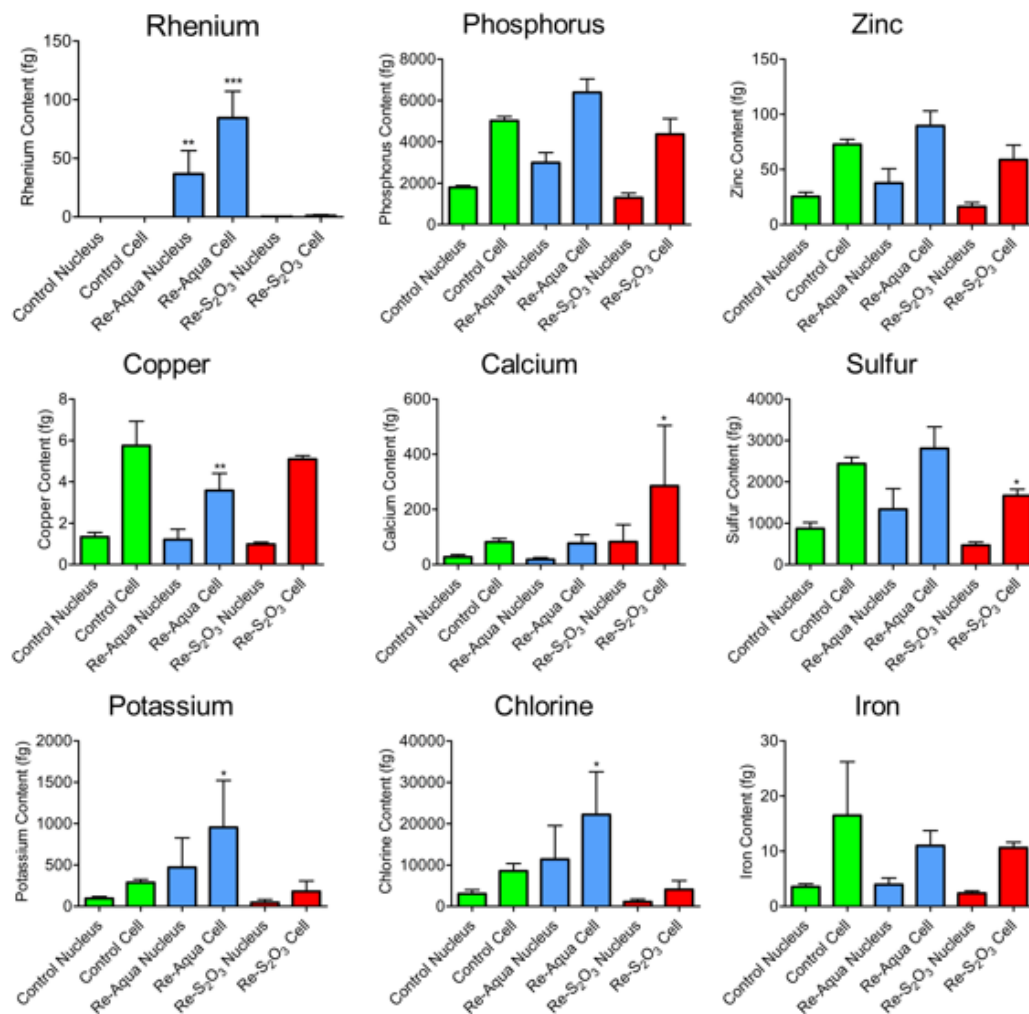


**Figure 3.5.** Intracellular content of P, S, Cl, K, Ca, Fe, Cu, Zn, and Re obtained by quantification using XFM as compared with the nuclear content of MDA-MB-231 cells treated for 6 h with control (green, n=5) as well as 20  $\mu$ M solutions of **1** (blue, n=4) and **4** (red, n=4) in DMEM. Error bars represent standard deviations. Data were analyzed with a one-way ANOVA followed by Tukey post-tests: \* $p < 0.05$ ; \*\* $p < 0.01$ ; \*\*\* $p < 0.001$  from comparisons between treated and control cell/nucleus regions.

### 3.6 Conclusion

Upon the replacement of the aqua ligand in *fac*-[Re(CO)<sub>3</sub>(bpy)(H<sub>2</sub>O)](CF<sub>3</sub>SO<sub>3</sub>) (**1**) with thiosulfate in Na(*fac*-[Re(CO)<sub>3</sub>(bpy)(S<sub>2</sub>O<sub>3</sub>)])·H<sub>2</sub>O (**4**), the cytotoxicity against the MDA-MB-231 breast cancer cells is drastically reduced. XFM images show high accumulation of the cationic complex *fac*-[Re(CO)<sub>3</sub>(bpy)(H<sub>2</sub>O)]<sup>+</sup> (of **1**) in areas outside the nucleus as well as localization with Zn inside the nucleus, whereas cellular uptake of **4** was considerably less. It is concluded that coordination of thiosulfate to Re(CO)<sub>3</sub>(bpy)<sup>+</sup> core generates a negatively charged species *fac*-[Re(CO)<sub>3</sub>(bpy)(S<sub>2</sub>O<sub>3</sub>)]<sup>-</sup> with lower lipophilicity that cannot pass easily through the cell membrane, preventing its cellular uptake. To the best of our knowledge, this is the second anticancer agent (after cisplatin) that is inhibited by thiosulfate.

## Chapter 4 Future Work and Conclusions

### 4.1 Design of an ideal photosensitizer and PACT agent

In this study, the photophysical and cytotoxic properties of a library of complexes with the general form, *fac*-[Re(CO)<sub>3</sub>(bpy)(X)]<sup>-/0</sup> where X was varying S-containing ligands, were examined. In the case of **2** and **3**, the small structural change of an acetyl group caused a notable variance in the stability, photophysical and <sup>1</sup>O<sub>2</sub> generating properties. In the case of **2** and **4**, when either thiosulfate or *L*-cysteine was coordinated the cytotoxicity was significantly reduced. The models studied here highlight some important features in the design of Re(I) tricarbonyl complexes as both chemotherapeutics and photosensitizers.

One of the main outcomes of this study would include further development of Re(I) tricarbonyl complexes. Ideally, the development of a complex that can absorb green/red visible light, generate generous amounts <sup>1</sup>O<sub>2</sub> and release CO would be desired. This could be achieved in a number of ways involving the altering of the axial ligand and equatorial diimine ligand. The current study has indicated that S-coordinated ligands are not particularly efficient at releasing CO. Previous research has shown that phosphine ligands, e.g. P(CH<sub>2</sub>OH)<sub>3</sub>, coordinated to Re(I) can induce CO release upon irradiation as well as generate <sup>1</sup>O<sub>2</sub>. One of the drawbacks of this study was that the irradiation wavelength was 365 nm. Irradiating with UVA light is problematic for several reasons, due to its cellular damaging effect.<sup>151</sup> A way to address this issue would be the use of more conjugated diimine ligands to bathochromically shift the absorbance of the complex towards the green/red light region. Take for instance the metal-organic dyad TLD1433, a Ru based PS that is currently in clinical trials for use in PDT.<sup>74</sup> The use of a functionalized ligand (PDT

ligand) contributes to the accessible  $^3\text{IL}$  state. The triplet excited state lifetimes tend to increase along with the number of these functionalized ligands.<sup>74</sup> Due to the affinity of Re(I) for diimine ligands this same method could be used to improve the photophysical properties of Re(I) tricarbonyl complexes and shift absorbance into the PDT window.

Additionally, the recent report shown the *in vivo* antitumor activity of a Re based complex was a promising sign in the development of Re based drug candidates.<sup>59</sup> Using the same methodology applied in Chapter 3, the reactions between this complex and sodium thiosulfate could be performed. While the complex itself has been shown to be mitochondrial selective, helping circumvent resistance mechanisms, the issue of unwanted toxicity could potentially be solved using this method. Additionally, the photophysical data presented gives insight into the pitfalls of using certain techniques for the identification of cellular accumulation sites.

Overall, the work displayed here provides some interesting information which ideally would benefit the development of potential chemotherapeutics and photosensitizers.

## Appendix

### Chapter 2: Supporting Information

#### *Syntheses*

##### *Synthesis of fac-[Re(CO)<sub>3</sub>(bpy)(Cl)].*

2, 2'-Bipyridine (2.76 mmol) was added to Re(CO)<sub>5</sub>Cl (2.76 mmol) in 150 mL of dry toluene instantly forming a yellow precipitate. The reaction mixture was heated under reflux at 60 °C for 2 h. The reaction mixture was then left overnight in a freezer (T= -10°C). The bright yellow product was filtered and left to dry at 65 °C using calcium chloride as a drying agent. Yield: 97%. <sup>1</sup>H NMR (400 MHz, CD<sub>3</sub>CN) δ 9.05 – 8.99 (d, 2H), 8.43 (dt, J = 8.1, 1.1 Hz, 2H), 8.20 (td, J = 7.9, 1.6 Hz, 2H), 7.63 (ddd, J = 7.6, 5.5, 1.3 Hz, 2H).

#### *Physical Measurements and Methods*

##### *NMR Spectroscopy.*

<sup>1</sup>H and <sup>13</sup>C-NMR spectra were recorded at room temperature with a Bruker AVIII-600 CFI-600 spectrometer using D<sub>2</sub>O (for **1**) and CD<sub>3</sub>OD (for **2**). For **3** and the above complex, <sup>1</sup>H spectra were recorded at room temperature using a Bruker AVIII-400 spectrometer. <sup>1</sup>H NMR were internally referenced using either the HOD/H<sub>2</sub>O peak at 4.80 ppm or the CD<sub>3</sub>OD peak at 3.31 ppm with a total of 64 scans being coadded in all cases.<sup>152</sup> <sup>13</sup>C NMR spectra were recorded using the UDEFT pulse sequence and broadband proton decoupling at 151 MHz. <sup>13</sup>C NMR spectra were externally calibrated using CH<sub>3</sub>OH in D<sub>2</sub>O or internally referenced using CD<sub>3</sub>OD with both signals resonating at 49.15 ppm, with



10240 scans being coadded in all cases.<sup>153</sup> 30° pulse, 26.2 kHz sweep width, 1-s delay between scans, and 65 K data points were used.

### ***FT-IR Spectroscopy.***

An Agilent Cary 630 FT-IR instrument with a diamond ATR accessory was used to measure the vibrational spectra of the samples collecting 500 scans.

### ***ESI-Mass spectrometry.***

Electrospray ionization (ESI) mass spectra in both positive (+) and negative (-) ion modes, were collected using an Agilent 6520 Accurate-Mass Q-TOF. Solutions of **1**, **2** and **3** in MeOH were injected and mobilized using an injection flow rate of 0.2 mL/min. The source was held at 200 °C with a drying gas flow rate of 7 L/min and a nebulizer pressure of 12 p.s.i. Fragmentor, capillary and skimmer voltages were at the respective setting of 80, 4000 and 65 V. Using a high-resolution Isotope Distribution Calculator from Scientific Instrument Services, peak assignments were confirmed.<sup>154</sup>

### ***Thermogravimetric Analysis.***

Using a Netzsch STA 409 PC Luxx instrument thermogravimetric analysis was performed. The analyses were run from room temperature to 450 °C using a ramp rate of 2 °C min<sup>-1</sup> under a flow of N<sub>2</sub>.

## NMR Spectroscopy

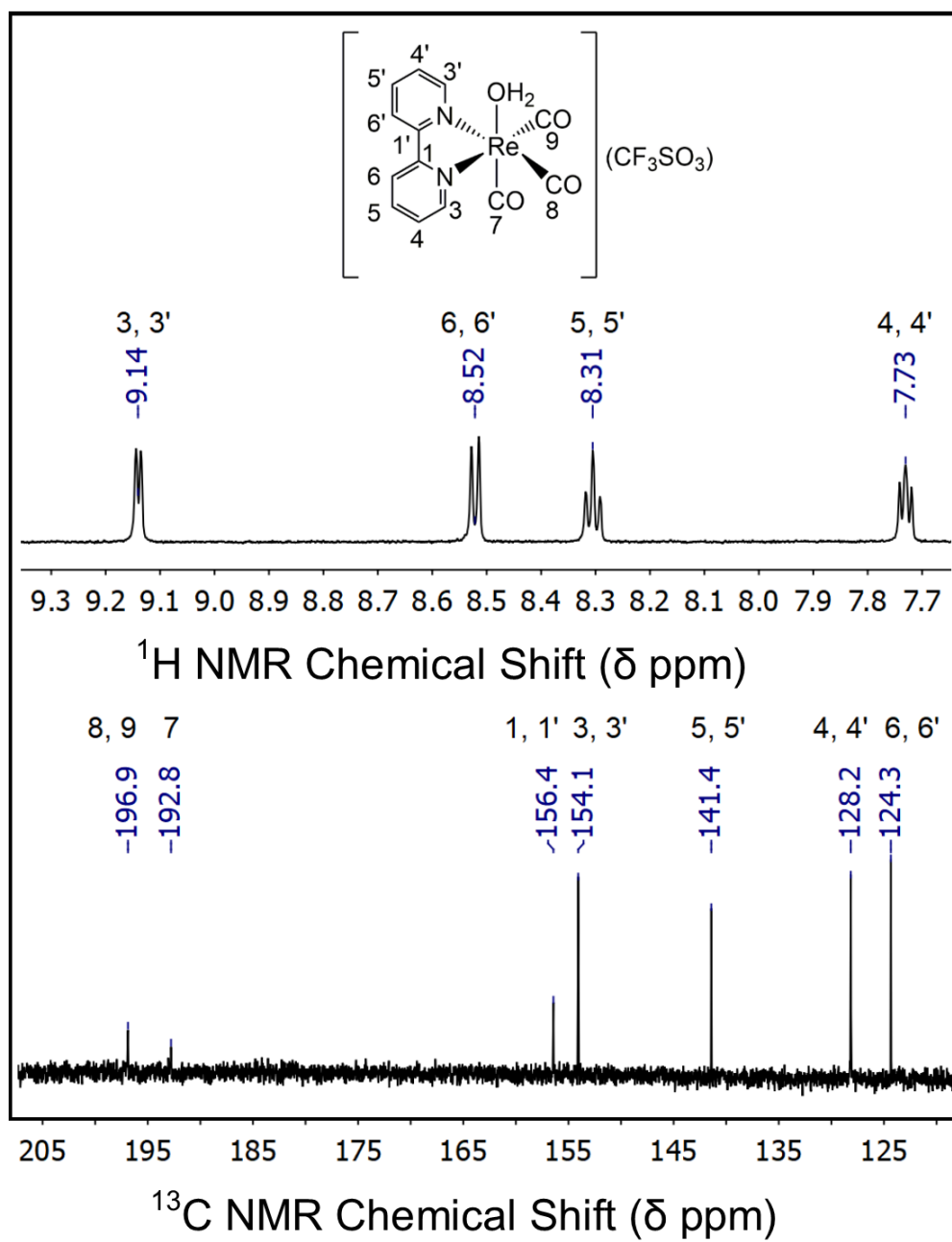


**Figure A2.1** <sup>1</sup>H and <sup>13</sup>C NMR of *fac*-[Re(CO)<sub>3</sub>(bpy)(H<sub>2</sub>O)](CF<sub>3</sub>SO<sub>3</sub>) (1) in D<sub>2</sub>O

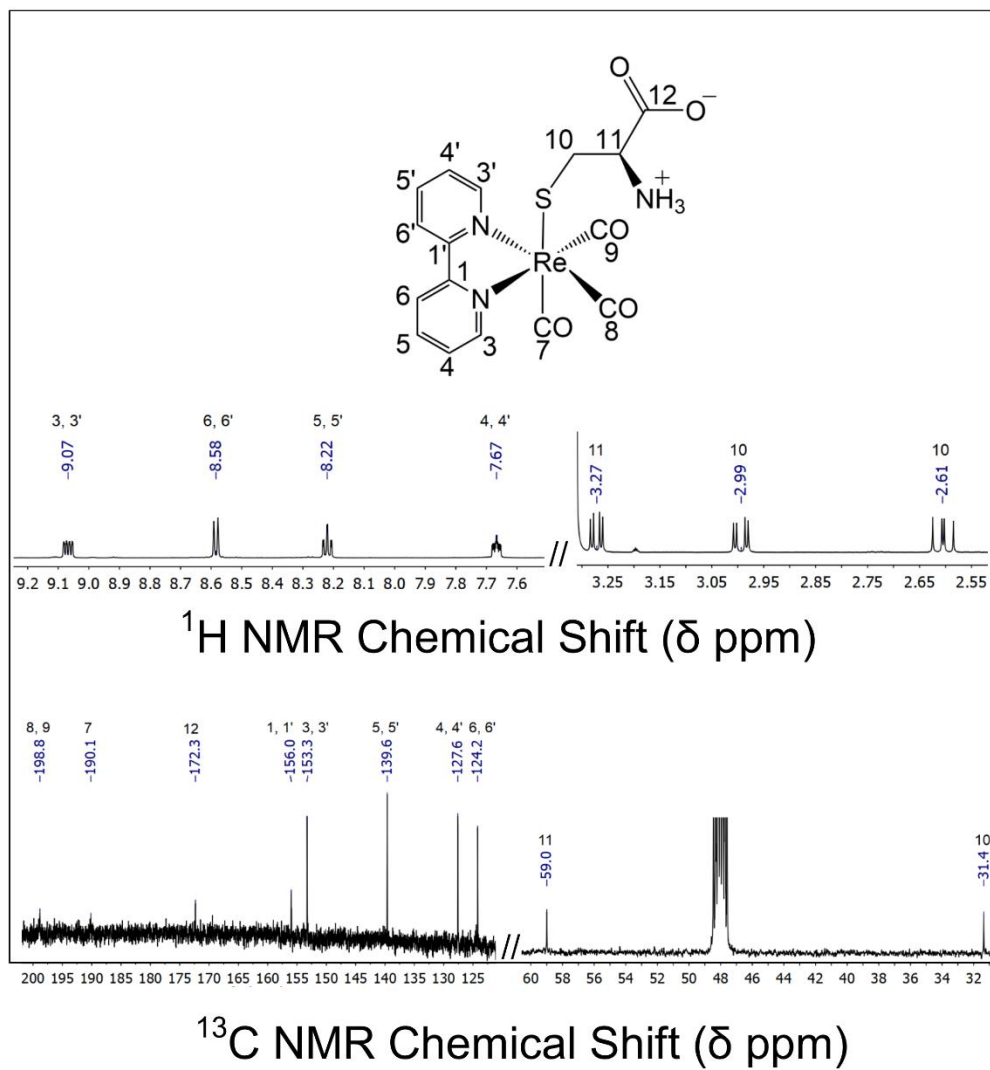


**Figure A2.2**  $^1\text{H}$  and  $^{13}\text{C}$  NMR of *fac*-[Re(CO)<sub>3</sub>(bpy)(HCys)].0.5H<sub>2</sub>O (**2**) in CD<sub>3</sub>OD.

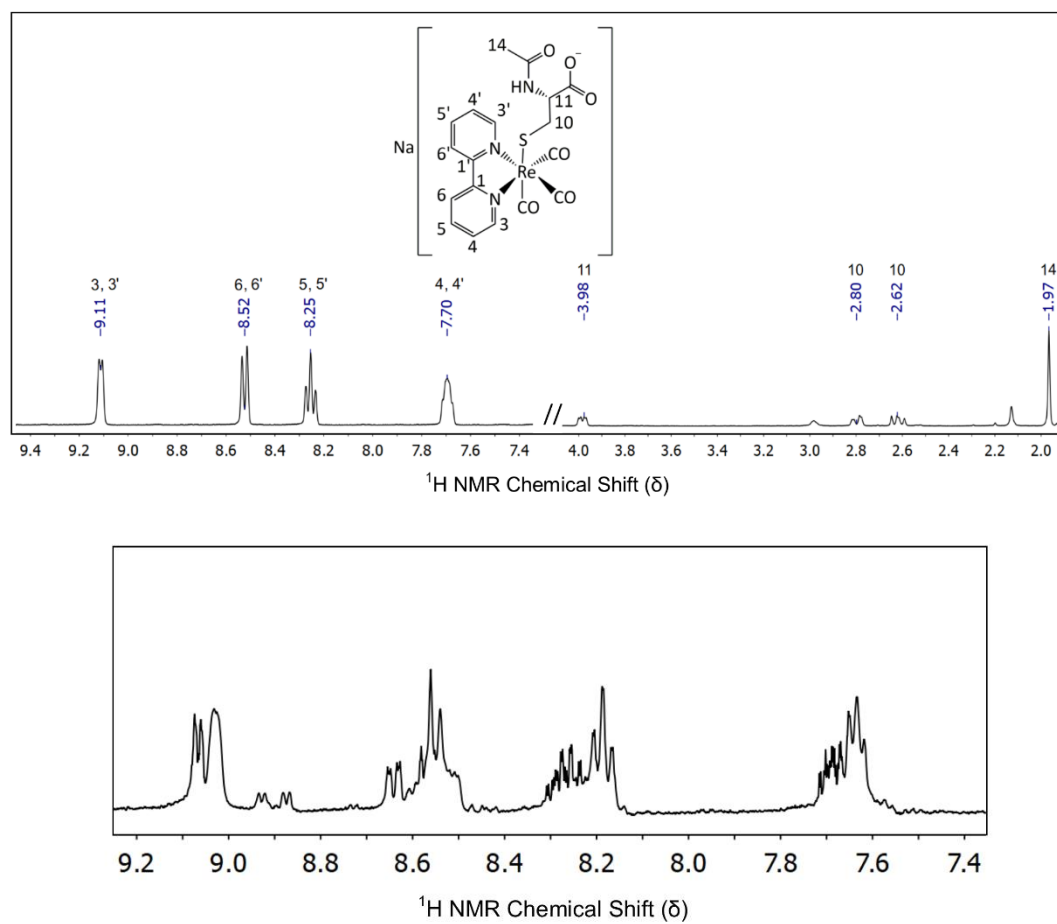


**Figure A2.3**  $^1\text{H}$  NMR spectrum of  $\text{Na}(\text{fac}[\text{Re}(\text{CO})_3(\text{bpy})(\text{NAC})])$  (3) in  $\text{D}_2\text{O}$  (top) and  $\text{CD}_3\text{OD}$  (bottom).

## FT-IR Spectroscopy

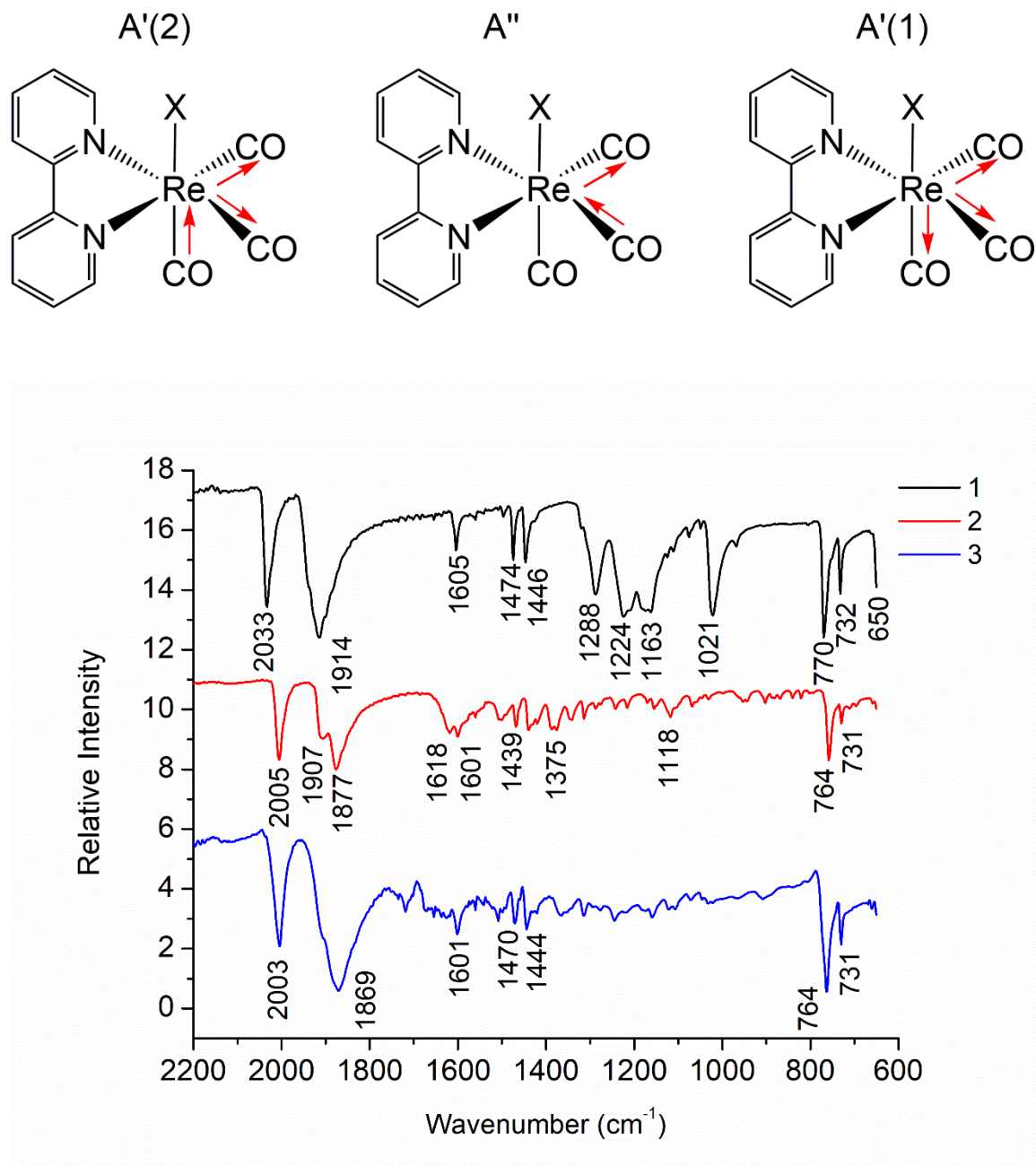


**Figure A2.4** FT-IR spectra of **1**, **2** and **3** and corresponding  $\nu(\text{CO})$  vibrations.

## Thermogravimetric Analysis

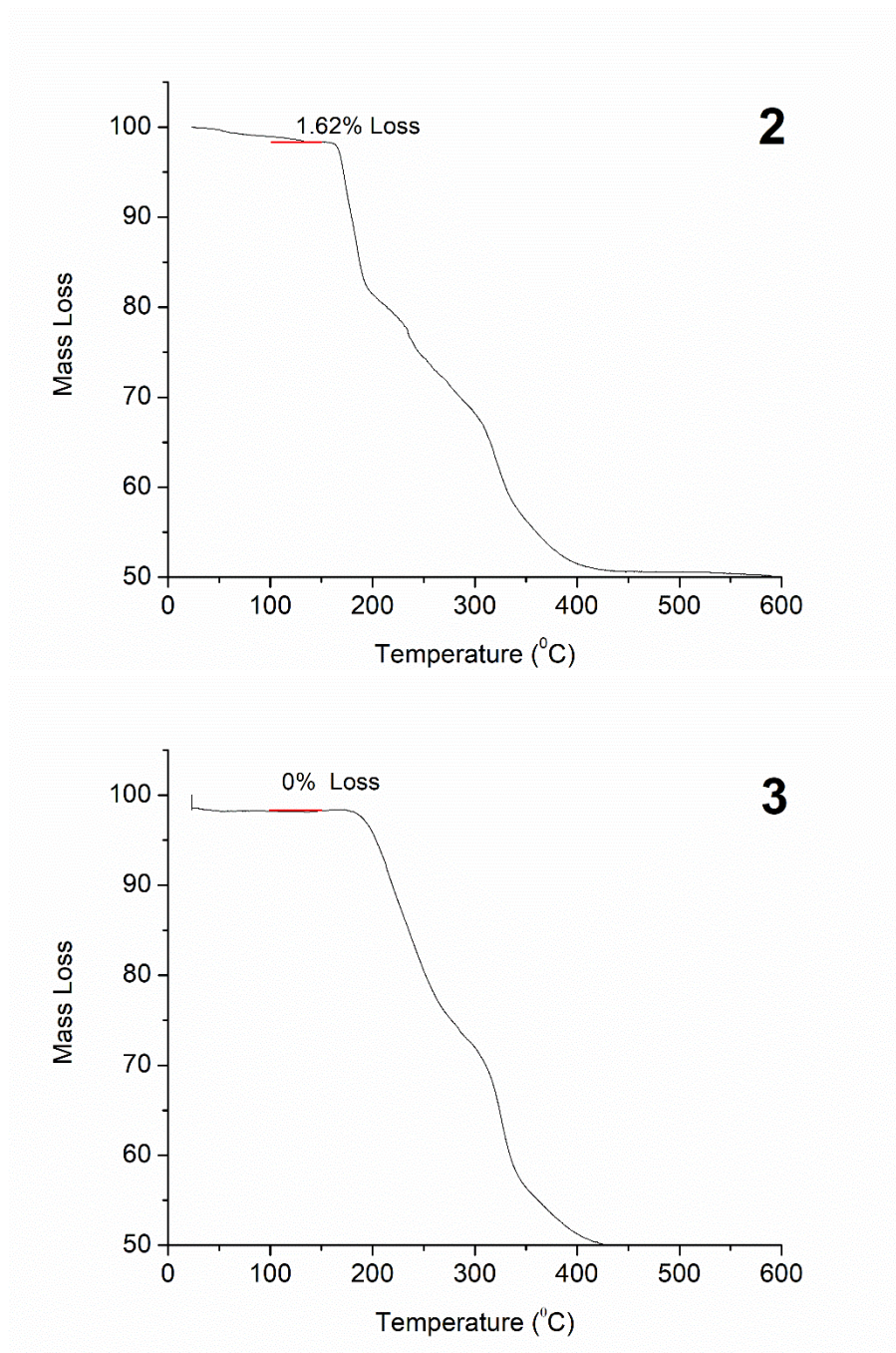


**Figure A2.5** Thermogravimetric analysis of **2** and **3**.

## Electrospray Ionization Mass-Spectrometry (ESI-MS)

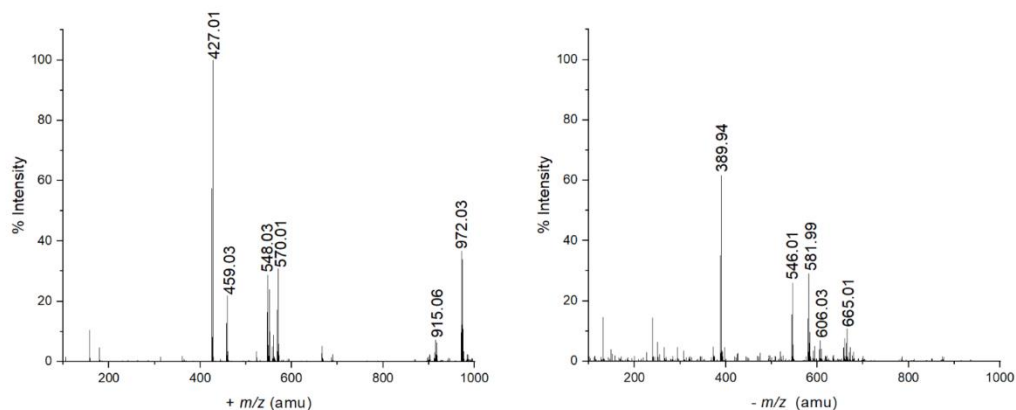


**Figure A2.6** ESI-mass spectra of **2** in MeOH (left) + ion mode, (right) – ion mode. Peak assignments can be found in Table A2.1.

**Table A2.1** Assignments of mass ions in the ESI-MS as shown in Figure A2.6.

m/z	Assignment	m/z	Assignment
427.01	$[\text{Re}(\text{CO})_3(\text{bpy})]^+$	389.94	$[\text{Re}(\text{CO})_3(\text{Cys})]^-$
459.03	$[\text{Re}(\text{CO})_3(\text{bpy})(\text{CH}_3\text{OH})]^+$	546.01	$[\text{Re}(\text{bpy})(\text{CO})_3(\text{Cys})]^-$
548.03	$[\text{Re}(\text{bpy})(\text{CO})_3(\text{HCys}) + \text{H}^+]^+$	581.99	$[\text{Re}(\text{bpy})(\text{CO})_3(\text{HCys})(\text{Cl}^-)]^-$
570.01	$[\text{Re}(\text{bpy})(\text{CO})_3(\text{HCys}) + \text{Na}^+]^+$	606.03	$[\text{Re}(\text{bpy})(\text{CO})_3(\text{HCys})(\text{OAc})]^-$
915.06	$[(\text{Re}(\text{bpy})(\text{CO})_3)_2(\text{CH}_3\text{OH})(\text{CH}_3\text{O})]^+$	660.01	$[\text{Re}(\text{bpy})(\text{CO})_3(\text{HCys})(\text{NaOAc})(\text{CH}_3\text{O})]^-$
972.03	$[\text{Re}(\text{bpy})(\text{CO})_3(\text{HCys}) + \text{Re}(\text{bpy})(\text{CO})_3]^+$		

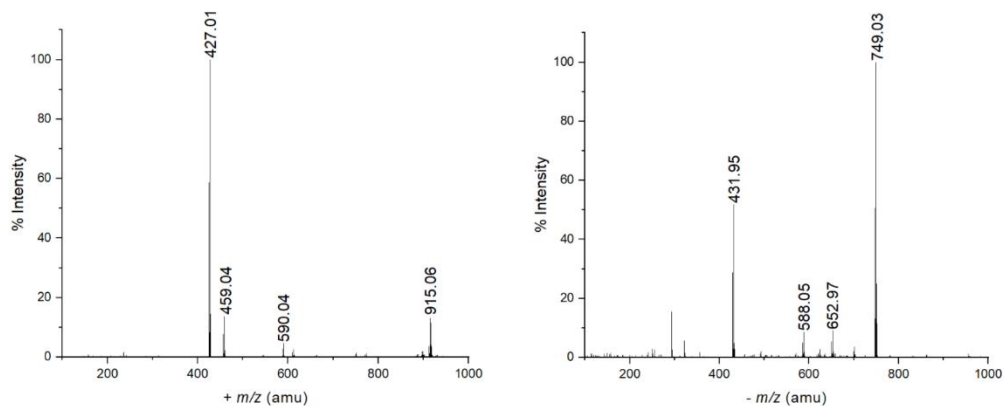


**Figure A2.7** ESI-mass spectra of **3** in MeOH (left) + ion mode, (right) – ion mode. Peak assignments can be found in Table A2.2.

**Table A2.2** Assignment of mass ions of ESI-MS as shown in Figure A2.7.

m/z	Assignment	m/z	Assignment
427.01	$[\text{Re}(\text{bpy})(\text{CO})_3]^+$	431.95	$[\text{ReCO})_3(\text{NAC})]^-$
459.04	$[\text{Re}(\text{CO})_3(\text{bpy})(\text{CH}_3\text{OH})]^+$	588.02	$[\text{ReCO})_3(\text{bpy})(\text{NAC})]^-$
590.04	$[\text{Re}(\text{bpy})(\text{CO})_3(\text{NAC}) + 2\text{H}^+]^+$	652.97	$[\text{ReCO})_3(\text{bpy})(\text{NAC})(\text{CH}_3\text{OH})_2]^-$
915.06	$[(\text{Re}(\text{bpy})(\text{CO})_3)_2(\text{CH}_3\text{OH})(\text{CH}_3\text{O})]^+$	749.03	$[\text{ReCO})_3(\text{bpy})(\text{NAC-NAC})]^-$



## Crystal Data

**Table A2.3** Crystal Data and Structure Refinement for Complex **2** + 1.75 H<sub>2</sub>O.<sup>a</sup>

{ <i>fac</i> }-[(CO) <sub>3</sub> Re(bpy)(HCys)]}4.9H <sub>2</sub> O ( <b>2</b> + 1.75 H <sub>2</sub> O)	
Chemical formula	C <sub>64</sub> H <sub>74</sub> N <sub>12</sub> O <sub>29</sub> Re <sub>4</sub> S <sub>4</sub>
Formula weight (g mol <sup>-1</sup> )	2348.39
Crystal system	Monoclinic
Space group	P21
<i>a</i> (Å)	7.5927(3)
<i>b</i> (Å)	8.2828(2)
<i>c</i> (Å)	32.1679(13)
α (deg)	90
β (deg)	96.531(3)
γ (deg)	90
<i>V</i> (Å <sup>3</sup> )	2009.87(12)
<i>Z</i>	1
<i>D</i> <sub>calcd</sub> (g/cm <sup>3</sup> )	1.940
<i>T</i> (K)	173.0
λ (Å)	1.54178 (Cu K <sub>α</sub> )
(μ / mm <sup>-1</sup> )	13.204
<i>F</i> (000)	1138.0
2θ range for data collection (deg)	2.764 – 145.1
<i>R</i> <sub>1</sub> , <i>wR</i> <sub>2</sub> [ <i>I</i> ≥ 2σ( <i>I</i> )]	0.0700, 0.1631

$$^a R_1 = \sum \|F_0 - F_c\| / \sum |F_0| ; wR_2 = [\sum w(F_0^2 - F_c^2)^2 / [\sum w(F_0^2)^2]]^{1/2}$$

**Table A2.4.** Selected Bond Lengths (Å) and Angles (deg) for Complex **2** + 1.75 H<sub>2</sub>O.

Bond	Distance (Å)
Re(1)-S(1)	2.503(6)
Re(1)-N(1)	2.11(2)
Re(1)-N(2)	2.15(2)
Re(1)-C(11)	1.91(2)
Re(1)-C(12)	1.92(2)
Re(1)-C(13)	1.91(2)
C(11)-O(1)	1.16(2)
C(12)-O(2)	1.13(3)
C(13)-O(3)	1.15(3)
Re(2)-S(2)	2.50(1)
Re(2)-N(4)	2.13(2)
Re(2)-N(5)	2.18(2)
Re(2)-C(27)	1.88(2)
Re(2)-C(28)	1.87(3)
Re(2)-C(29)	1.90(4)
C(27)-O(6)	1.15(3)
C(28)-O(7)	1.20(4)
C(29)-O(8)	1.16(4)

Bond angle	Degree
N(1)-Re(1)-N(2)	74.5(7)
N(1)-Re(1)-S(1)	87.9(5)
N(1)-Re(1)-C(11)	95.2(8)
N(1)-Re(1)-C(13)	97.9(9)
C(12)-Re(1)-C(13)	90.9(10)
N(4)-Re(2)-N(5)	74.4(8)
N(4)-Re(2)-S(2)	89.0(6)
N(4)-Re(2)-C(27)	91.7(10)
N(4)-Re(2)-C(28)	99.8(12)
C(28)-Re(2)-C(29)	89.4(15)

## UV-Visible Absorbance Spectroscopy

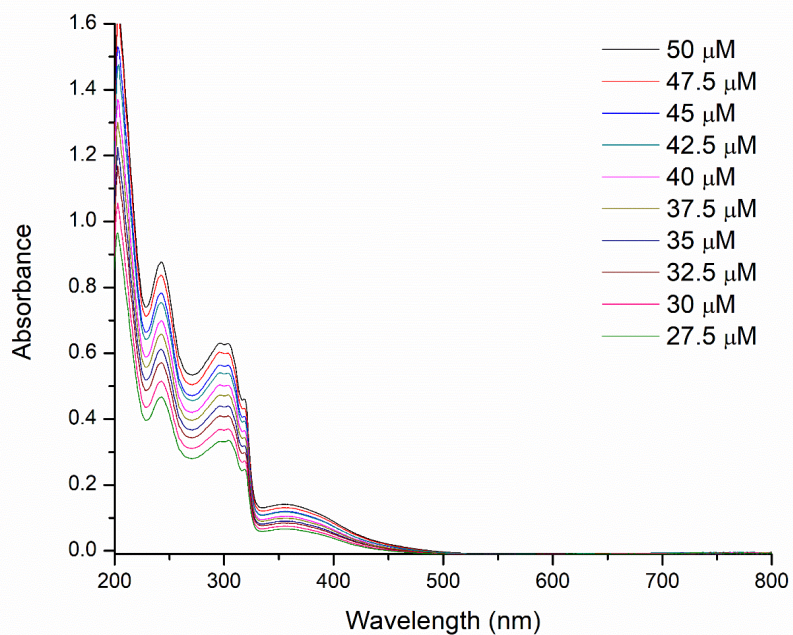


**Figure A2.8** UV-visible absorbance spectrum of **1** in MeOH. Assignment of bands and epsilon ( $\epsilon$ ) values shown in Table A2.5.

**Table A2.5** Assignment of bands and epsilon ( $\epsilon$ ) values of UV-visible absorbance spectra as shown in Figure A2.8.

Wavelength (nm)	$\epsilon$ ( $\text{M}^{-1} \text{cm}^{-1}$ )
243	18,000
293	13,200
303	13,000
317	9,350
358	3,250

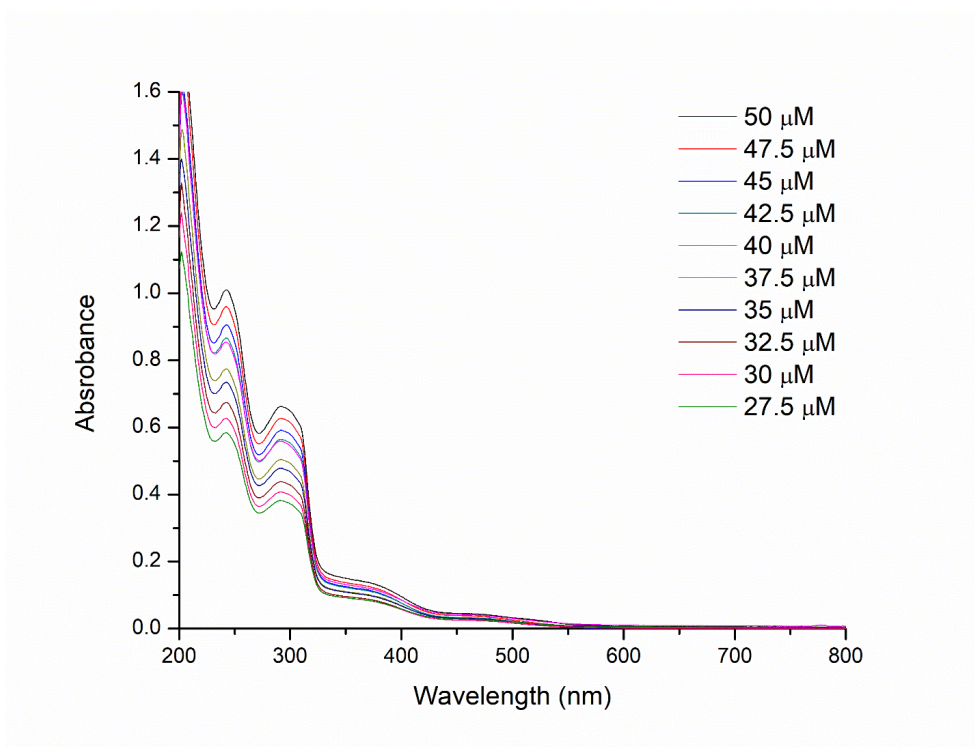


**Figure A2.9** UV-visible absorbance spectrum of **2** in MeOH. Assignment of bands and epsilon ( $\epsilon$ ) values shown in Table A2.6.

**Table A2.6** Assignment of bands and epsilon ( $\epsilon$ ) values of UV-visible absorbance spectra as shown in Figure A2.9.

Wavelength (nm)	$\epsilon$ ( $\text{M}^{-1} \text{cm}^{-1}$ )
243	18,900
291	12,500
370	2,260
475	500

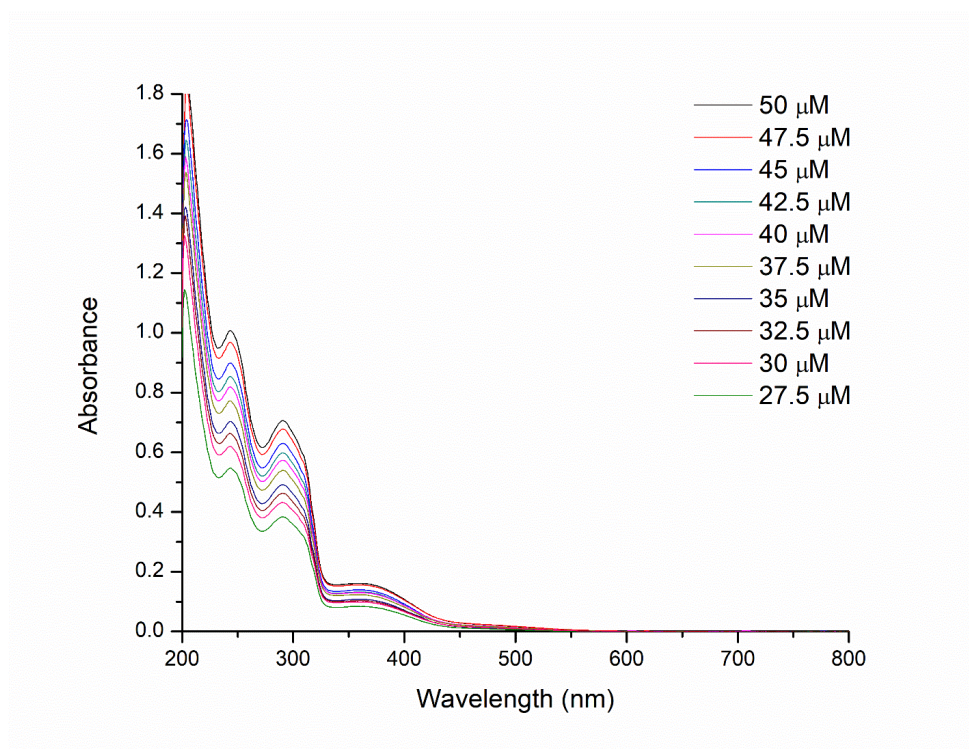


**Figure A2.10** UV-visible absorbance spectroscopy of **3** in MeOH. Assignment of bands and epsilon ( $\epsilon$ ) values shown in Table A2.7.

**Table A2.7** Assignment of bands and epsilon ( $\epsilon$ ) values of UV-visible absorbance spectra as shown in Figure A2.10.

Wavelength (nm)	$\epsilon$ ( $\text{M}^{-1} \text{cm}^{-1}$ )
244	20,000
290	14,100
360	3,300
483	550

## *Singlet Oxygen*

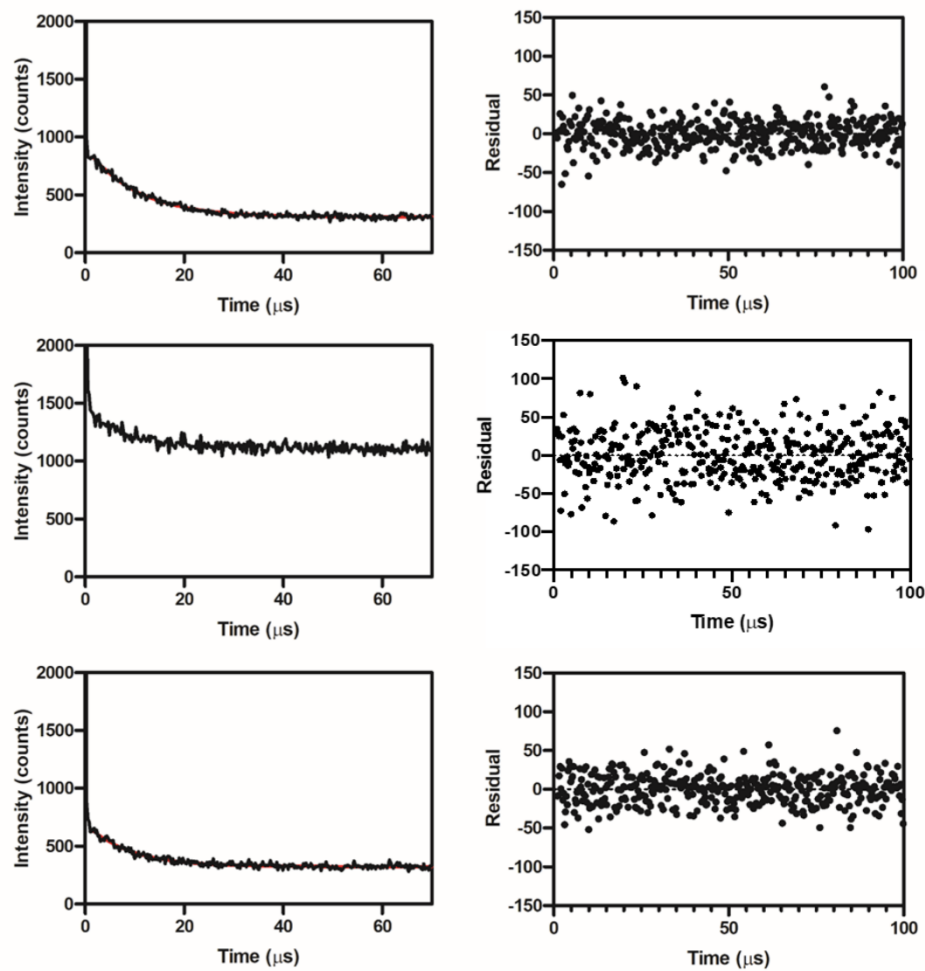


**Figure A2.11** Time-resolved decay curves probed at maximum wavelength after 355 nm laser excitation in an MeOH solution at 298 K of **1** (top), **2** (middle) and **3** (bottom).

## UV Irradiation and CO Release

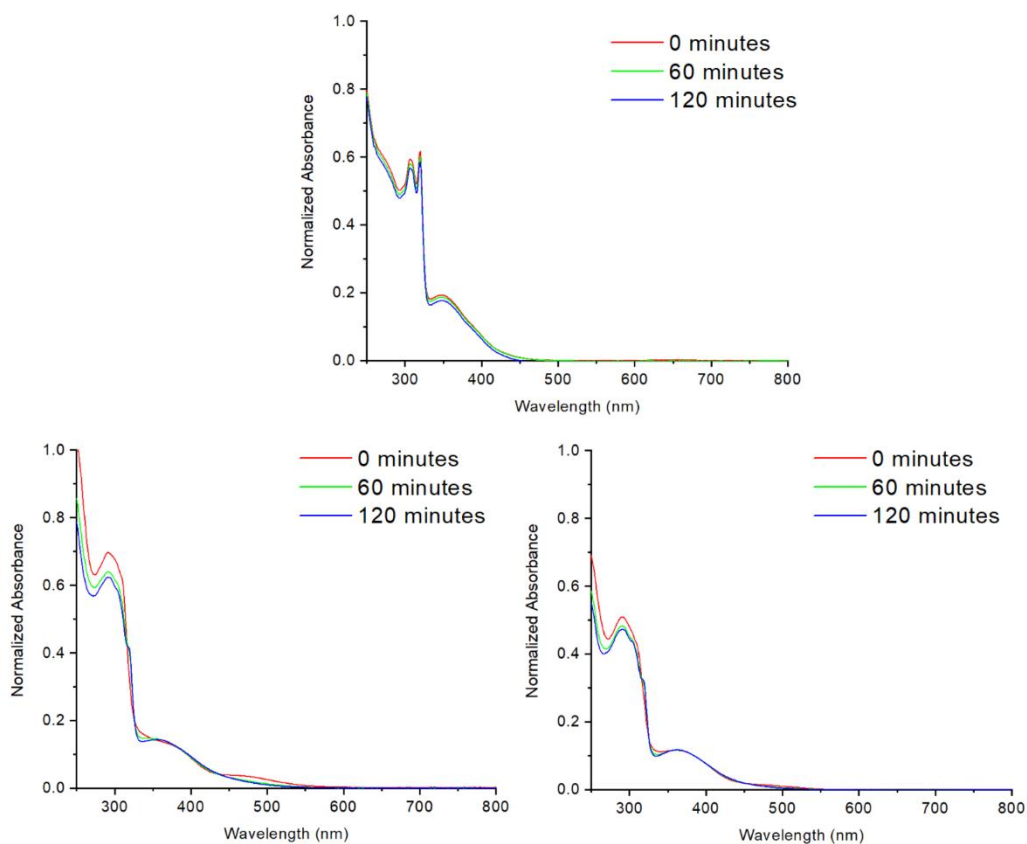


**Figure A2.12** UV-visible absorbance spectra of **1** (top), **2** (left) and **3** (right) at the respective concentration of 25, 12.5 and 20  $\mu\text{M}$  in MeOH when irradiated in a Schlenk cuvette using a UV-A hand lamp (365 nm,  $7.105 \text{ mW}/\text{cm}^{-2}$ ) under Ar over the course of 2hr.

**Table A2.8** CO release measured using gas chromatography with thermal conductivity detector (GC-TCD) of **1** (top), **2** (middle) and **3** (bottom). 50  $\mu$ M concentrations of each complex in MeOH were irradiated in a Schlenk cuvette using a UVA hand lamp (365 nm, 7.105 mW/cm<sup>2</sup>) under Ar.

Time (minutes)	CO GC Peak Area	CO (mole%)
20	1.3	0
40	2.2	0
60	11	0
80	4.5	0
100	13.5	0
120	4.2	0

Time (minutes)	CO GC Peak Area	CO (mole%)
20	-	-
40	1.8	0
60	2.1	0
80	-	-
100	2.1	0
120	1.9	0

Time (minutes)	CO GC Peak Area	CO (mole%)
20	2.2	0
40	2.3	0
60	3.3	0
80	4.3	0
100	3.2	0
120	5.1	0



### *Lipophilicity and partition coefficient (log P)*

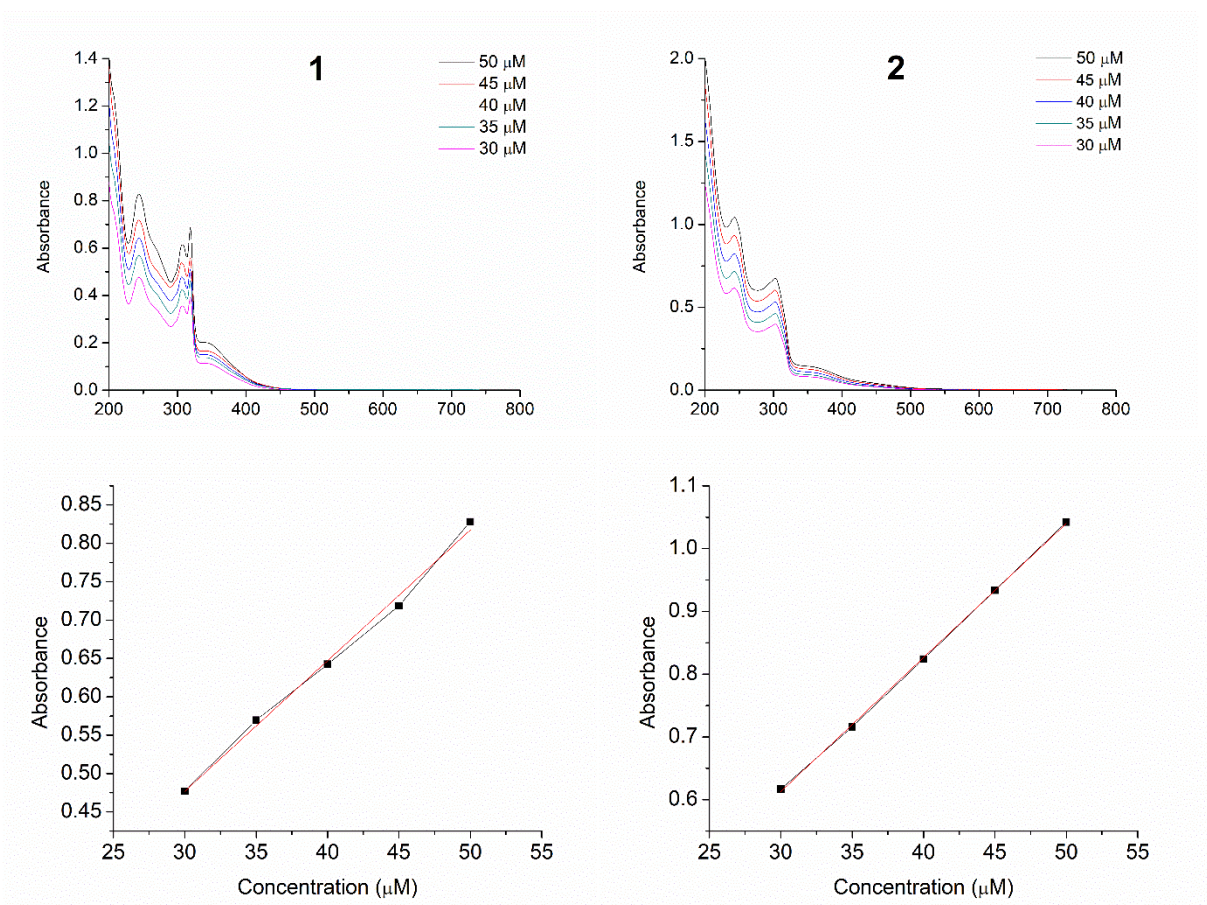
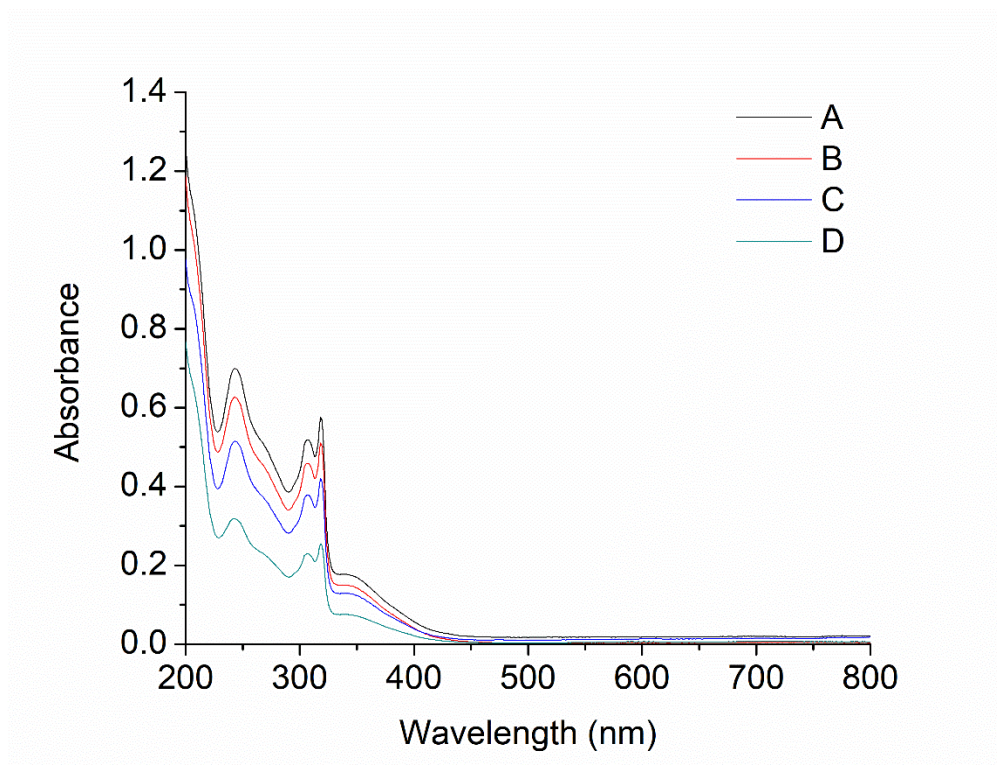


**Figure A2.13** UV-visible absorbance spectra of **1** in  $\text{H}_2\text{O}$  and **2** in aqueous EtOH to obtain a calibration curve. Assignment of epsilon ( $\epsilon$ ) values at 243 nm shown in Table A2.9.

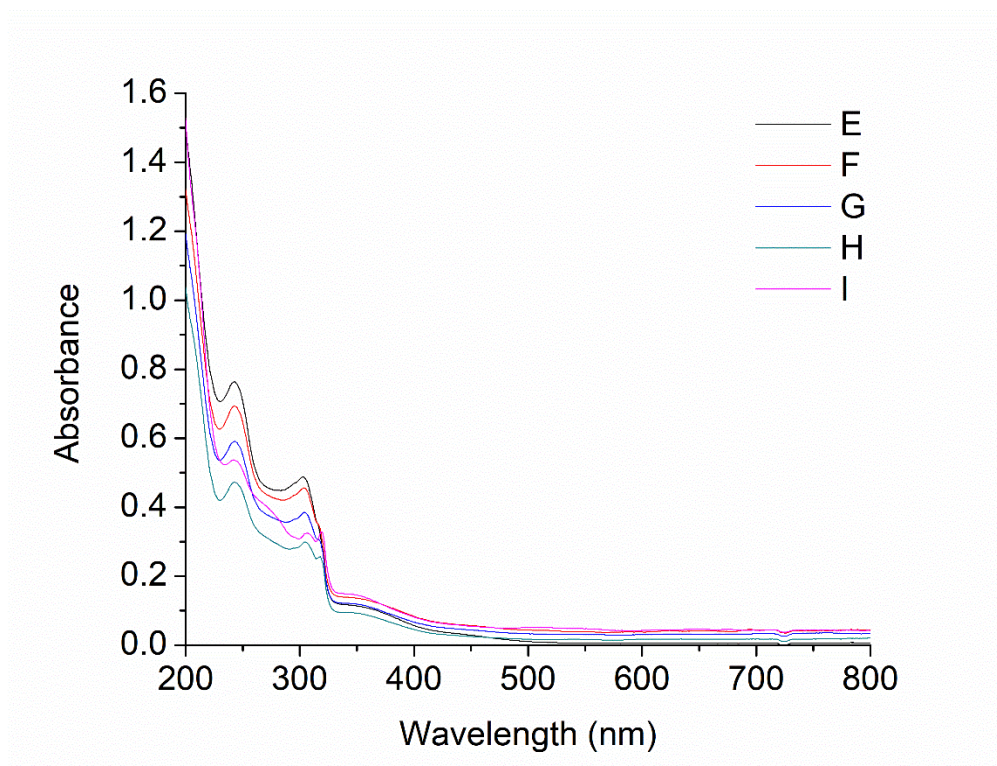
**Table A2.9** Assignment of bands and epsilon ( $\epsilon$ ) values of UV-visible absorbance spectra as shown in Figure A2.13.

Complex	$\epsilon$ ( $\text{M}^{-1} \text{cm}^{-1}$ )
<b>1</b>	17,000
<b>2</b>	21,400



Sample	Initial amount of <b>1</b> ( $\mu\text{mol}$ )	Water (mL)	n-Octanol (mL)
A	1.25	25	25
B	1	20	30
C	0.75	15	35
D	0.5	10	40

**Figure A2.14** UV-visible absorbance spectra of **1** in aqueous phase of the above solutions A - D (water/ n-octanol mixtures) obtained after shaking for 24 hr at 25 C.



Sample	Initial amount of <b>2</b> ( $\mu\text{mol}$ )	Water (mL)	n-Octanol (mL)
E	1.25	25	25
F	1	20	30
G	0.75	15	35
H	0.5	10	40
I	0.25	5	45

**Figure A2.15** UV-visible absorbance spectra of **2** in aqueous phase of the above solutions E - I (water + 1.5% EtOH/ n-octanol mixtures) obtained after shaking for 24 hr at 25 C.

*Synchrotron-Based X-ray Fluorescence Microscopy (XFM)*

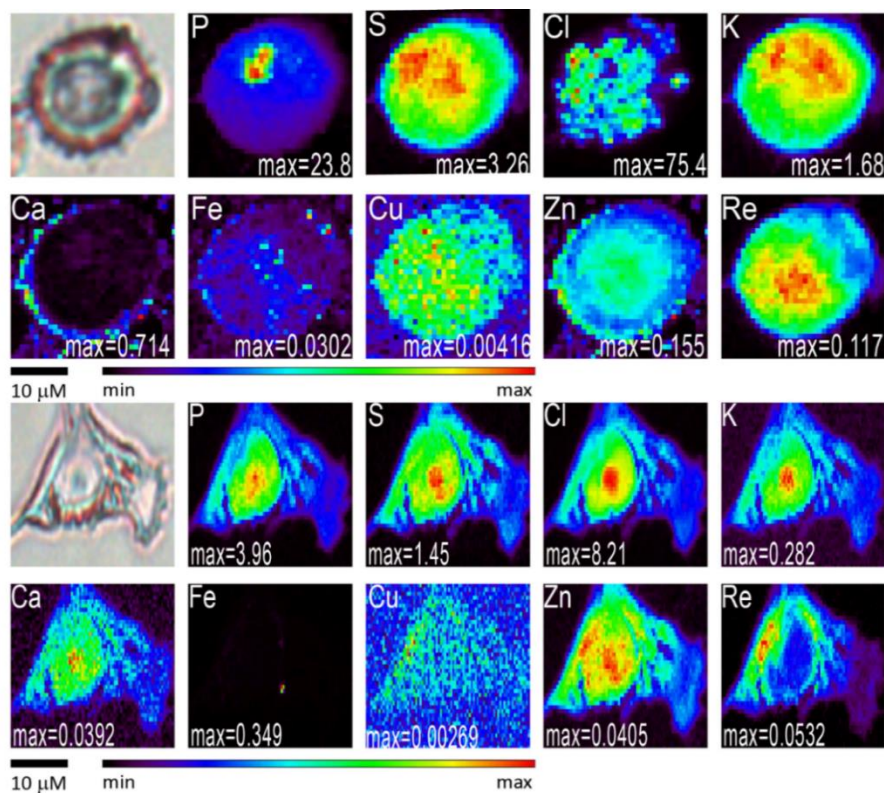


**Figure A2.16** Optical micrographs (top left) and scattered X-ray (XS) and XRF elemental distribution map of MDA-MB-231 cells treated with **1** for 6 h. The maximum elemental area densities (quantified from standards and expressed in  $\mu\text{g cm}^{-2}$ ) are given in the bottom of each map. The scale bar represents 10  $\mu\text{m}$  unless otherwise indicated.



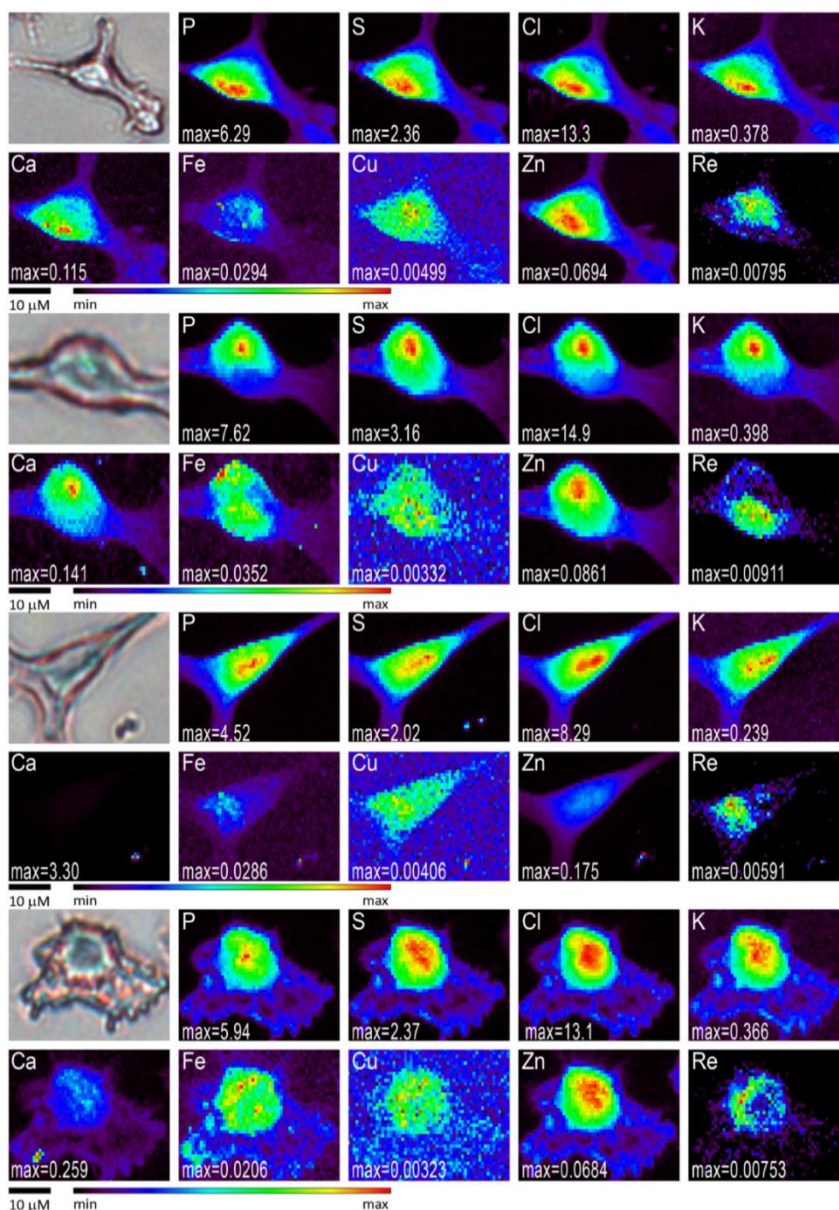


**Figure A2.17** Optical micrographs (top left) and scattered X-ray (XS) and XRF elemental distribution map of MDA-MB-231 cells treated with **2** for 6 h. The maximum elemental area densities (quantified from standards and expressed in  $\mu\text{g cm}^{-2}$ ) are given in the bottom of each map. The scale bar represents 10  $\mu\text{m}$  unless otherwise indicated.

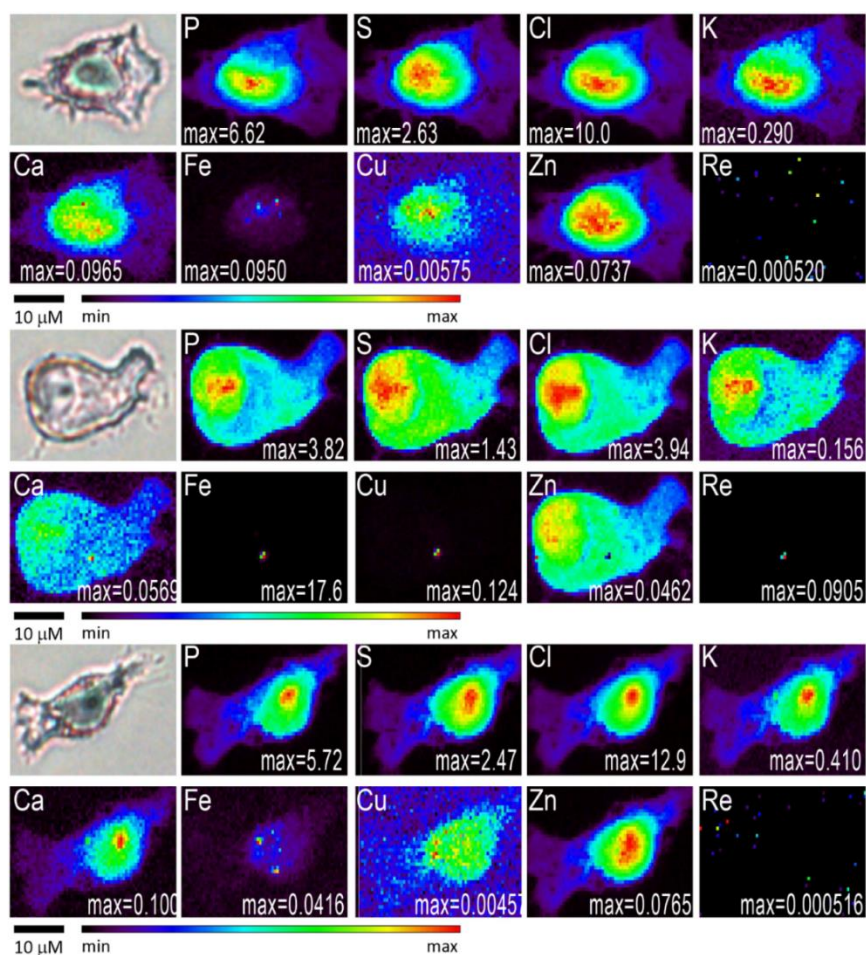


**Figure A2.18** Optical micrographs (top left) and scattered X-ray (XS) and XRF elemental distribution map of MDA-MB-231 cells treated with DMEM for 6 h. The maximum elemental area densities (quantified from standards and expressed in  $\mu\text{g cm}^{-2}$ ) are given in the bottom of each map. The scale bar represents 10  $\mu\text{m}$  unless otherwise indicated.

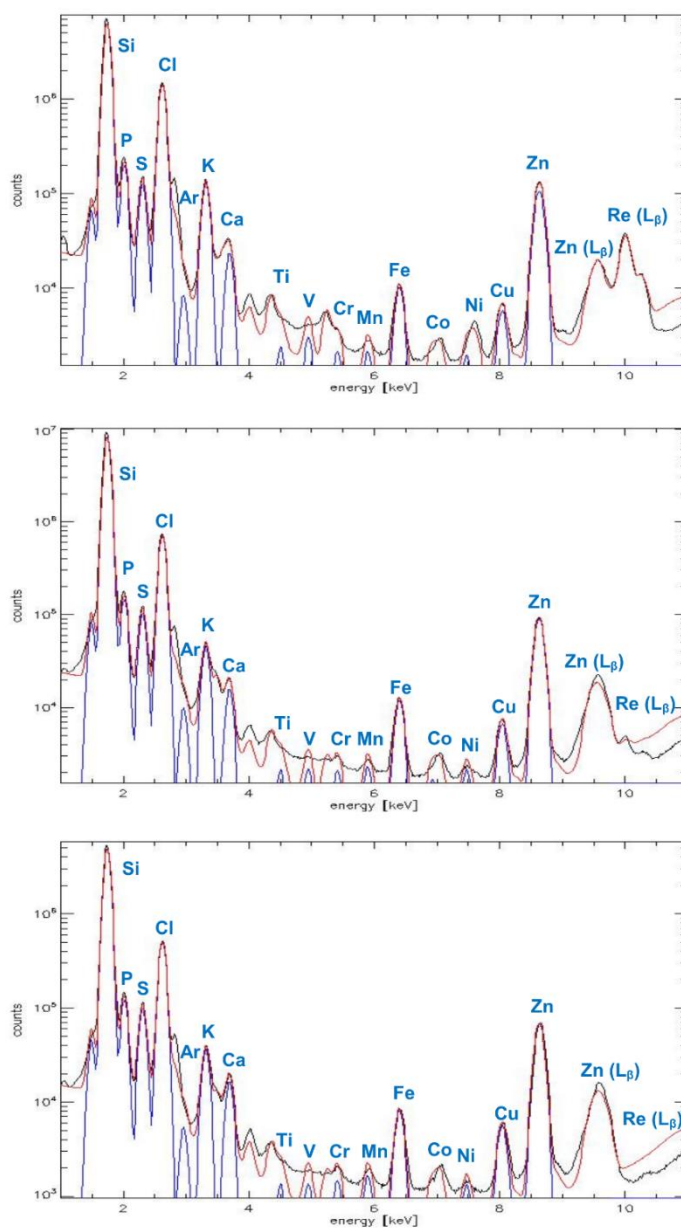


**Figure A2.19** XFM spectra (black) of MDA-MB-231 sample cells treated for 6 hr with 20  $\mu$ M solutions of **1** (top) and **2** (middle) or in DMEM (bottom). Each figure shows the fit to the spectrum (red) and the contribution of the K $\alpha$  peaks used in the fitting (blue) with their corresponding labelling.

## Chapter 3: Supporting Information

### *Physical Measurements and Methods*

#### *NMR Spectroscopy*

$^1\text{H}$  and  $^{13}\text{C}$ -NMR spectroscopy measurements were carried out at room temperature using a Bruker AVIII-600 CFI-600 spectrometer using  $\text{D}_2\text{O}$  as a solvent.  $^1\text{H}$  NMR were internally referenced using the HOD/ $\text{H}_2\text{O}$  peak at 4.80 ppm with a total of 64 scans being coadded.<sup>152</sup> Using the UDEFT pulse sequence and broadband proton decoupling at 151 MHz,  $^{13}\text{C}$  NMR spectra were recorded.  $^{13}\text{C}$  NMR spectra were externally calibrated using  $\text{CH}_3\text{OH}$  in  $\text{D}_2\text{O}$ , resonating at 49.15 ppm with a total of 4000 scans being coadded.<sup>153</sup> A  $30^\circ$  pulse, 26.2 kHz sweep width, 1-s delay between scans, and 65 K data points were used.

#### *FT-IR Spectroscopy.*

500 scans were measured using an Agilent Cary 630 FTIR with a diamond ATR accessory.

#### *ESI-Mass spectrometry.*

Electrospray ionization (ESI) mass spectra were collected both in positive (+) and  $\text{H}_2\text{O}$  were injected and mobilized using an injection flow rate of 0.2 mL/min. The source was held at  $200^\circ\text{C}$  with a drying gas flow rate of 7 L/min and a nebulizer pressure of 12 p.s.i. The fragmentor, capillary, and skimmer voltages were set to 80, 4000 and 65 V, respectively. Peak assignments were confirmed using a high-resolution Isotope Distribution Calculator from Scientific Instrument Services.<sup>154</sup>



### ***Thermogravimetric Analysis.***

Using a Netzsch STA 409 PC Luxx instrument thermogravimetric analysis was performed. The analyses were run from room temperature to 450 °C using a ramp rate of 2 °C min<sup>-1</sup> under a flow of N<sub>2</sub>.

## NMR Spectroscopy

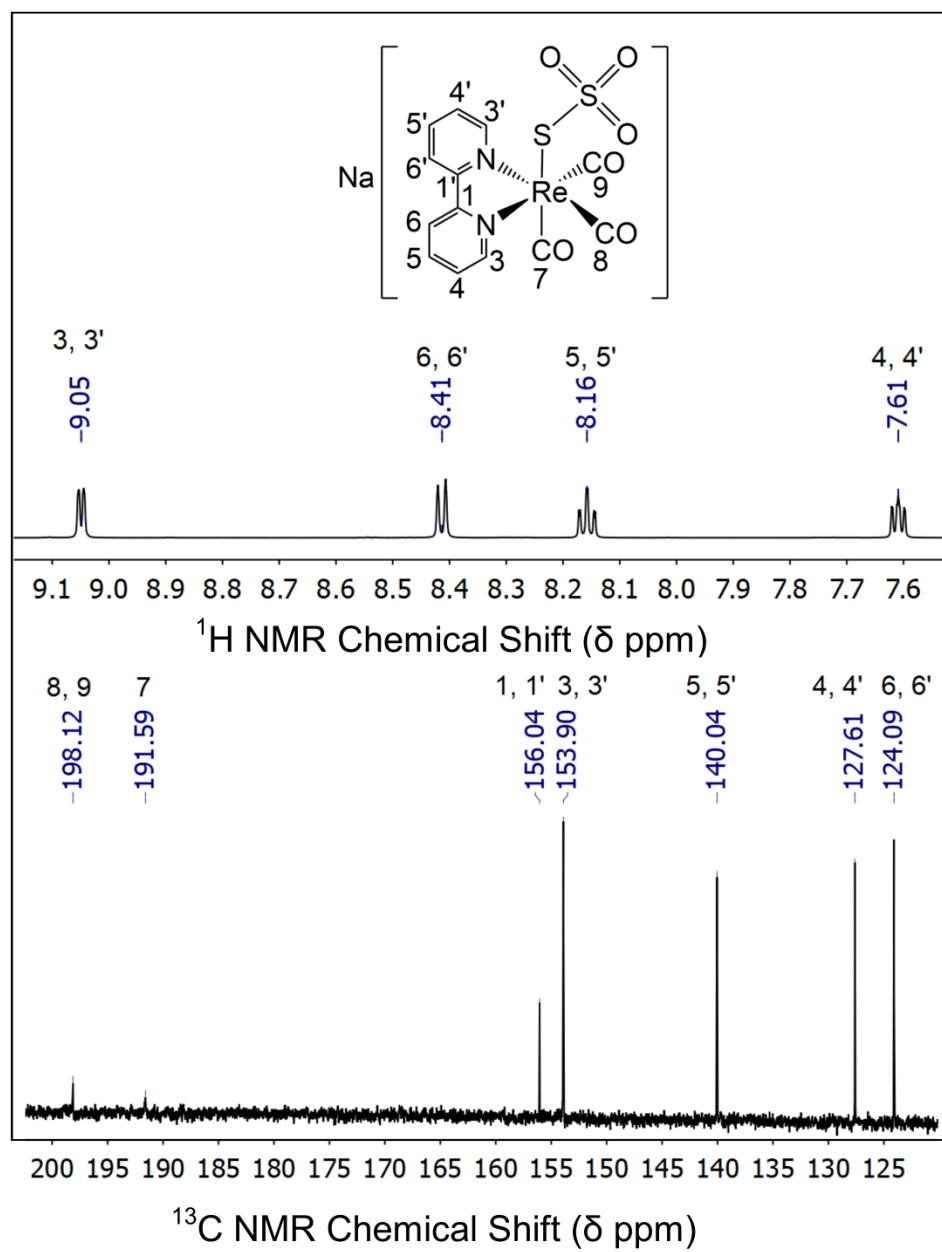


**Figure A3.1**  $^1\text{H}$  NMR and  $^{13}\text{C}$  NMR spectra of  $\text{Na}(\text{fac-}[\text{Re}(\text{CO})_3(\text{bpy})(\text{S}_2\text{O}_3)]). \text{H}_2\text{O}$  (**4**) in  $\text{D}_2\text{O}$ .

## FT-IR Spectroscopy

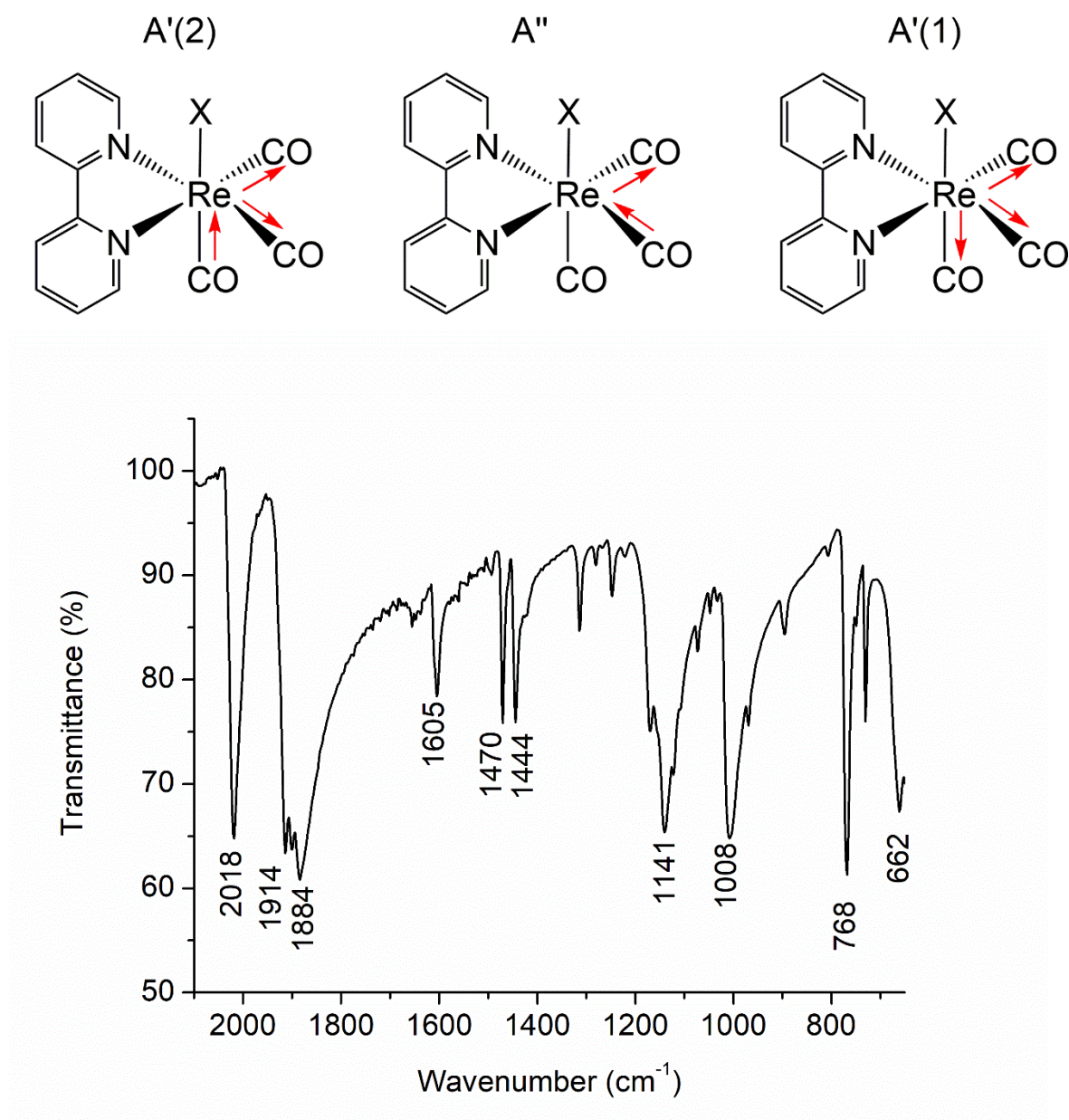


**Figure A3.2** FT-IR spectrum of **4** and corresponding  $\nu(\text{CO})$  vibrations.

*Thermogravimetric Analysis (TGA)*

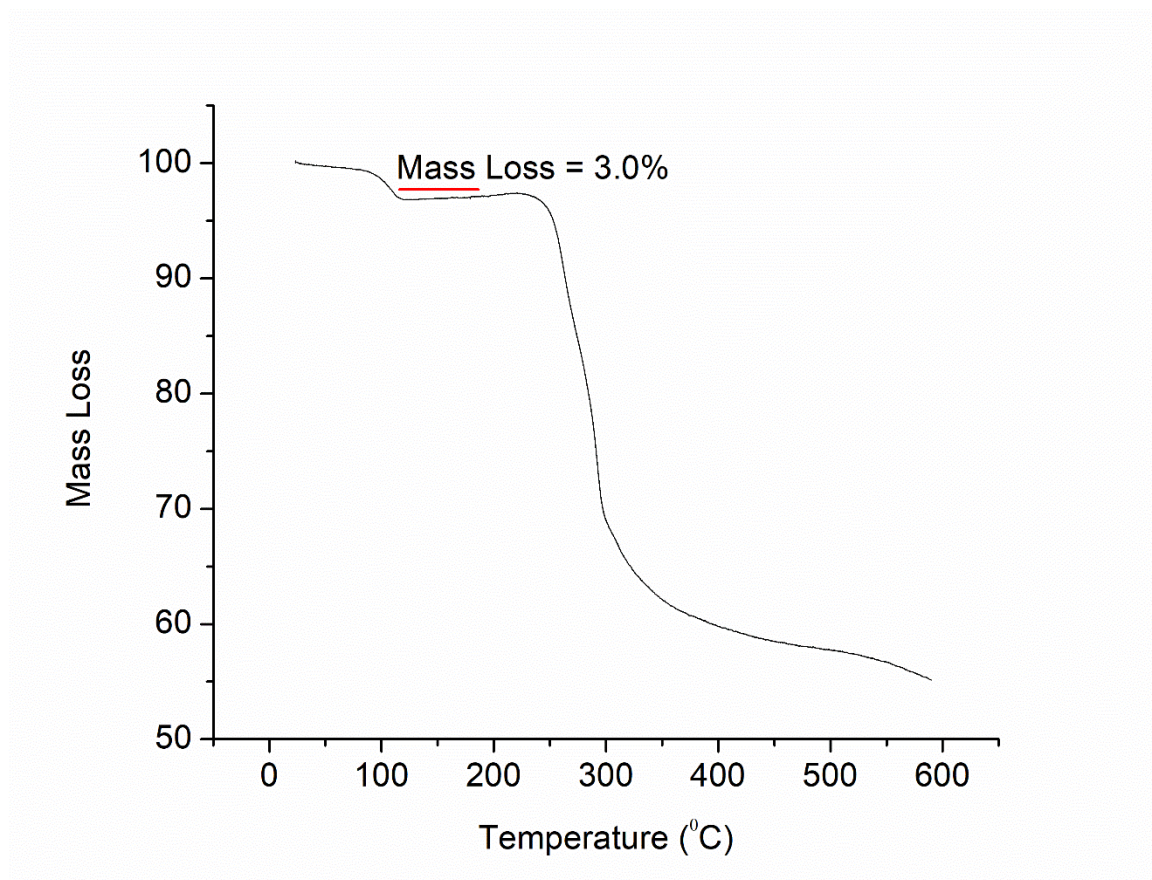


**Figure A3.3** Thermogravimetric analysis (TGA) of **4**.

## Electrospray Ionization Mass-Spectrometry (ESI-MS)

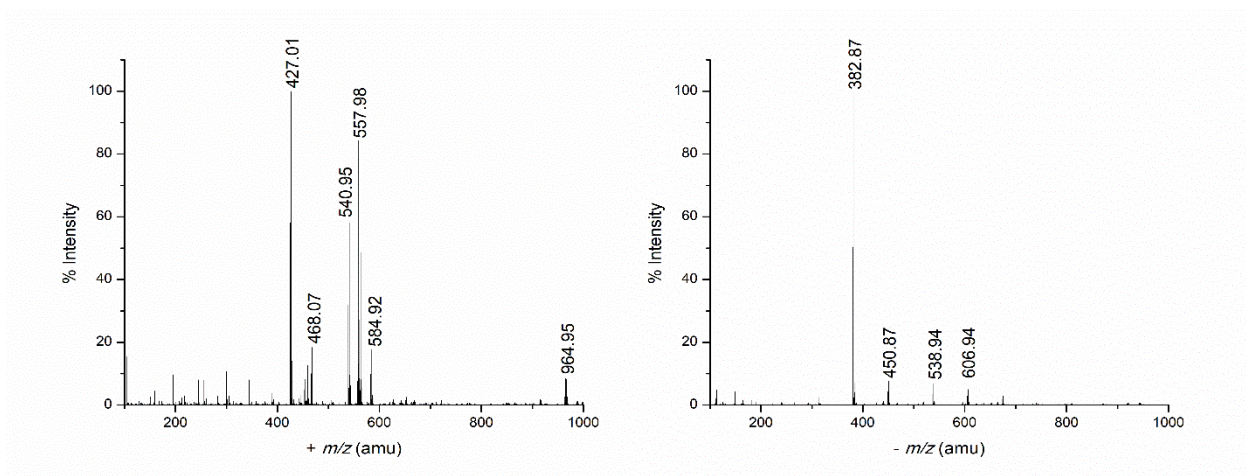


**Figure A3.4** ESI-mass spectra of **4** in H<sub>2</sub>O (left) + ion mode, (right) – ion mode. Peak assignments can be found in Table A3.1.

**Table A3.1** Assignments of mass ions in the ESI-mass spectra as shown in Figure A3.4.

m/z	Assignment	m/z	Assignment
427.01	$[\text{Re}(\text{CO})_3(\text{bpy})]^+$	382.87	$[\text{Re}(\text{CO})_3\text{S}_2\text{O}_3]^-$
468.07	$[\text{Re}(\text{CO})_3(\text{bpy})(\text{CH}_3\text{CN})]^+$	450.87	$[\text{Re}(\text{CO})_3\text{S}_2\text{O}_3] + (\text{CH}_3\text{CN}) + (\text{HCN})^-$
540.95	$[\text{Re}(\text{CO})_3(\text{bpy})(\text{S}_2\text{O}_3) + 2\text{H}^+]^+$	538.94	$[\text{Re}(\text{CO})_3(\text{bpy})(\text{S}_2\text{O}_3)]^-$
557.98	$[\text{Re}(\text{CO})_3(\text{bpy})(\text{S}_2\text{O}_3) + \text{NH}_4^+ + \text{H}^+]^+$	606.94	$[\text{Re}(\text{CO})_3(\text{bpy})(\text{S}_2\text{O}_3)(\text{CH}_3\text{CN}) + (\text{HCN})]^-$
584.92	$[\text{Re}(\text{CO})_3(\text{bpy})(\text{S}_2\text{O}_3) + 2\text{Na}^+]^+$		
964.95	$[(\text{Re}(\text{CO})_3(\text{bpy}))_2(\text{S}_2\text{O}_3) + \text{H}^+]^+$		

## Crystal Data

**Table A3.2** Crystal Data and Structure Refinement for Complex **4** + 0.75H<sub>2</sub>O · C<sub>2</sub>H<sub>5</sub>OH.<sup>a</sup>

Empirical formula	C <sub>60</sub> H <sub>70</sub> N <sub>8</sub> Na <sub>4</sub> O <sub>35</sub> Re <sub>4</sub> S <sub>8</sub>
Formula weight	2556.48
Crystal system	monoclinic
Space group	P2 <sub>1</sub> /n
a (Å)	18.1076(4)
b (Å)	18.6534(4)
c (Å)	24.5013(6)
α (deg)	90
β (deg)	92.749(2)
γ (deg)	90
V (Å <sup>3</sup> )	8266.2(3)
Z	4
D <sub>calcd</sub> (g/cm <sup>3</sup> )	2.054
T (K)	173.0
λ (Å)	1.54178 (CuKα)
(μ / mm <sup>-1</sup> )	14.061
F(000)	4952
2θ range for data collection (deg)	5.934 to 140.138
R <sub>1</sub> , wR <sub>2</sub> [I ≥ 2σ(I)]	0.0700, 0.1631

$$^a R_1 = \sum \|F_0 - F_c\| / \sum |F_0| ; wR_2 = [\sum w(F_0^2 - F_c^2)^2 / [\sum w(F_0^2)^2]]^{1/2}$$

**Table A3.3** Selected Bond Lengths (Å) for Complex **4** + 0.75H<sub>2</sub>O · C<sub>2</sub>H<sub>5</sub>OH.

Bond	Distance (Å)	Bond	Distance (Å)
Re(1)-S(1)	2.511(2)	Re(3)-S(5)	2.522(2)
Re(1)-N(1)	2.165(6)	Re(3)-N(5)	2.184(6)
Re(1)-N(2)	2.168(5)	Re(3)-N(6)	2.169(5)
Re(1)-C(11)	1.924(7)	Re(3)-C(37)	1.930(7)
Re(1)-C(12)	1.937(7)	Re(3)-C(38)	1.930(7)
Re(1)-C(13)	1.925(7)	Re(3)-C(39)	1.933(7)
C(11)-O(1)	1.143(9)	C(37)-O(13)	1.135(9)
C(12)-O(2)	1.137(9)	C(38)-O(14)	1.142(9)
C(13)-O(3)	1.145(9)	C(39)-O(15)	1.134(9)
S(1)-S(2)	2.036(3)	S(5)-S(6)	2.023(3)
Re(2)-S(3)	2.512(2)	Re(4)-S(7)	2.525(2)
Re(2)-N(3)	2.186(6)	Re(4)-N(7)	2.176(5)
Re(2)-N(4)	2.158(5)	Re(4)-N(8)	2.175(6)
Re(2)-C(24)	1.935(7)	Re(4)-C(50)	1.921(7)
Re(2)-C(25)	1.932(7)	Re(4)-C(51)	1.928(7)
Re(2)-C(26)	1.913(7)	Re(4)-C(52)	1.906(7)
C(24)-O(7)	1.141(9)	C(50)-O(19)	1.141(9)
C(25)-O(8)	1.138(9)	C(51)-O(20)	1.147(9)
C(26)-O(9)	1.154(9)	C(52)-O(21)	1.906(7)
S(3)-S(4)	2.030(3)	S(7)-S(8)	2.033(3)

**Table A3.4** Selected Bond Angles (deg) for Complex **4** + 0.75H<sub>2</sub>O • C<sub>2</sub>H<sub>5</sub>OH.

Bond angle	Degree	Bond angle	Degree
N(1)-Re(1)-N(2)	75.3(2)	N(5)-Re(3)-N(6)	74.8(2)
N(1)-Re(1)-S(1)	78.3(1)	N(5)-Re(3)-S(5)	81.1(1)
N(1)-Re(1)-C(11)	97.4(3)	N(5)-Re(3)-C(38)	100.6(3)
N(1)-Re(1)-C(13)	95.3(3)	N(5)-Re(3)-C(39)	94.5(3)
C(12)-Re(1)-C(13)	89.6(3)	C(38)-Re(3)-C(39)	88.1(3)
Re(1)-S(1)-S(2)	109.77(9)	Re(3)-S(5)-S(6)	109.1(1)
N(3)-Re(2)-N(4)	74.6(2)	N(7)-Re(4)-N(8)	74.8(2)
N(3)-Re(2)-S(3)	78.4(1)	N(7)-Re(4)-S(7)	89.5(1)
N(3)-Re(2)-C(25)	99.4(3)	N(7)-Re(4)-C(51)	173.9(3)
N(3)-Re(2)-C(26)	95.5(3)	N(7)-Re(4)-C(52)	93.0(3)
C(25)-Re(2)-C(26)	87.5(3)	C(51)-Re(4)-C(52)	901(3)
Re(2)-S(3)-S(4)	108.43(9)	Re(4)-S(7)-S(8)	110.1(1)



**Table A3.5** Crystal Data and Structure Refinement for Complex **5** + 4H<sub>2</sub>O.<sup>a</sup>

Empirical formula	C <sub>26</sub> H <sub>26</sub> N <sub>4</sub> O <sub>14</sub> Re <sub>2</sub> S <sub>2</sub>
Formula weight	1055.03
Crystal system	monoclinic
Space group	Pc
a (Å)	8.09140(10)
b (Å)	7.8966(2)
c (Å)	26.1412(5)
α (deg)	90
β (deg)	98.6020(10)
γ (deg)	90
V (Å <sup>3</sup> )	1651.49(6)
Z	2
D <sub>calcd</sub> (g/cm <sup>3</sup> )	2.122
T (K)	173.0
λ (Å)	1.54178 (CuKα)
(μ / mm <sup>-1</sup> )	15.942
F(000)	1008.0
2θ range for data collection (deg)	3.418 to 144.498
R <sub>1</sub> , wR <sub>2</sub> [ <i>I</i> ≥ 2σ( <i>I</i> )]	0.0278, 0.0715

$$^a R_1 = \Sigma \|F_0 - F_c\| / \Sigma |F_0| ; wR_2 = [\Sigma w(F_0^2 - F_c^2)^2 / [\Sigma w(F_0^2)^2]]^{1/2}$$

**Table A3.6** Selected Bond Lengths (Å) for Complex **5** + 4 H<sub>2</sub>O.

Bond	Distance (Å)	Bond	Distance (Å)
C(1)-C(2)	1.400(16)	C(18)-C(19)	1.447(17)
C(1)-N(1)	1.330(14)	C(18)-N(3)	1.344(16)
C(2)-C(3)	1.40(2)	C(19)-C(20)	1.403(16)
C(3)-C(4)	1.356(19)	C(19)-N(4)	1.354(17)
C(4)-C(5)	1.393(15)	C(20)-C(21)	1.38(2)
C(5)-C(6)	1.466(15)	C(21)-C(22)	1.37(2)
C(5)-N(1)	1.378(16)	C(22)-C(23)	1.362(19)
C(6)-C(7)	1.37(2)	C(23)-N(4)	1.363(14)
C(6)-N(2)	1.366(16)	C(24)-O(7)	1.120(14)
C(7)-C(8)	1.39(2)	C(24)-Re(2)	1.937(11)
C(8)-C(9)	1.41(2)	C(25)-O(8)	1.144(15)
C(9)-C(10)	1.36(2)	C(25)-Re(2)	1.929(11)
C(10)-N(2)	1.343(14)	C(26)-O(9)	1.170(14)
C(11)-O(4)	1.121(15)	C(26)-Re(2)	1.889(11)
C(11)-Re(1)	1.948(12)	N(1)-Re(1)	2.157(10)
C(12)-O(5)	1.153(14)	N(2)-Re(1)	2.169(9)
C(12)-Re(1)	1.915(10)	N(3)-Re(2)	2.169(9)
C(13)-O(6)	1.114(14)	N(4)-Re(2)	2.166(9)
C(13)-Re(1)	1.941(11)	O(1)-S(2)	1.486(14)
C(14)-C(15)	1.370(18)	O(2)-S(2)	1.431(16)

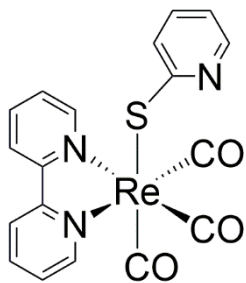
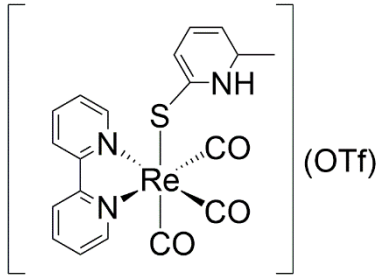
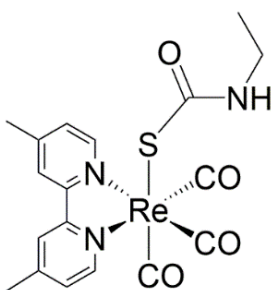
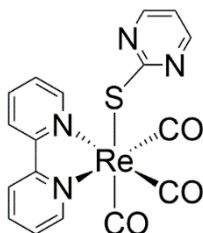
C(14)-N(3)	1.345(15)	O(3)-S(2)	1.469(9)
C(15)-C(16)	1.35(2)	O(10)-Re(2)	2.253(7)
C(16)-C(17)	1.37(2)	Re(1)-S(1)	2.481(3)
C(17)-C(18)	1.409(18)	S(1)-S(2)	2.045(4)

**Table A3.7** Selected Bond Angles (deg) for Complex **5** + 4H<sub>2</sub>O.

Bond	Degree	Bond	Degree
N(1)-C(1)-C(2)	122.8(12)	C(18)-N(3)-Re(2)	116.5(7)
C(1)-C(2)-C(3)	117.8(11)	C(19)-N(4)-C(23)	118.5(10)
C(4)-C(3)-C(2)	119.9(11)	C(19)-N(4)-Re(2)	117.1(7)
C(3)-C(4)-C(5)	120.1(12)	C(23)-N(4)-Re(2)	124.4(9)
C(4)-C(5)-C(6)	123.6(11)	C(11)-Re(1)-N(1)	173.0(5)
N(1)-C(5)-C(4)	120.6(11)	C(11)-Re(1)-N(2)	97.7(4)
N(1)-C(5)-C(6)	115.8(10)	C(11)-Re(1)-S(1)	94.8(4)
C(7)-C(6)-C(5)	123.0(12)	C(12)-Re(1)-C(11)	88.5(5)
N(2)-C(6)-C(5)	115.2(11)	C(12)-Re(1)-C(13)	89.1(5)
N(2)-C(6)-C(7)	121.8(11)	C(12)-Re(1)-N(1)	98.2(4)
C(6)-C(7)-C(8)	119.3(13)	C(12)-Re(1)-N(2)	172.9(4)
C(7)-C(8)-C(9)	118.7(13)	C(12)-Re(1)-S(1)	88.4(3)
C(10)-C(9)-C(8)	118.5(13)	C(13)-Re(1)-C(11)	89.5(5)
N(2)-C(10)-C(9)	123.2(13)	C(13)-Re(1)-N(1)	92.4(4)
O(4)-C(11)-R(1)	177.6(13)	C(13)-Re(1)-N(2)	94.4(4)
O(5)-C(12)-Re(1)	179.8(11)	C(13)-Re(1)-S(1)	175.0(3)
O(6)-C(13)-Re(1)	175.5(10)	N(1)-Re(1)-N(2)	75.5(4)
N(3)-C(14)-C(15)	123.0(12)	N(1)-Re(1)-S(1)	83.7(3)
C(16)-C(15)-C(14)	119.6(12)	N(2)-Re(1)-S(1)	87.7(2)
C(15)-C(16)-C(17)	118.7(14)	C(24)-Re(2)-N(3)	172.4(4)

C(16)-C(17)-C(18)	120.2(14)	C(24)-Re(2)-N(4)	99.0(4)
C(17)-C(18)-C(19)	123.0(12)	C(24)-Re(2)-O(10)	90.0(4)
N(3)-C(18)-C(17)	120.2(12)	C(25)-Re(2)-C(24)	88.5(5)
N(3)-C(18)-C(19)	116.7(10)	C(25)-Re(2)-N(3)	97.8(4)
C(20)-C(19)-C(18)	125.3(11)	C(25)-Re(2)-N(4)	172.1(4)
N(4)-C(19)-C(18)	115.1(10)	C(25)-Re(2)-O(10)	92.9(4)
N(4)-C(19)-C(20)	119.5(11)	C(26)-Re(2)-C(24)	88.6(5)
C(21)-C(20)-C(19)	120.9(12)	C(26)-Re(2)-C(25)	89.0(5)
C(22)-C(21)-C(20)	118.4(12)	C(26)-Re(2)-N(3)	95.7(4)
C(23)-C(22)-C(21)	119.4(12)	C(26)-Re(2)-N(4)	93.6(5)
C(22)-C(23)-N(4)	123.1(12)	C(26)-Re(2)-O(10)	177.6(4)
O(7)-C(24)-Re(2)	179.2(11)	N(3)-Re(2)-O(10)	85.6(3)
O(8)-C(25)-Re(2)	179.5(13)	N(4)-Re(2)-N(3)	74.6(4)
O(9)-C(26)-Re(2)	178.7(10)	N(4)-Re(2)-O(10)	84.8(4)
C(1)-N(1)-C(5)	118.8(10)	S(2)-S(1)-Re(1)	109.65(15)
C(1)-N(1)-Re(1)	124.7(8)	O(1)-S(2)-S(1)	106.8(5)
C(5)-N(1)-Re(1)	116.6(7)	O(2)-S(2)-O(1)	110.5(8)
C(6)-N(2)-Re(1)	117.0(7)	O(2)-S(2)-O(3)	114.0(6)
C(10)-N(2)-C(6)	118.4(10)	O(2)-S(2)-S(1)	107.8(5)
C(10)-N(2)-Re(1)	124.7(8)	O(3)-S(2)-O(1)	109.1(7)
C(14)-N(3)-Re(2)	125.3(7)	O(3)-S(2)-S(1)	108.3(4)
C(18)-N(3)-C(14)	118.2(10)		

**Table A3.8** Survey of Re(I) tricarbonyl complexes with S coordinating ligand in CSD version 5.38 ( 2017).

CSD Code	Ref	Structure	Re-S (Å)	Re-CO <sub>axial</sub> (Å)
ERUFII	<i>Inorganica Chim. Acta</i> , 2017, <b>460</b> , 127-133.		2.4945(13)	1.924(6)
ERUFOO	<i>Inorganica Chim. Acta</i> , 2017, <b>460</b> , 127-133.		2.5428(10)	1.931(3)
EXACAH	<i>Chem. Eur. J.</i> , 2004, <b>10</b> , 1765-1777.		2.496(2)	1.919(10)
RUMPUL	<i>Dalton Trans.</i> , 2009, 4458-4467.		2.5012(13)	1.927(5)
<b>Average Distance ± SD:</b>			2.51 ± 0.02	1.93 ± 0.01

### *Lipophilicity and partition coefficient (log P)*

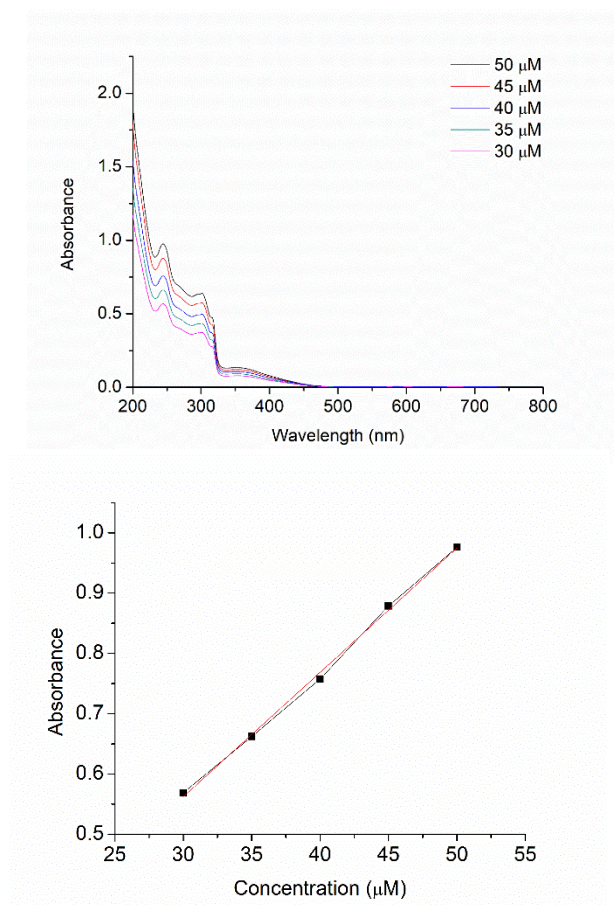
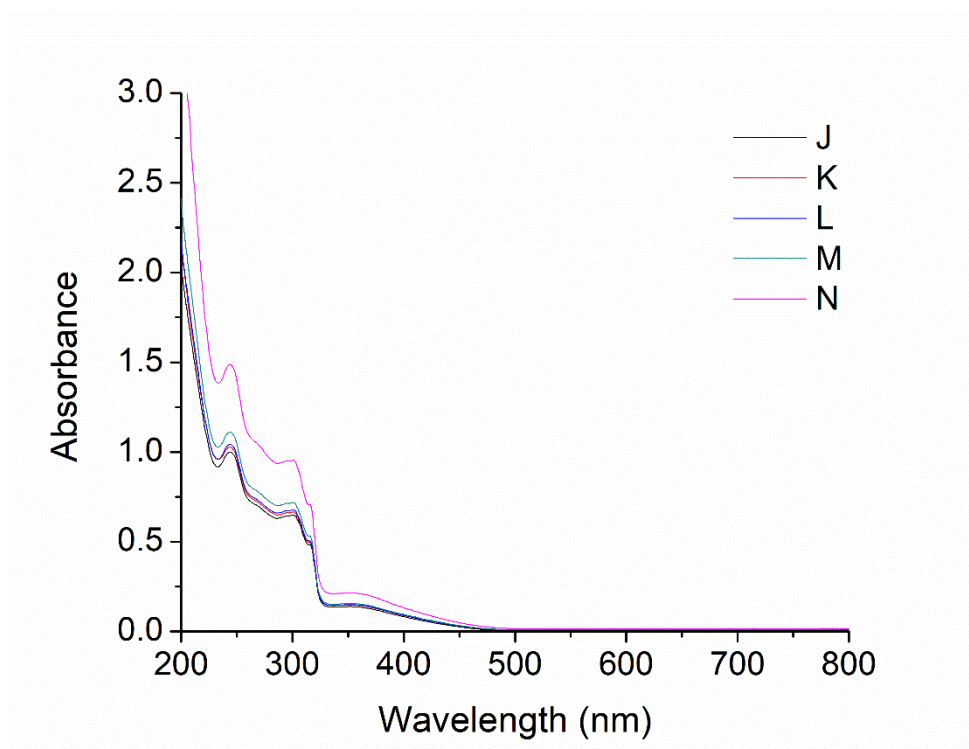


**Figure A3.5** UV-visible absorbance spectrum of **4** in H<sub>2</sub>O to obtain a calibration curve. Assignment of epsilon ( $\epsilon$ ) values at 243 nm shown in Table A3.9. Epsilon ( $\epsilon$ ) values at 243 nm shown in Table A3.9.

**Table A3.9** Epsilon ( $\epsilon$ ) values of UV-visible absorbance spectra as shown in Figure A3.5.

Complex	$\epsilon$ (M <sup>-1</sup> cm <sup>-1</sup> )
<b>1</b>	17,000
<b>4</b>	20,600



Sample	Initial amount of <b>4</b> ( $\mu\text{mol}$ )	Water (mL)	n-Octanol (mL)
J	1.25	25	25
K	1	20	30
L	0.75	15	35
M	0.5	10	40
N	0.25	5	45

**Figure A3.6** UV-visible absorbance spectra of **4** in aqueous phase of the above solutions J - N (water/ n-octanol mixtures) obtained after shaking for 24 hr at 25 C.



### *Synchrotron Based X-ray Fluorescence Microscopy (XFM)*

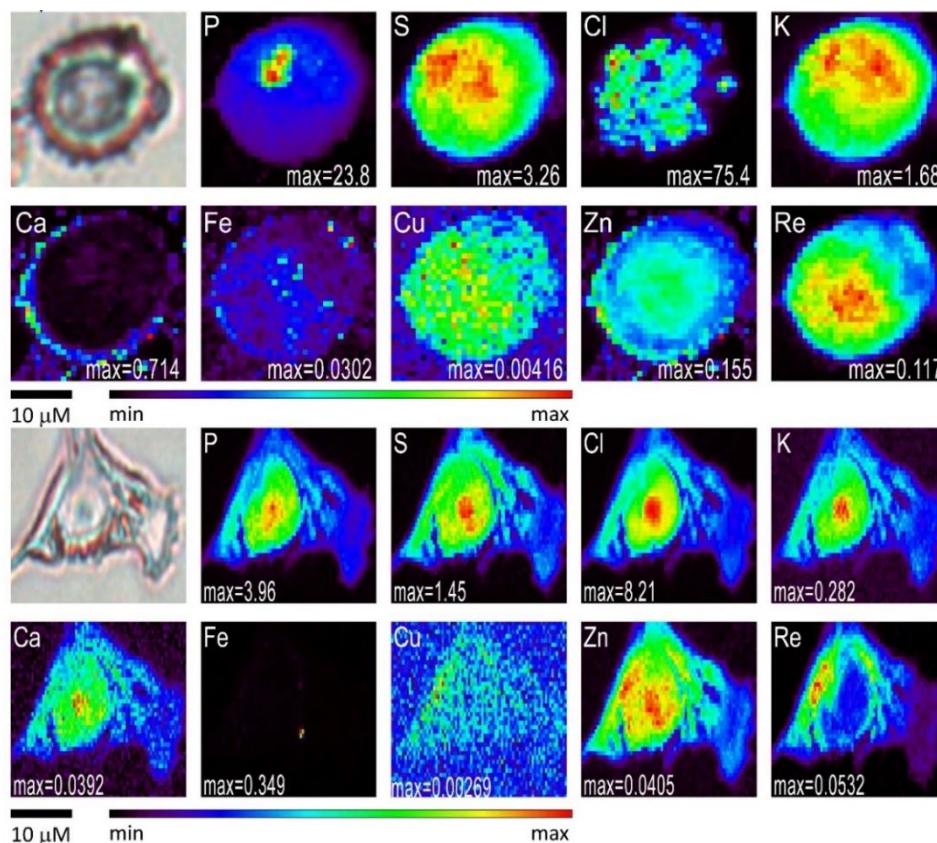


**Figure A3.7** Optical micrographs (top left) and scattered X-ray (XS) and XRF elemental distribution map of MDA-MB-231 cells treated with **1** for 6 h. The maximum elemental area densities (quantified from standards and expressed in  $\mu\text{g cm}^{-2}$ ) are given in the bottom of each map. The scale bar represents 10  $\mu\text{M}$  unless otherwise indicated.

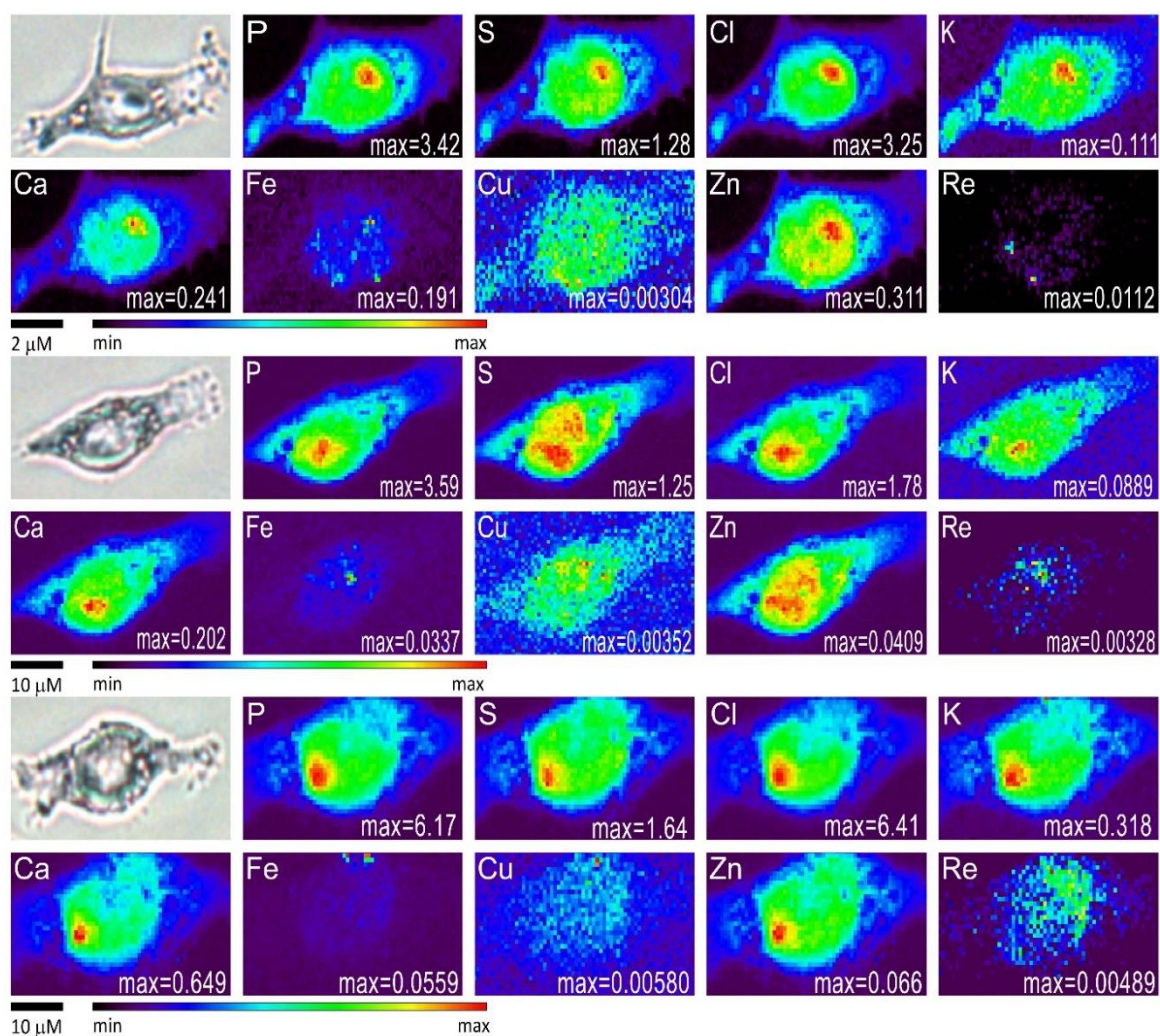


**Figure A3.8** Optical micrographs (top left) and scattered X-ray (XS) and XRF elemental distribution map of MDA-MB-231 cells treated with **4** for 6 h. The maximum elemental area densities (quantified from standards and expressed in  $\mu\text{g cm}^{-2}$ ) are given in the bottom of each map. The scale bar represents 10  $\mu\text{M}$  unless otherwise indicated.

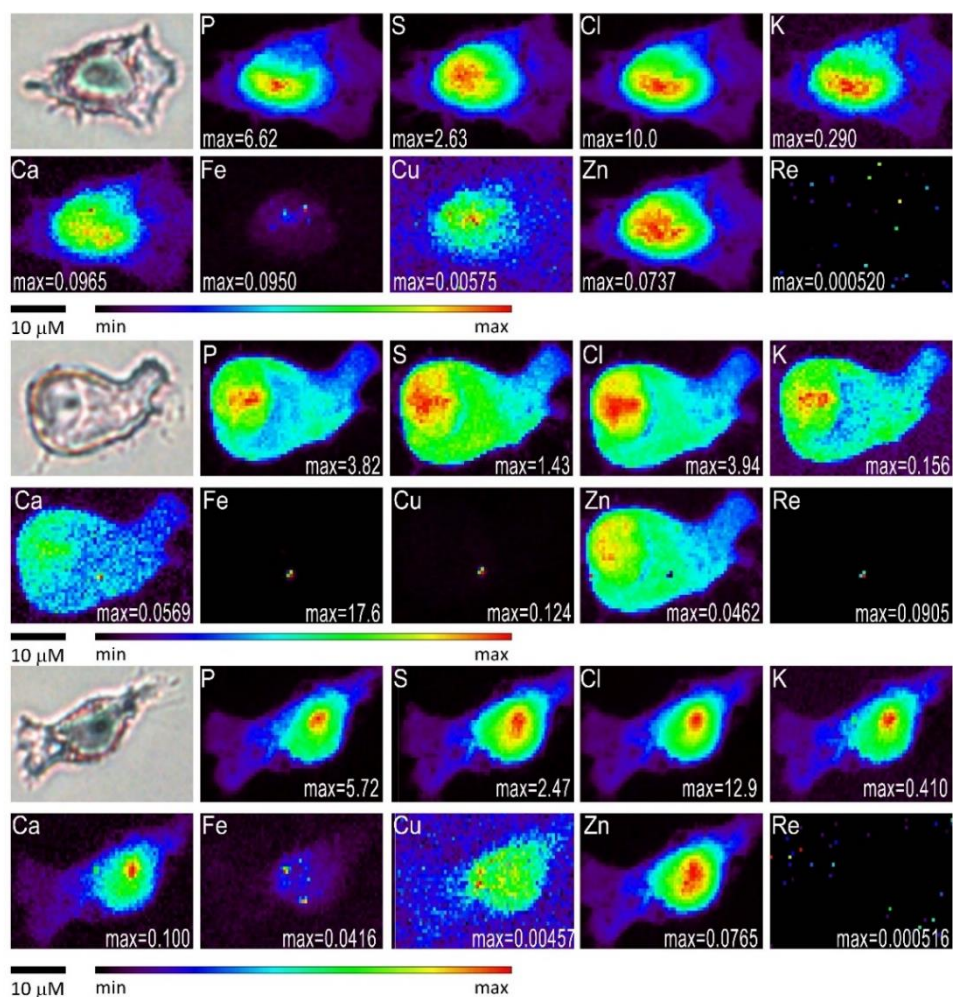


**Figure A3.9** Optical micrographs (top left) and scattered X-ray (XS) and XRF elemental distribution map of MDA-MB-231 cells treated with DMEM for 6 h. The maximum elemental area densities (quantified from standards and expressed in  $\mu\text{g cm}^{-2}$ ) are given in the bottom of each map. The scale bar represents 10  $\mu\text{M}$  unless otherwise indicated.



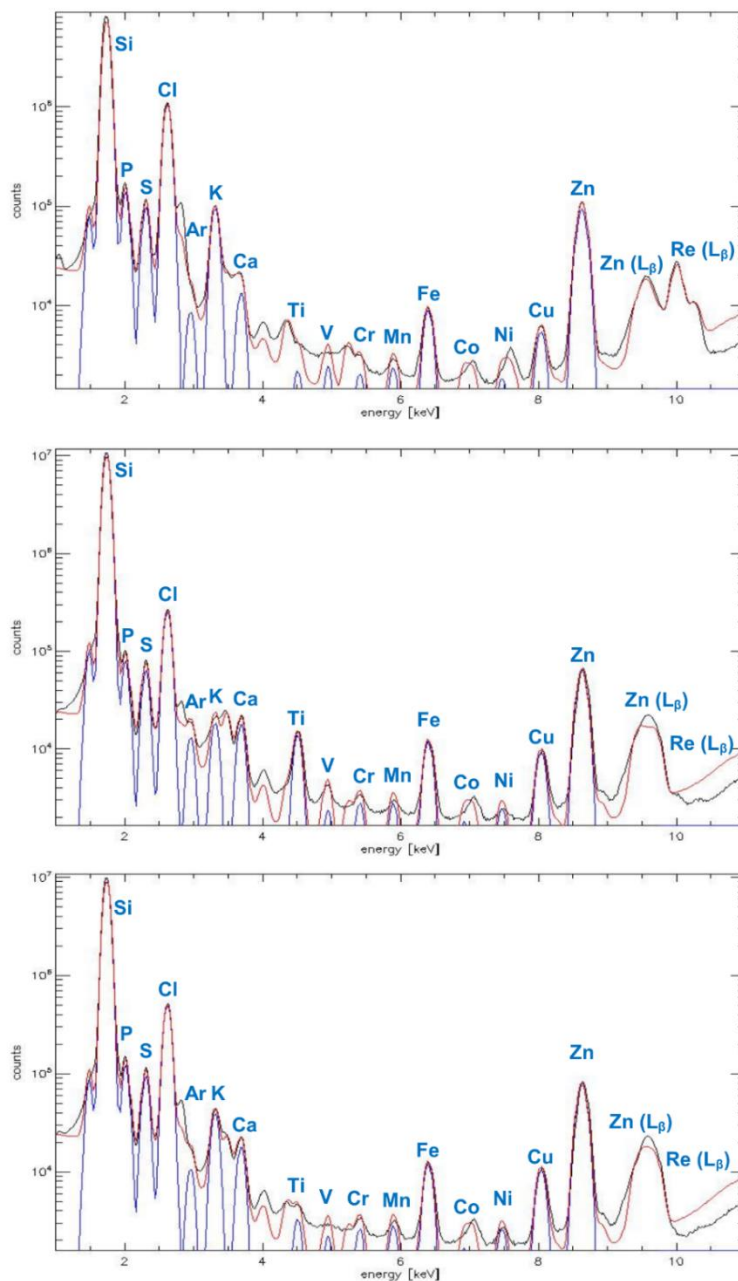


**Figure A3.10** XFM spectra (black) of MDA-MB-231 sample cells treated for 6 hr with 20  $\mu$ M solutions of **1** (top) and **4** (middle) or in DMEM (bottom). Each figure shows the fit to the spectrum (red) and the contribution of the  $K\alpha$  peaks used in the fitting (blue) with their corresponding labelling.

## References

1. D. Hanahan and R. A. Weinberg, *Cell*, 2000, **100**, 57-70.
2. A. Sudhakar, *J. Cancer Sci. Ther.*, 2009, **1**, 1.
3. B. Stewart and C. P. Wild, *IARC*, 2014.
4. A. Dobrovic and D. Simpfendorfer, *Cancer Res.*, 1997, **57**, 3347.
5. W. You and M. Henneberg, *Evol Appl*, 2017, **11**, 140-152.
6. V. T. DeVita and E. Chu, *Cancer Res.*, 2008, **68**, 8643-8653.
7. A. Brandt, *Science*, 1988, **239**, 375-380.
8. B. Rosenberg, L. Van Camp and T. Krigas, *Nature*, 1965, **205**, 698-699.
9. A.-M. Florea and D. Büsselberg, *Cancers*, 2011, **3**, 1351-1371.
10. P. C. Bruijninx and P. J. Sadler, *Curr. Opin. Chem. Biol.*, 2008, **12**, 197-206.
11. P. Jordan and M. Carmo-Fonseca, *Cell. Mol. Life Sci.*, 2000, **57**, 1229-1235.
12. C. F. Harrington, R. C. Le Pla, G. D. Jones, A. L. Thomas and P. B. Farmer, *Chem. Res. Toxicol*, 2010, **23**, 1313-1321.
13. C. Saris, P. M. van de Vaart, R. Rietbroek and F. Blorumaert, *Carcinogenesis*, 1996, **17**, 2763-2769.
14. M. Shimada, H. Itamochi and J. Kigawa, *Cancer Manag. Res.*, 2013, **5**, 67.
15. N. J. Wheate, S. Walker, G. E. Craig and R. Oun, *Dalton Trans.*, 2010, **39**, 8113-8127.
16. B. Desoize and C. Madoulet, *Crit. Rev. Oncol. Hematol.*, 2002, **42**, 317-325.
17. N. Shah and D. S. Dizon, *Future Oncol.*, 2009, **5**, 33-42.
18. D. A. Günes, A.-M. Florea, F. Splettstoesser and D. Büsselberg, *Neurotoxicology*, 2009, **30**, 194-202.
19. A.-M. Florea and D. Büsselberg, *Biomaterials*, 2006, **19**, 419-427.
20. R. Y. Tsang, T. Al-Fayea and H.-J. Au, *Drug Saf.*, 2009, **32**, 1109-1122.
21. R. Skinner, A. D. J. Pearson, M. W. English, L. Price, R. A. Wyllie, M. G. Coulthard, M. G. Coulthard and A. W. Craft, *Lancet*, 1996, **348**, 578-580.
22. K. R. G. Knight, D. F. Kraemer and E. A. Neuwelt, *J. Clin. Oncol*, 2005, **23**, 8588-8596.
23. K. R. Knight, D. F. Kraemer, C. Winter and E. A. Neuwelt, *J. Clin. Oncol*, 2007, **25**, 1190-1195.
24. P. Leohrer and L. Einhorn, *Ann. Intern. Med.*, 1984, **100**, 704-713.
25. R. T. Greenlee, M. B. Hill-Harmon, T. Murray and M. Thun, *CA Cancer J. Clin.*, 2001, **51**, 15-36.
26. D.-W. Shen, L. M. Pouliot, M. D. Hall and M. M. Gottesman, *Pharmacol. Rev.*, 2012, **64**, 706-721.
27. O. B. Katz and Y. Shaked, *Drug Resist. Updat.*, 2015, **19**, 33-42.
28. S.-J. Kim, J.-S. Kim, E. S. Park, J.-S. Lee, Q. Lin, R. R. Langley, M. Maya, J. He, S.-W. Kim and Z. Weihua, *Neoplasia*, 2011, **13**, 286-298.
29. J. M. Roodhart, L. G. Daenen, E. C. Stigter, H.-J. Prins, J. Gerrits, J. M. Houthuijzen, M. G. Gerritsen, H. S. Schipper, M. J. Backer and M. van Amersfoort, *Cancer Cell*, 2011, **20**, 370-383.
30. R. Agarwal and S. B. Kaye, *Nat. Rev. Cancer*, 2003, **3**, 502.
31. A. B. Kornblith, M. Kemeny, B. L. Peterson, J. Wheeler, J. Crawford, N. Bartlett, G. Fleming, S. Graziano, H. Muss and H. J. Cohen, *Cancer*, 2002, **95**, 989-996.

32. T. J. Dougherty, C. J. Gomer, B. W. Henderson, G. Jori, D. Kessel, M. Korbelik, J. Moan and Q. Peng, *J. Natl. Cancer Inst.*, 1998, **90**, 889-905.
33. T. Hasan, B. Ortel, N. Solban and B. Pogue, *Cancer Med.*, 2003, **7**, 537-548.
34. N. J. Farrer, L. Salassa and P. J. Sadler, *Dalton Trans.*, 2009, **48**, 10690-10701.
35. G. N. Lewis and M. Kasha, *J. Am. Chem. Soc.*, 1944, **66**, 2100-2116.
36. A. Gilbert and J. E. Baggott, *Essentials of Molecular Photochemistry*, CRC, 1991.
37. M. Proetto, W. Liu, A. Hagenbach, U. Abram and R. Gust, *Eur. J. Med. Chem.*, 2012, **53**, 168-175.
38. I. J. Macdonald and T. J. Dougherty, *J. Porphyr. Phthalocyanines*, 2001, **5**, 105-129.
39. F. Hund, *Z. Phys*, 1925, **33**, 345-371.
40. R. Motterlini, J. E. Clark, R. Foresti, P. Sarathchandra, B. E. Mann and C. J. Green, *Circ. Res.*, 2002, **90**, e17-e24.
41. R. D. Rimmer, H. Richter and P. C. Ford, *Inorg. Chem.*, 2010, **49**, 1180-1185.
42. U. Schatzschneider, *Inorganica Chim. Acta*, 2011, **374**, 19-23.
43. R. Motterlini and L. E. Otterbein, *Nat. Rev. Drug Discov.*, 2010, **9**, 728.
44. M. Stupfel and G. Bouley, *Ann. N. Y. Acad. Sci.*, 1970, **174**, 342-368.
45. L. Goldbaum, T. Orellano and E. Dergal, *Ann. Clin. Lab. Sci.*, 1976, **6**, 372-376.
46. M. D. Maines, *FASEB J.*, 1988, **2**, 2557-2568.
47. H. Was, J. Dulak and A. Jozkowicz, *Curr. Drug Targets*, 2010, **11**, 1551-1570.
48. M. A. Alaoui-Jamali, T. A. Bismar, A. Gupta, W. A. Szarek, J. Su, W. Song, Y. Xu, B. Xu, G. Liu, J. Z. Vlahakis, G. Roman, J. Jiao and H. M. Schipper, *Cancer Res.*, 2009, **69**, 8017-8024.
49. G. Kikuchi, T. Yoshida and M. Noguchi, *Biochem. Biophys. Res. Commun.*, 2005, **338**, 558-567.
50. P. R. Brock, R. Maibach, M. Childs, K. Rajput, D. Roebuck, M. J. Sullivan, V. Laithier, M. Ronghe, P. Dall'Igna, E. Hiyama, B. Brichard, J. Skeen, M. E. Mateos, M. Capra, A. A. Rangaswami, M. Ansari, C. Rechnitzer, G. J. Veal, A. Covezzoli, L. Brugières, G. Perilongo, P. Czauderna, B. Morland and E. A. Neuwelt, *N. Engl. J. Med.*, 2018, **378**, 2376-2385.
51. M. Sooriyaarachchi, J. Gailer, N. V. Dolgova, I. J. Pickering and G. N. George, *J. Inorg. Biochem.*, 2016, **162**, 96-101.
52. W. Noddack, I. Tacke and O. Berg, *Naturwissenschaften*, 1925, **13**, 567-574.
53. H. Yoshihara, *Spectrochimica Acta Part B: Atomic Spectroscopy*, 2004, **59**, 1305-1310.
54. J. R. Dilworth and S. J. Parrott, *Chem. Soc. Rev.*, 1998, **27**, 43-55.
55. R. Alberto, R. Schibli, A. Egli, A. P. Schubiger, U. Abram and T. A. Kaden, *J. Am. Chem. Soc.*, 1998, **120**, 7987-7988.
56. D. L. Morse and M. S. Wrighton, *J. Am. Chem. Soc.*, 1976, **98**, 3931-3934.
57. J. C. Luong, L. Nadjo and M. S. Wrighton, *J. Am. Chem. Soc.*, 1978, **100**, 5790-5795.
58. M. Wrighton and D. L. Morse, *J. Am. Chem. Soc.*, 1974, **96**, 998-1003.
59. C. C. Konkankit, A. P. King, K. M. Knopf, T. L. Southard and J. J. Wilson, *ACS Med. Chem. Lett.*, 2019, **10**, 822-827.
60. K. M. Knopf, B. L. Murphy, S. N. MacMillan, J. M. Baskin, M. P. Barr, E. Boros and J. J. Wilson, *J. Am. Chem. Soc.*, 2017, **139**, 14302-14314.

61. A. V. Shtemenko, P. Collery, N. I. Shtemenko, K. V. Domasevitch, E. D. Zabitskaya and A. A. Golichenko, *Dalton Trans.*, 2009, 5132-5136.
62. N. Shtemenko, P. Collery and A. Shtemenko, *Anticancer Res.*, 2007, **27**, 2487-2492.
63. A. Leonidova and G. Gasser, *ACS Chem. Biol.*, 2014, **9**, 2180-2193.
64. T. Gianferrara, C. Spagnul, R. Alberto, G. Gasser, S. Ferrari, V. Pierroz, A. Bergamo and E. Alessio, *ChemMedChem*, 2014, **9**, 1231-1237.
65. A. Leonidova, V. Pierroz, R. Rubbiani, Y. Lan, A. G. Schmitz, A. Kaech, R. K. O. Sigel, S. Ferrari and G. Gasser, *Chem. Sci.*, 2014, **5**, 4044-4056.
66. A. E. Pierri, A. Pallaoro, G. Wu and P. C. Ford, *J. Am. Chem. Soc.*, 2012, **134**, 18197-18200.
67. S. C. Marker, S. N. MacMillan, W. R. Zipfel, Z. Li, P. C. Ford and J. J. Wilson, *Inorg. Chem.*, 2018, **57**, 1311-1331.
68. K. Hasegawa, *The Rigaku Journal*, 2012, **28**, 14-18.
69. A. Kirsch-De Mesmaeker, J.-P. Lecomte and J. M. Kelly, *Top. Curr. Chem*, 1996, **177**, 25-76.
70. J. R. Lakowicz, "Instrumentation for fluorescence spectroscopy." *Principles of fluorescence spectroscopy*. Springer, Boston, MA, 1999. 25-61.
71. S. Nonell and C. Flors, *Singlet Oxygen: Applications in Biosciences and Nanosciences*, Royal Society of Chemistry, 2016.
72. S. Nonell and S. E. Braslavsky, "Time-resolved singlet oxygen detection", in *Singlet Oxygen, UV-A and Ozone* (L. Packer and H. Sies, Eds.), *Methods Enzymol.*, 2000, 319, 37-49.
73. A. Leonidova, V. Pierroz, R. Rubbiani, J. Heier, S. Ferrari and G. Gasser, *Dalton Trans.*, 2014, **43**, 4287-4294.
74. A. Mahdaviifar, M. Navaei, P. J. Hesketh, J. D. Dimandja, J. R. Stetter and G. McMurray, *ECS J. Solid State Sci. Technol.*, 2015, **4**, S3062-S3066.
75. L. P. Candéias, D. P. S. MacFarlane, S. L. W. McWhinnie, N. L. Maidwell, C. A. Roeschlaub, P. G. Sammes and R. Whittlesey, *J. Chem. Soc., Perkin Trans. 2*, 1998, 2333-2334.
76. H. Winick, *Sci. Am.*, 1987, **257**, 88-101.
77. R. Ortega, A. Carmona, I. Llorens and P. L. Solari, *J. Anal. At. Spectrom.*, 2012, **27**, 2054-2065.
78. C. J. Fahrni, *Curr. Opin. Struct. Biol.*, 2007, **11**, 121-127.
79. Penner-Hahn, J. E., *Metals in Cells: X-Ray Fluorescence Microscopy in Encyclopedia of Inorganic and Bioinorganic Chemistry*, John Wiley & Sons, Ltd, 2011.
80. T. Paunesku, S. Vogt, J. Maser, B. Lai and G. Woloschak, *J. Cell. Biochem.*, 2006, **99**, 1489-1502.
81. L. Galluzzi, L. Senovilla, I. Vitale, J. Michels, I. Martins, O. Kepp, M. Castedo and G. Kroemer, *Oncogene*, 2011, **31**, 1869.
82. K. Szaciłowski, W. Macyk, A. Drzewiecka-Matuszek, M. Brindell and G. Stochel, *Chem. Rev.*, 2005, **105**, 2647-2694.
83. S. Monro, K. L. Colón, H. Yin, J. Roque, P. Konda, S. Gujar, R. P. Thummel, L. Lilge, C. G. Cameron and S. A. McFarland, *Chem. Rev.*, 2019, **119**, 797-828.
84. G. Graschew and M. Shopova, *Lasers Med. Sci.*, 1986, **1**, 181-186.

85. J. Boczkowski, J. J. Poderoso and R. Motterlini, *Trends Biochem. Sci.*, 2006, **31**, 614-621.
86. B. Wegiel, D. Gallo, E. Csizmadia, C. Harris, J. Belcher, G. M. Vercellotti, N. Penacho, P. Seth, V. Sukhatme, A. Ahmed, P. P. Pandolfi, L. Helczynski, A. Bjartell, J. L. Persson and L. E. Otterbein, *Cancer Res.*, 2013, **74**, 7009-7021.
87. A. Kastl, S. Dieckmann, K. Wähler, T. Völker, L. Kastl, A. L. Merkel, A. Vultur, B. Shannan, K. Harms and M. Ocker, *ChemMedChem*, 2013, **8**, 924-927.
88. A. Kastl, S. Dieckmann, K. Wähler, T. Völker, L. Kastl, A. L. Merkel, A. Vultur, B. Shannan, K. Harms, M. Ocker, W. J. Parak, M. Herlyn and E. Meggers, *ChemMedChem*, 2013, **8**, 924-927.
89. A. Leonidova, V. Pierroz, R. Rubbiani, J. Heier, S. Ferrari and G. Gasser, *Dalton Trans.*, 2014, **43**, 4287-4294.
90. F. Zobi, O. Blacque, H. W. Schmalke, B. Spingler and R. Alberto, *Inorg. Chem.*, 2004, **43**, 2087-2096.
91. J. Lecina, Ò. Palacios, S. Atrian, M. Capdevila and J. Suades, *J. Biol. Inorg. Chem.*, 2015, **20**, 465-474.
92. V. Lopez, F. Foolad and S. L. Kelleher, *Cancer Lett.*, 2011, **304**, 41-51.
93. S. Alam and S. L. Kelleher, *Nutrients*, 2012, **4**, 875-903.
94. D. B. G. Williams and M. Lawton, *J. Org. Chem.*, 2010, **75**, 8351-8354.
95. B. Salignac, P. V. Grundler, S. Cayemittes, U. Frey, R. Scopelliti, A. E. Merbach, R. Hedinger, K. Hegetschweiler, R. Alberto and U. Prinz, *Inorg. Chem.*, 2003, **42**, 3516-3526.
96. J. Degen, K. Reinecke and H.-H. Schmidtke, *Chem. Phys.*, 1992, **162**, 419-426.
97. J. E. Sabol and M. G. Rockley, *J. Photochem. Photobiol. A*, 1987, **40**, 245-257.
98. B. A. Inc, pp. 53711-55373.
99. O. V. Dolomanov, L. J. Bourhis, R. J. Gildea, J. A. Howard and H. Puschmann, *J. Appl. Crystallogr.*, 2009, **42**, 339-341.
100. G. M. Sheldrick, *Acta Crystallogr. A*, 2015, **71**, 3-8.
101. G. M. Sheldrick, *Acta Crystallogr. C*, 2015, **71**, 3-8.
102. S. C. Marker, S. N. MacMillan, W. R. Zipfel, Z. Li, P. C. Ford and J. J. Wilson, *Inorg. Chem.*, 2018, **57**, 1311-1331.
103. OECD, *Test No. 107: Partition Coefficient (n-octanol/water): Shake Flask Method*. OECD Publishing, 1995
104. A. Enriquez Garcia, B. Lai, S. G. Gopinathan, H. H. Harris, C. S. Shemanko and F. Jalilehvand, *Chem. Commun.*, 2019, **55**, 8223-8226.
105. R. McRae, B. Lai and C. J. Fahrni, *Metallomics*, 2013, **5**, 52-61.
106. R. McRae, B. Lai, S. Vogt and C. J. Fahrni, *J. Struct. Biol.*, 2006, **155**, 22-29.
107. P. Van Epsen, *Spectrum Evaluation*, in *Handbook of X-ray Spectrometry*, R. E. Van Grieken and A. A. Markowicz, CRC Press, Editon., 2002, vol. 29.
108. S. Vogt, *J. Phys. IV*, 2003, **104**, 635-638.
109. E. A. Carter, B. S. Rayner, A. I. McLeod, L. E. Wu, C. P. Marshall, A. Levina, J. B. Aitken, P. K. Witting, B. Lai, Z. Cai, S. Vogt, Y. C. Lee, C. I. Chen, M. J. Tobin, H. H. Harris and P. A. Lay, *Mol. Biosyst.*, 2010, **6**, 1316-1322.
110. A. Vlček Jr, *Ultrafast excited-state processes in Re (I) carbonyl-diimine complexes: from excitation to photochemistry* Springer



111. V. Fernández-Moreira and H. Sastre-Martín, *Inorganica Chim. Acta.*, 2017, **460**, 127-133.
112. B. Salignac, P. V. Grundler, S. Cayemittes, U. Frey, R. Scopelliti, A. E. Merbach, R. Hedinger, K. Hegetschweiler, R. Alberto and U. Prinz, *Inorg. Chem*, 2003, **42**, 3516-3526.
113. P. Kurz, B. Probst, B. Spingler and R. Alberto, *Eur. J. Inorg. Chem*, 2006, **2006**, 2966-2974.
114. Y. Kim, F. W. Vanhelmont, C. L. Stern and J. T. Hupp, *Inorganica Chim. Acta*, 2001, **318**, 53-60.
115. L. Sacksteder, A. P. Zipp, E. A. Brown, J. Streich, J. Demas and B. DeGraff, *Inorg. Chem.*, 1990, **29**, 4335-4340.
116. J. S. Strukl and J. L. Walter, *Spectrochim. Acta A*, 1971, **27**, 209-221.
117. V. Fernández-Moreira, F. L. Thorp-Greenwood, A. J. Amoroso, J. Cable, V. Gray, A. J. Hayes, R. L. Jenkins, B. M. Kariuki, D. Lloyd and C. O. Millet, *Org. Biomol. Chem*, 2010, **8**, 3888-3901.
118. L. D. Ramos, H. M. da Cruz and K. P. M. Frin, *Photochem. Photobiol. Sci.*, 2017, **16**, 459-466.
119. K. Bhattacharyya and P. Das, *Chem. Phys. Lett.*, 1985, **116**, 326-332.
120. T. P. A. Devasagayam, A. R. Sundquist, P. Di Mascio, S. Kaiser and H. Sies, *J. Photochem. Photobiol. B*, 1991, **9**, 105-116.
121. N. S. Sisombath and F. Jalilehvand, *Chem. Res. Toxicol.*, 2015, **28**, 2313-2324.
122. A. E. Pierri, A. Pallaoro, G. Wu and P. C. Ford, *J. Am. Chem. Soc.*, 2012, **134**, 18197-18200.
123. B. Testa, P. Crivori, M. Reist and P.-A. Carrupt, *Perspect. Drug Discovery Des.*, 2000, **19**, 179-211.
124. E. A. Ahmed, H. M. Omar, S. K. A. elghaffar, S. M. M. Ragb and A. Y. Nasser, *Food Chem. Toxicol.*, 2011, **49**, 1115-1121.
125. R. T. Dorr, *Semin. Oncol.*, 1991, **18**, 48-58.
126. A. W.-T. Choi, M.-W. Louie, S. P.-Y. Li, H.-W. Liu, B. T.-N. Chan, T. C.-Y. Lam, A. C.-C. Lin, S.-H. Cheng and K. K.-W. Lo, *Inorg. Chem.*, 2012, **51**, 13289-13302.
127. I. Kitanovic, S. Can, H. Alborzinia, A. Kitanovic, V. Pierroz, A. Leonidova, A. Pinto, B. Spingler, S. Ferrari and R. Molteni, *Chem.: Eur. J.*, 2013, **20**, 2496-2507.
128. J. L. Wedding, H. H. Harris, C. A. Bader, S. E. Plush, R. Mak, M. Massi, D. A. Brooks, B. Lai, S. Vogt and M. V. Werrett, *Metallomics*, 2017, **9**, 382-390.
129. W. H. Stein and S. Moore, *J. Biol. Chem*, 1954, **211**, 915-926.
130. M. Sooriyaarachchi, G. N. George, I. J. Pickering, A. Narendran and J. Gailer, *Metallomics*, 2016, **8**, 1170-1176.
131. C. S. Allardyce, A. Dorcier, C. Scolaro and P. J. Dyson, *Appl. Organomet. Chem*, 2005, **19**, 1-10.
132. N. Viola-Villegas, A. E. Rabideau, J. Cesnavicious, J. Zubieta and R. P. Doyle, *ChemMedChem*, 2008, **3**, 1387-1394.
133. D. K. Orsa, G. K. Haynes, S. K. Pramanik, M. O. Iwunze, G. E. Greco, D. M. Ho, J. A. Krause, D. A. Hill, R. J. Williams and S. K. Mandal, *Inorg. Chem. Commun.*, 2008, **11**, 1054-1056.
134. M.-W. Louie, H.-W. Liu, M. H.-C. Lam, T.-C. Lau and K. K.-W. Lo, *Organometallics*, 2009, **28**, 4297-4307.

135. A. J. Amoroso, M. P. Coogan, J. E. Dunne, V. Fernández-Moreira, J. B. Hess, A. J. Hayes, D. Lloyd, C. Millet, S. J. Pope and C. Williams, *ChemComm*, 2007, 3066-3068.
136. A. Leonidova, V. Pierroz, L. A. Adams, N. Barlow, S. Ferrari, B. Graham and G. Gasser, *ACS Med. Chem. Lett.*, 2014, **5**, 809-814.
137. G. Kirker, S. Zelinka, S.-C. Gleber, D. Vine, L. Finney, S. Chen, Y. P. Hong, O. Uyarte, S. Vogt, J. Jellison, B. Goodell and J. E. Jakes, *Sci. Rep.*, 2017, **7**, 41798.
138. Bruker-AXS. SAINT; Madison, Wisconsin, USA, 2017.
139. Bruker-AXS. XPREP; Madison, Wisconsin, USA, 2017.
140. C. Tessier, A. L. Beauchamp and F. D. Rochon, *J. Inorg. Biochem.*, 2001, **85**, 77-78.
141. A. Enriquez Garcia, B. Lai, S. G. Gopinathan, H. H. Harris, C. S. Shemanko and F. Jalilehvand, *ChemComm*, 2019, **55**, 8223-8226.
142. E. Hevia, J. Pérez, V. Riera and D. Miguel, *Organometallics*, 2003, **22**, 257-263.
143. V. Fernández-Moreira and H. Sastre-Martín, *Inorganica Chim. Acta*, 2017, **460**, 127-133.
144. S. Kabir, J. Alam, S. Ghosh, K. Kundu, G. Hogarth, D. Tocher, G. Hossain and H. Roesky, *Dalton Trans.*, 2009, 4458-4467.
145. L. Cuesta, D. C. Gerbino, E. Hevia, D. Morales, M. E. Navarro Clemente, J. Pérez, L. Riera, V. Riera, D. Miguel and I. Del Río, *Chem. Eur. J.*, 2004, **10**, 1765-1777.
146. C. Stoica, P. Verwer, H. Meekes, P. J. C. M. van Hoof, F. M. Kaspersen and E. Vlieg, *Cryst. Growth Des.*, 2004, **4**, 765-768.
147. A. Z. M. Pauzi, S. K. Yeap, N. Abu, K. L. Lim, A. R. Omar, S. A. Aziz, A. L. T. Chow, T. Subramani, S. G. Tan and N. B. Alitheen, *Chin. Med. J.*, 2016, **11**, 46.
148. A. J. Amoroso, R. J. Arthur, M. P. Coogan, J. B. Court, V. Fernández-Moreira, A. J. Hayes, D. Lloyd, C. Millet and S. J. A. Pope, *New J. Chem.*, 2008, **32**, 1097-1102.
149. A. Gupte and R. J. Mumper, *Cancer Treat. Rev.*, 2009, **35**, 32-46.
150. J. Folkman and M. Klagsbrun, *Science*, 1987, **235**, 442-447.
151. D. I. Pattison and M. J. Davies, *Actions of ultraviolet light on cellular structures* Springer
152. Claridge, T. D. W. Practical Aspects of High-Resolution NMR. In *High-Resolution NMR Techniques in Organic Chemistry (Third Edition)*, Claridge, T. D. W., Ed.; Elsevier: Boston, 2016; Chapter 3, pp 61-132.
153. In *The Merck Index: An Encyclopedia of Chemicals, Drugs, and Biologicals*, 14th ed.; O'Neil, M. J.; Heckelman, P. E.; Koch, C. B.; Roman, K. J., Eds.; Merck Co., Inc.: Whitehouse Station, NJ, 2006.
154. J. Manura and D. Manura, *Scientific Instrument Services*, 2009, 1996-2009.